Construction and characterization of a para-hydrogen crystal Raman shifter for the mid-infrared range

im Fachbereich Physik
der Freien Universität Berlin

eingereichte

Diplomarbeit

vorgelegt von
Patrick Blitstein

Erstprüfer: Prof. Dr. Gerard Meijer

Berlin, April 2006

„If you understand hydrogen, you understand all that can be understood."

V. Weisskopf [1]

[1] G. Herzberg citing V. Weisskopf, in Herzberg, G. „The Spectra of Hydrogen and Their Role in the Development of Our Understanding of the Structure of Matter and of the Universe." Trans. Roy. Soc. Can. Vol. V Ser. IV (1967), 3

Kurzfassung

Gegenstand dieser Diplomarbeit ist der Aufbau und die Charakterisierung eines *para*-Wasserstoffkristall-Ramanshifters als Frequenzkonverter zum Betrieb als gepulste, kontinuierlich durchstimmbare Laserlichtquelle für den mittleren Infrarotbereich ($\nu \approx$ 1000 – 3300 cm^{-1}, entsprechend $\lambda \approx 3 – 10$ μm). Dieser Wellenzahlbereich ist von besonderem Interesse, da dieser Bereich wichtige charakteristische Molekülschwingungen sowohl organischer Moleküle, beispielsweise C-H Deformationsschwingungen, C-C Skelettschwingungen und Carbonyl– und Cyanogruppen, als auch eine Vielzahl von Banden umfasst, die für die Strukturaufklärung von Clustern sowie Clusterkomplexen, z. B. Übergangsmetalloxidcluster, Metallclustercarbonylkomplexe, usw. von Bedeutung sind.

Obwohl es zwar eine Vielzahl von Lichtquellen im mittleren Infrarotbereich (m-IR) gibt, herrscht ein Mangel an kompakten sowie gleichzeitig ausreichend leistungsstarken und genügend durchstimmbaren Laserquellen. Dies liegt im Wesentlichen in Folgendem begründet:

- Kommerzielle durchstimmbare m-IR-Laserquellen, die beispielsweise optische parametrische Verstärker (OPA) und/oder Differenzfrequenzmischer (DFM) verwenden, sind durch eine langwellige Grenze von etwa 4-5 μm eingeschränkt. Die nichtlinearen Kristalle, welche für die Frequenzkonversion bei Wellenlängen $\lambda \geq 5$ μm verwendet werden, haben recht niedrige Zerstörschwellen (typischerweise unter 10^{12} W/m^2)[2], so dass diese lediglich in nanosekundengepulsten Systemen mit niedrigen Leistungsdichten eingesetzt werden können. Hier ist der *para*-Wasserstoffkristall-Ramanshifter klar im Vorteil, denn die Zerstörschwelle des *p*-H_2-Kristalls ist nicht nur höher als in den oben genannten nichtlinearen Kristallen (> 10^{16} W/m^2), sondern im Falle einer Zerstörung des Kristalls durch zu hohe Leistungsdichten des Pumplasers, kann dieser ohne großen experimentellen Aufwand und fast ohne weitere Kosten in wenigen Stunden erneut gezüchtet werden.

[2] Zum Beispiel für $AgGaSe_2$ Kristalle, die in m-IR Systemen eingesetzt werden, vgl. z. B. http://www.toplent.com/aggase2.htm.

- Diodenlaser in diesem Wellenlängenbereich sind zwar erhältlich, haben aber typischerweise recht geringe gepulste Leistungen und für viele spektroskopische Anwendungen auch nicht den erforderlichen Durchstimmbereich.

- Freie Elektronenlaser (FEL), wie z. B. FELIX am FOM Rijnhuizen, sind in einem sehr großen Wellenlängenbereich durchstimmbar (etwa λ = 4 - 250 μm), welcher weit mehr als nur den m-IR-Bereich umfasst, und bieten auch Spitzenleistungen von 100 MW in (Sub-)Picosekundenpulsen, sind jedoch nicht gerade kompakte Strahlungsquellen, und außerdem durch recht große spektrale Breiten charakterisiert (ca. 0.4 – 7%).

Aufgrund der oben geschilderten Sachverhalte erscheint es gerechtfertigt, einen neuen experimentellen Zugang zu dem m-IR-Bereich zu suchen, welcher die oben genannten Nachteile überwindet.
Kürzlich wurde über den ersten erfolgreichen Aufbau eines *para*-Wasserstoffkristall-Ramanshifters als Quelle für die m-IR-Spektroskopie in der Arbeitsgruppe von Prof. Andrey F. Vilesov an der University of Southern California, Los Angeles, berichtet [Kuyanov, Momose et al. 2004, p. 26]. Dieser Ramanshifter stellt einen völlig neuartigen Frequenzkonverter dar, insofern als er sich deutlich von den seit ca. 35 Jahren verwendeten Ramanshiftern, die vor allem Wasserstoff-Gaszellen (bei hohen Drücken von ca. 30 bar) bzw. flüssigen Wasserstoff als Raman-aktives Medium verwenden, unterscheidet. Eine Untersuchung der Abhängigkeit des Verstärkungsfaktors α für die simulierte Ramanstreuung (SRS) von verschiedenen experimentell zugänglichen Parametern zeigt darüber hinaus, dass der Verstärkungsfaktor α für festen *para*-Wasserstoff um ungefähr **vier** Größenordnungen größer ist als für die klassischen Wasserstoff-Hochdruckzellen-Ramanshifter, bei welchen die Dopplerverbreiterung des beteiligten Schwingungsramanübergangs die Effizienz limitiert. Zusammen mit der großen Ramanverschiebung des festen *para*-Wasserstoffs (*p*-H_2) von 4149,75 cm^{-1} [3] begründet dies die Auswahl des Ramanmediums.
Während die klassischen Ramanshifter mindestens die *3. Ordnung* der Stokeswellen verwenden müssen, um in den m-IR-Bereich zu gelangen, wenn man diese etwa mit durchstimmbaren Farbstofflasern hoher Leistungsdichten pumpt (ca. 680 nm – 730 nm), verwendet der in dieser Arbeit beschriebene *para*-Wasserstoffkristall-Ramanshifter die *1. Sokeswelle*; hierzu wird er durch ein DFM/OPA System gepumpt, welches zur Abdeckung des gewünschten m-IR-Bereichs von ca. 1,5 – 2 μm durchge-

[3] Für den $Q_1(0)$ Schwingungsübergang bei 4,2 K, vgl. [Momose, Weliky et al. 1992]

stimmt wird. Dies bietet gegenüber den klassischen Ramanshiftern den Vorteil, dass die Quanteneffizienz der Frequenzkonversion im *para*-Wasserstoffkristall-Ramanshifter um ein Vielfaches größer ist, zumal auch die Effizienz mit der Ordnung der verwendeten Stokeswelle sinkt.

Abstract

The purpose of this diploma thesis is the development and characterization of a para-hydrogen crystal Raman shifter for the mid-infrared (m-IR) range as a frequency converter serving as a pulsed continually-tunable laser source for that spectral range ($\nu \approx$ 1000 – 3300 cm^{-1}, corresponding to $\lambda \approx$ 3 – 10 μm). This spectroscopic region is of particular interest, since it comprises characteristic molecular vibrations of organic molecules, e.g., C-H deformation modes, carbonyl groups and C-C skeletal modes, as well as many bands of relevance for structure determination of clusters and cluster complexes, such as transition metal oxide clusters, metal cluster carbonyl complexes etc.

Unfortunately, there is a lack of compact widely tunable m-IR laser sources due to essentially the following reasons:

- Tunable m-IR laser sources using for example optical parametric amplifiers (OPA) and/or difference frequency mixing (DFM) are limited to wavelengths below approximately 4-5 μm. Nonlinear crystals that are used for frequency conversion at wavelengths ≥ 5 μm have low damage thresholds (typically less than 10^{12} W/m^2)[4], so that they can only be used with nanosecond pulses of low power. The major advantage of using *p*-H_2 crystals is not only their high damage threshold (> 10^{16} W/m^2), but if the crystal is destroyed by too high laser powers, the crystal can be re-grown in only a few hours at virtually no additional expense.

- Diode lasers are available in the m-IR regime, but they have rather low pulsed output powers and too limited tuning ranges for many spectroscopic applications.

[4] Cf. for example http://www.toplent.com/aggase2.htm for $AgGaSe_2$ crystals used in commercial m-IR laser systems.

- Free electron lasers, like e. g. FELIX at the FOM Rijnhuizen, are tunable in a very large wavelengths region (approximately λ = 3 - 250 μm) and have high power outputs of 100 MW in (sub-)picosecond pulses, but are said to come with their own zip code, and they also have a relatively large spectral width (ca. 0.4 – 7%).

For the reasons stated above it seems justified to seek a new experimental approach into the m-IR region that overcomes the disadvantages of the techniques mentioned above. Recently, the successful construction and operation of a *para*-hydrogen crystal Raman shifter was reported in the group of Prof. Andrey F. Vilesov at the university of Southern California, Los Angeles [Kuyanov, Momose et al. 2004]. The Raman shifter described in their publication represents a new type of frequency converter, which differs fundamentally from the conventional Raman shifters that have been employed for over 35 years or so and mostly use high pressure hydrogen gas Raman cells (with pressure of approx. 30 bar) or liquid hydrogen cells as a Raman-active medium. Moreover, an examination of the dependence of the gain coefficient α for stimulated Raman scattering (SRS) on various experimentally accessible parameters reveals that the gain factor α is approximately **four** orders of magnitude larger than for the traditional gas-based hydrogen Raman shifters, which are limited in efficiency by the Doppler broadening of the involved vibrational Raman transition. Together with the large Raman shift of molecular hydrogen of 4149.75 cm^{-1} for solid *p*-H_2 at 4.2 K [5] this fact makes solid *para*-hydrogen an excellent choice as a Raman medium.

While in the classical Raman shifters at least the *3rd order* of the Stokes waves has to be employed in order to get into the desired spectral region if e. g. high power dye lasers (tune between approx. 680 – 730 nm) are used as a pump laser, the *para*-hydrogen Raman shifter described in the present work relies on the use of the 1st Stokes wave, and is pumped by a DFM/OPA system that has to be tuned from approx. 1,5 – 2 μm to cover the desired m-IR region. This new approach offers an advantage as compared to the classical Raman shifters, as the quantum yield decreases with the order of the Stoke wave order.

Keywords: Raman shifter, solid *para*-hydrogen, stimulated Raman scattering (SRS)

[5] For the $Q_1(0)$ vibrational transition, cf. [Momose, Weliky et al. 1992]

Table of contents

List of figures

List of tables

Abbreviations and glossary of symbols

SRS	stimulated Raman scattering
EQQ interaction	electrical quadrupole-quadrupole interaction
sccm	standard cubic centimeters per minute

Introduction and motivation

Although stimulated Raman scattering (SRS) in molecular hydrogen is prevalently used to generate ***near***-infrared radiation[6], and solid hydrogen has been thoroughly investigated for over 70 years[7], only recently it has been found that the $Q_1(0)$ Raman transition at 4149.7 cm^{-1} in a cryogenic crystal of *para*-hydrogen (*p*-H_2) at T = 4 K has a very narrow linewidth, of less than 7 MHz[8] (corresponding to 0.0002 cm^{-1}) half width at half maximum (HWHM). This feature makes a Raman shifter based on solid p-H_2 far superior to the traditional ones which mostly use pressurized gaseous H_2 (linewidth of 0.003 cm^{-1} at 20 atm).[9]

Overview: Classical Raman shifters

After its discovery by Woodbury and Ng[10] in 1961, stimulated Raman scattering (SRS) quickly became a well-established technique for shifting laser radiation into various spectral regions, cf. e.g. the review article by Maier [Maier 1976]. Many studies of this third-order non-linear process have been conducted employing various pump lasers and experimental designs:

- Minck and Terhune used a giant pulsed ruby laser focused into gas cells containing H_2, D_2, and CH_4 at pressures up to 50 atm [Minck, Terhune et al. 1963].

- Dielectric waveguides can be used to improve the frequency conversion in the gases by enlarging the pump interaction region[11]: Hartig and Schmidt reported the production of tunable IR radiation (in the first, second and third Stokes orders) yielding light in the region from 0.7 to 7 μm with conversion efficiencies exceeding 1% for the 3rd Stokes order using a tunable high power dye laser as a pump source in a hydrogen gas filled waveguide [Hartig and Schmidt 1979].

---

[6] Minck and Terhune reported the first investigation – to the best of my knowledge – of SRS in different gases, including H_2 [Minck, Terhune et al. 1963].

[7] The first spectroscopic study of condensed molecular hydrogen was performed on the liquid phase by McLennan and McLeod in 1929, who have demonstrated the quasi-free rotation of hydrogen molecules by means of rotational transitions in the Raman spectra [McLennan and McLeod 1929].

[8] Cf. [Momose, Weliky et al. 1992] and [Weliky, Byers et al. 1994].

[9] Cf. [Sussmann, Weber et al. 1992]

[10] [Woodbury and Ng 1962].

- The pursuit of increasing the conversion efficiency into the higher Stokes orders has led to numerous other experimental setups, among the most successful ones being *multiple-pass cells (MPCs)*[12] which are rather bulky devices (using e.g. a Herriott cell[13] that can be up to 4 meters long in a more recent setup at the Saykally group in Berkeley used for *cavity ringdown laser absorption spectroscopy (CRDLAS)* of small water clusters and laser ablated carbon clusters[14]). A high Raman gain in these MPCs is achieved by a combination of a long optical path with periodic refocusing of the laser beam. But MPCs have another disadvantage, apart from requiring a high degree of expertise for their operation: Special mirrors that have high damage thresholds in a wide spectral range are also needed for the operation of MPC Raman shifters, leading to a substantial increase in costs.

The reported conversion efficiencies in these different experimental setups span a wide range. This is not only due to the dependence of the Raman gain on the pump wavelength, but is also due to the particularities of the individual experiments.

Figure 0-1 shows an example of a successful classical setup, which consists of a waveguide Raman cell employing a tunable dye laser oscillator parametric amplifier (OPA) as a pump source. The dye laser output was focused into a H_2 waveguide cell made of glass with a 0.6 mm bore diameter and a length of 0.75 m. The frequency range of this Raman shifter was 0.7 – 7 μm by using the first three Stokes waves.

[11] The first brief report of a waveguide hydrogen Raman shifter is found in [Rabinowitz, Kador et al. 1976]

[12] Cf. [Rabinowitz, Perry et al. 1986] and [Trutna and Byer 1980]

[13] Cf. [Herriott, Kogelnik et al. 1964] and [Herriott and Schulte 1965]

[14] [Paul, Provencal et al. 1998] and [Casaes, Provencal et al. 2002]

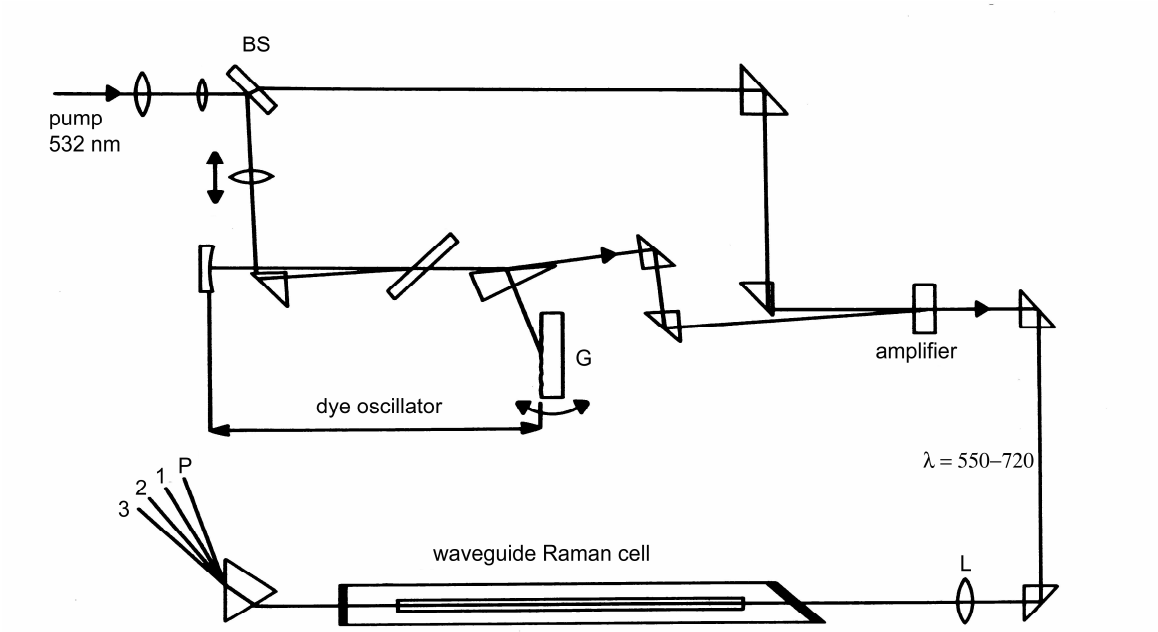

Figure 0-1: *Waveguide Raman shifter by Hartig and Schmidt [Hartig and Schmidt 1979].*

Solid para-hydrogen Raman shifters

The outstanding properties of solid *para*-hydrogen as a Raman medium have been the subject of many experimental studies and publications. A major breakthrough regarding the construction of a *para*-hydrogen crystal based Raman shifter was achieved by Hakuta, Suzuki, Katsuragawa and Li [Hakuta, Suzuki et al. 1997]. In their paper they showed that the familiar *phase-matching conditions* are not generally valid, i.e., in solid *p*-H_2 crystals the ***phase-matching can be self-induced***. Before that, it was generally assumed that the phase velocity had been restricted by the refractive index of the Raman medium, and thus the phase-matching condition was assumed to be strictly dominated by the dispersion of the Raman medium. The self-induced phase-matching is explained as resulting from the ***strong coupling*** between the radiation fields and the optical phonon fields induced by the stimulated Raman scattering (SRS) process.

In paragraph 1.3 it will be shown that the Raman width Γ_R is a key parameter not only for fulfilling the strong coupling condition [Hakuta, Suzuki et al. 1997], but it also governs the SRS gain coefficient α, which is computed in that paragraph.

$$\alpha \propto \frac{nP_P}{\lambda_S\left(\lambda_S+\lambda_P\right)\Gamma_R}$$

That is, the gain coefficient α is proportional to the number density n of the Raman-active medium and the pump power P_P, and inversely proportional to the line width of the Raman transition Γ_R.

In this context it is interesting to note the vast differences in the Raman width for the different states of molecular hydrogen shown in **Table 1-2**. This also explains our choice of the Raman medium. A more detailed discussion is found at the end of paragraph 1.3.

1 Theory of Raman scattering

In the first paragraph of this chapter, the *spontaneous* Raman scattering is treated in the semi-classical description. The transition polarizability tensor $\vec{\alpha}$ is treated in this description, from which it is deduced that the *spontaneous* Raman scattering produces *incoherent* radiation, as opposed to the *stimulated* Raman scattering (SRS) treated in the second paragraph, which occurs for higher pump power and produces *coherent* radiation. The third paragraph is devoted to the derivation of the plane-wave Raman gain coefficient, as maximizing the gain coefficient is one of the major goals in the development of our Raman shifter.

1.1 Spontaneous Raman scattering

If monochromatic light is incident on a transparent target (e.g. transparent gases, liquids or perfectly transparent solids), in addition to the light transmitted without change in frequency (***Rayleigh scattering***), one can in general detect some scattered light of new frequency components as well. The most effective scattering occurs due to the electrons within the medium, but the nuclear motion can in addition affect the light scattered by the electrons leading to *Raman* and *Brillouin scattering*: The change in frequency corresponds to the frequencies of the nuclear motion (or electronic transitions of the molecular system the target is composed of). In the case of scattering by *optical phonons*, the scattering is termed ***Raman scattering***, whereas in the case of scattering by *acoustical phonons* it is called ***Brillouin scattering***.

This inelastic scattering of light by optical phonons was first observed in liquids by C. V. Raman in the year 1928, and is referred to as ***Raman scattering*** (or ***Raman effect***), cf.[Raman and Krishnan 1928]. It is worthwhile to note that the Raman effect was predicted by A. Smekal five years before Raman succeeded in his experimental proof [Smekal 1923].

The energy level diagram for the Raman scattering process is shown in **Figure 1-1**.

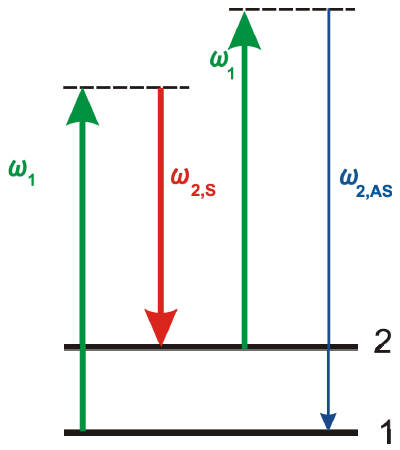

Figure 1-1: *Energy level diagram of the Raman process. The subscripts S and AS denote the Stokes and anti-Stokes waves, respectively.*

As can be seen in **Figure 1-1**, the spontaneous Raman effect is a direct two-photon inelastic light scattering, in which an incident pump photon of frequency ω_1 is absorbed, and a photon of frequency ω_2 is emitted while the Raman medium undergoes a transition from an initial state $|i\rangle$ to a final state $|f\rangle$ such that energy is conserved (up to an energy uncertainty caused by the finite linewidth), i.e.,

$$\hbar\omega_1 = \hbar\omega_2 + \underbrace{\left(E_f - E_i\right)}_{=:\hbar\omega_v}. \tag{1.1}$$

The energy difference $E_f - E_i$ corresponds to the energy of the phonon, $\hbar\omega_v$, created or annihilated in this process. In the first case, a molecular excitation is produced (***Stokes*** case) and the light is red-shifted, in the latter case the molecular system is de-excited and the light is blue-shifted (***anti-Stokes*** case) with respect to the incident light frequency. The dotted lines in **Figure 1-1** designate so-called *virtual levels* of the scattering molecule, meaning that these do not have to coincide with any quantum-mechanically allowed molecular states, i. e. these states are no solutions of the Schrödinger equation for the molecular system.

In the case which is of interest for our Raman shifter, the states 1 and 2 in **Figure 1-1** correspond to vibrational-rotational states designated by v = 0, J = 0 and v = 1, J = 0 in the ground electronic state $X^1\Sigma_g^+$ of molecular hydrogen, respectively. In solid hydrogen, the energy separation between these states is 4149.641±0.005 cm^{-1}, cf. [Katsuragawa and Hakuta 2000].

1.1.1 Semi-classical description

The earliest elaborate review of the Raman effect goes back to Placzek, who treats the Raman scattering according to classical ***polarizability theory*** [Placzek 1934]. This approach is not only very intuitive, but can also serve as a good basis for the description of the stimulated Raman scattering (SRS), which is treated in the next paragraph, as well as is the basis for the computation of the SRS gain coefficient.

Throughout this chapter, and especially in the treatment of SRS, the ***semi-classical treatment*** is adopted, i. e., the *quantization of the electromagnetic fields* is ***not*** carried out but disregarded as the number of phonons in the Raman mode is assumed to be large.

I will follow the description of C.-S. Wang [Wang 1969] and address only the points that are needed for the description of SRS in this paragraph.

The interaction between a molecule and an external electromagnetic field in the dipole approximation is given by the following Hamiltonian

$$H = H_0 - \boldsymbol{\mu} \cdot \mathbf{E}_L \tag{1.2}$$

in which H_0 is the unperturbed Hamiltonian of the molecule and

$$\boldsymbol{\mu} := \alpha \mathbf{E}_L \tag{1.3}$$

is the induced electric dipole moment of the molecule due to the action of the electric field $\mathbf{E}_L$.

Assuming that the term due to the field interaction, $\boldsymbol{\mu} \cdot \mathbf{E}_L$, is much smaller than H_0, the problem can be treated according to time-dependent perturbation theory. The eigenstates of the unperturbed Hamiltonian, H_0, are used in order to compute the wave functions of the molecular system up to the first order in the perturbation. This approach leads to the following expression for the ***transition polarizability*** for the Raman scattering, in which the molecular system undergoes a transition from the initial state $|i\rangle$ to the final state $|f\rangle$:

$$\alpha^{if}(\omega) = \frac{1}{\hbar} \sum_{r \neq i,f} \left\{ \frac{\langle i|e\mathbf{r}|r\rangle\langle r|e\mathbf{r}|f\rangle}{\omega_{rf} + \omega} + \frac{\langle i|e\mathbf{r}|r\rangle\langle r|e\mathbf{r}|f\rangle}{\omega_{ri} - \omega} \right\} \tag{1.4}$$

The summation is carried out over all intermediate states $|r\rangle$ of the molecule; also, for the sake of simplicity, the polarizability α is treated as a scalar, and not as a tensor. If we chose to treat the transition polarizability as a tensor, the $\alpha\beta$-component of the ***transition polarizability tensor*** is given as

$$\alpha_{\alpha\beta}{}^{if}(\omega) = \frac{1}{\hbar} \sum_{r \neq i,f} \left\{ \frac{\langle i|\mu_\alpha|r\rangle\langle r|\mu_\beta|f\rangle}{\omega_{rf} + \omega} + \frac{\langle i|\mu_\beta|r\rangle\langle r|\mu_\alpha|f\rangle}{\omega_{ri} - \omega} \right\} \tag{1.5}$$

In equations (1.4) or (1.5) we already find the answer to the question, why the spontaneously Raman-scattered radiation is *not* coherent: For computing the transition polarizability we have to form matrix elements which contain wave functions of arbitrary phases, as a consequence of which the transition polarizability itself depends on these phases. This means, that in general two scattering events occurring at two different molecular sites can not add up coherently.

The computation of the transition polarizability can be further simplified, if we assume that the transitions are *purely vibrational* (which is the case in the $Q_1(0)$ transition in molecular hydrogen), so that the translation and rotation of the molecule can be disregarded. To be more precise: We can use the Born-Oppenheimer approximation and the normal-mode expansion, according to Placzek [Placzek 1934; Wang 1969] in order to separate nuclear and electronic motion. This is, because of their mass ratio $m_P / m_e \approx 1837$ (for H_2), the nuclear motion is much slower than the electronic motion (and also the translation and rotation are much slower than the vibration).
In order to use the Born-Oppenheimer approximation we first expand the notation for a general total state $|j\rangle$ including electronic and nuclear states

$$|j\rangle = |e^j v^j R^j\rangle \tag{1.6}$$

such that its electronic, vibrational and rotational components are represented by their respective quantum numbers e^j, v^j and R^j. The corresponding notation for the circular frequency as a measure of energy (energy is expressed in units of rad s^{-1}; $\omega = E/\hbar$) is

$$\omega_j = \omega_{e^j v^j R^j} . \tag{1.7}$$

By virtue of the Born-Oppenheimer approximation we can now chose for the total state $|j\rangle$:

$$|j\rangle = |e^j\rangle \otimes |v^j\rangle \otimes |R^j\rangle \tag{1.8}$$

and for its energy,

$$\omega_j = \omega_{e^j v^j R^j} = \omega_{e^j} + \omega_{v^j} + \omega_{R^j} . \tag{1.9}$$

This separation approach implies the following relation for the *eigenfunctions of the unperturbed Hamiltonian* H_0:

$$\Psi_{nv}(x, X) = \underbrace{\chi_{nv}(X)}_{nucl.} \underbrace{\varphi_n(x, X)}_{electron.} \tag{1.10}$$

where $\varphi_n(x, X)$ denotes the electronic wave functions assuming that the electrons are moving in the field produced by the ***fixed*** (or "***clamped***") ***nuclei***, and n is the corresponding quantum number. The coordinates X refer to the nuclei.
If we denote the eigenvalues of the electronic eigenfunctions $\varphi_n(x, X)$ by $E_n(X)$, then the nuclear wave functions represent the nuclear motion in an effective electronic potential $E_n(X) - E_n(X^0)$, v being the vibrational quantum number. In the state $\Psi_{nv}(x, X)$, the eigenvalues of H_0 are determined predominantly by the electronic potential, since these are given as

$$E_n(X^0) + \varepsilon_{nv} , \tag{1.11}$$

with $\varepsilon_{nv} \ll E_{n'}(X) - E_n(X)$. Finally, it can be shown that this procedure leads to the following *simplified* expression for the ***transition polarizability***:

$$\alpha_{vv'}(\omega, X) := \langle v | \alpha(\omega, X) | v' \rangle , \tag{1.12}$$

where

$$\alpha\ (\omega, X) := \frac{1}{\hbar} \sum_{n \neq 0} \left\{ \frac{\langle 0|e\mathbf{r}|n\rangle\langle n|e\mathbf{r}|0\rangle}{\omega_{n0} + \omega} + \frac{\langle 0|e\mathbf{r}|n\rangle\langle n|e\mathbf{r}|0\rangle}{\omega_{n0} - \omega} \right\}, \tag{1.13}$$

and the $\alpha\beta$ ***-component of the transition polarizability tensor***

$$\alpha_{\alpha\beta}(\omega, X) := \frac{1}{\hbar} \sum_{n \neq 0} \left\{ \frac{\langle 0|\mu_\alpha|n\rangle\langle n|\mu_\beta|0\rangle}{\omega_{n0} + \omega} + \frac{\langle 0|\mu_\beta|n\rangle\langle n|\mu_\alpha|0\rangle}{\omega_{n0} - \omega} \right\}. \tag{1.14}$$

Here, $0 \equiv e^0$ is the electronic ground state. With the help of equations (1.13) or (1.14), respectively, we can now obtain a substantial simplification of the expression for the transition polarizabilities by expanding $\alpha(\omega, X)$ in a *Taylor's series* about the equilibrium position of the normal coordinate of the nuclear vibration [Placzek 1934]

$$\alpha\ (\omega, X) = \underbrace{\alpha\ (\omega, X^0)}_{\alpha_0(\omega, X)} + \sum_i \left(\frac{\partial \alpha\ (\omega, X)}{\partial q_i} \right)_0 q_i + \tfrac{1}{2} \sum_{i,j} \left(\frac{\partial^2 \alpha\ (\omega, X)}{\partial q_i \partial q_j} \right) + O\left(\frac{\partial^3 \alpha}{\partial q_i \partial q_j \partial q_k} \right), \tag{1.15}$$

with the normal-mode nuclear vibrational coordinate $q := X / \sqrt{\mu}$. The first term of equation (1.15) accounts for the index of refraction of the Raman medium, whereas the second term describes the coupling of the first-order Stokes (or anti-Stokes) waves to the optical phonon waves in the Raman medium (molecular vibrations). The higher-order terms in (1.15) denoted by the Landau symbol O allow for the multi-phonon processes in the medium. Now we may write the first-order term of the ***transition polarizability*** as

$$\begin{aligned} \langle v|\alpha\ (\omega, X)|v'\rangle &= \langle v| \sum_i \left(\frac{\partial \alpha\ (\omega, X)}{\partial q_i} \right)_0 q_i |v'\rangle \\ &= \sum_i \langle v| \left(\frac{\partial \alpha\ (\omega, X)}{\partial q_i} \right)_0 q_i |v'\rangle \\ &= \sum_i \left(\frac{\partial \alpha\ (\omega, X)}{\partial q_i} \right)_0 \langle v|q_i|v'\rangle \end{aligned} \tag{1.16}$$

This constitutes a major simplification, since we now only have to deal with ***one*** dynamic molecular variable, the normal-mode coordinate q of the nuclear vibration. The *coupling constant* for the interaction of the electromagnetic field induced by the laser and the optical phonons (of angular frequency ω_v) in the Raman-active medium is given as the derivative of the electronic polarizability with respect to the normal-mode coordinate q

$$\sum_i \left(\frac{\partial \alpha\ (\omega, X)}{\partial q_i} \right)_0 =: \left(\frac{\partial \alpha}{\partial q} \right)_0 . \tag{1.17}$$

1.1.2 Classical Raman scattering cross-section

The general form for the relation between the intensity I of Raman (or Rayleigh) scattered radiation from a single molecule and the ***irradiance*** P (by definition, this is the radiant power incident per unit area upon a surface with units of $[P]$ = Wm^{-2}, sometimes also called *power density*) of the incident (laser) radiation is given as

$$I = \sigma' P . \tag{1.18}$$

For the comparison of scattering efficiencies of different molecules it is useful to define the scattering cross section which is primarily a molecular property that is independent of the irradiance of the incident radiation (but in general not of other experimental factors). By definition, σ' is the (*first*) ***differential cross-section*** (per molecule), $[\sigma']$=m^2 sr^{-1} $molecule^{-1}$. The ***total cross-section*** (per molecule) σ is defined by

$$\sigma = \int_0^{4\pi} \sigma' d\Omega . \tag{1.19}$$

The (second) differential cross-section

$$\sigma'' = \frac{\partial \sigma'}{\partial \bar{\nu}} = \frac{\partial^2 \sigma}{\partial \bar{\nu} \partial \Omega} \tag{1.20}$$

takes into account that the scattered intensity varies across a range of wavenumbers around a central wavenumber. σ'' has the unit $[\sigma'']$ = m sr^{-1} $molecule^{-1}$.

The aabove equations can be interpreted in the following manner: σ measures the *rate at which energy is removed from the incident beam* by scattering over 4π steradians, *relative to the rate at which energy crosses a unit area perpendicular to the direction of propagation of the incident beam*. This is, the radiation scattered over 4π steradians by a molecule with the scattering cross-section σ corresponds to the radiation incident on the area σ.

For the rest of this paragraph the following assumptions are made (unless explicitly stated otherwise): The majority of the molecular population is in the ground state. This assumption is justified because the energy of the molecular vibration is often less than kT: $\left|E_{vib.}\right| \ll kT$. For solid hydrogen below 10 K, this assumption is fulfilled since the characteristic vibrational and rotational temperatures are approximately 6000 K and 180 K. The population of higher levels is reduced by the respective Boltzmann factors, so that in general higher-order Stokes and anti-Stokes emission is reduced. For this-reason the following treatment only includes the *first* Stokes component.

It is straightforward to compute the *first differential cross-section* (or power irradiated per unit solid angle) if we use the model of an oscillating electric dipole (***Hertzian dipole***) with an oscillation frequency equal to that of the first Stokes wave. In the case of a linearly polarized incident electromagnetic wave the ***power per unit solid angle*** is given as

$$\frac{dP}{d\Omega} = \frac{\hbar\omega_s^4}{4\pi c^3 \omega_\nu}\left(\frac{\partial\alpha}{\partial q}\right)_0^2 \left|E_L\right|^2 \mathbf{cos}^2\,\theta \tag{1.21}$$

where

$$\theta := \sphericalangle(\mathbf{k}_L, \mathbf{k}_s)\,, \tag{1.22}$$

and ω_ν is the ***optical phonon angular frequency*** (or vibrational frequency of the molecules in the Raman-active medium). This yields the following (first) differential and total cross sections for the spontaneous Raman scattering (per molecule):

$$\frac{d\sigma}{d\Omega} = \frac{dP}{d\Omega}\left(\frac{4\pi}{c\left|E_L\right|^2}\right) = \frac{\hbar\omega_s^4}{c^4\omega_\nu}\left(\frac{\partial\alpha}{\partial q}\right)_0^2 \left|E_L\right|^2 \mathbf{cos}^2\,\theta \tag{1.23}$$

$$\sigma = \frac{8\pi\hbar\omega_s^4}{3c^4\omega_\nu}\left(\frac{\partial\alpha}{\partial q}\right)_0^2 \tag{1.24}$$

For many molecules, the order of magnitude is $\sigma \approx 10^{-30} cm^2$ for the total spontaneous Raman cross section. Table 1-1 lists Raman lines of some materials in which spontaneous and stimulated Raman scattering were both measured, according to Shen [Shen 1975]: the frequency shift, linewidth, scattering cross-section of spontaneous Raman scattering and SRS gain factor for some molecular systems and crystals are tabulated.

To summarize, the following ***approximations*** were made in order to quantitatively describe the spontaneous Raman effect [Placzek 1934; Wang 1969; Wang 1975]:

We used the *dipole approximation*, making use of the ratio of the molecular dimensions versus the optical wavelengths as an expansion parameter,
next, the *Born-Oppenheimer approximation* was utilized relying on the ratio of the electronic and nuclear mass as the parameter,
the *normal-mode expansion* was applied using the change of the nuclear separation versus the separation as the parameter,
the population of the molecules in the vibrational ground state is assumed to be much larger than in the exited states due to the *Boltzmann statistics* ($e^{-\hbar\omega_v / kT} \ll 1$), and finally the interaction of molecules with the electromagnetic field was treated according to *perturbation theory*.

It is obvious that the above approximations do not hold if the incident laser field intensities reach the order of the interatomic fields, which are of the order $E_{atom.} \cong 10^9 V / cm$, whereas the intensities for the laser used in the present work are of the order $E_L \cong 5 \cdot 10^6 \ V / cm$, corresponding to an irradiance of $P_L \cong 5 \cdot 10^{11} W / cm^2$. This has an important implication for the treatment of the stimulated Raman scattering (SRS): Since the above approximations are obviously good, we may use the same parameters and dynamical variables for the treatment of the Stokes photons and optical phonons in the *stimulated Raman effect*.
From Table 1-1 one readily concludes that in order to generate $\approx 10^{13}$ Stokes photons from one "*noise photon"*, one would need to use a laser of 1 GW/cm^2 power in a 15 cm long nitrobenzene cell, cf. equation (1.25), as Shen pointed out [Shen 1975]. The Raman gain g_{ss} (1.25) is defined in equation in the next section.
But the case is definitely more complicated, since experiments proved that lasers of *less than* 100 MW/cm^2 suffice in order to get *more than* 10^{13} Raman (Stokes or anti-Stokes) photons [Stoicheff 1963].

This and other peculiarities of SRS were explained as being a consequence of ***self-focusing*** of the incident laser beam in the Raman-active medium. Among the other peculiarities that puzzled the experimentalists as well as the theorists were the asymmetry of forward and backward scattered Raman intensities, the existence of a very sharp SRS threshold power density, and the spectral broadening of Raman radiation [Shen 1975].

Table 1-1: Spontaneous Raman cross-sections and SRS gain coefficients for different substances.

substance	Raman shift [cm^{-1}]	linewidth 2Γ [cm^{-1}]	cross-section $\frac{d\sigma}{d\Omega}$ [10^{-8} $cm^{-1}ster^{-1}$]	Raman gain g_{ss} [10^{-3} cm/MW]
H_2 (gas) [a]	4155	0.2	--	**1.5** (300 K, 10 atm)
solid *p*-H_2	4149.75 [c]	0.0002 [c]	--	**(18±3) 10^3** [d]
O_2 (liquid)	1522	0.177	0.48±0.14	14.5±4
N_2 (liquid)	2326.5	0.067	0.29±0.09	17±5
benzene	992	2.15	3.06	2.8
CS_2	655.6	0.50	7.55	24
nitrobenzene	1345	6.6	6.4	2.1
$LiNbO_3$	258	7	262	28.7
InSb [b]	0-300	0.3	10	1.7 x 10^4

[a] [Hagenlocker, Minck et al. 1967],

[b] for a carrier concentration $n_e \simeq 10^{16}\ cm^{-3}$,

[c] [Momose, Weliky et al. 1992], [d] [Katsuragawa and Hakuta 2000].

1.2 Stimulated Raman scattering

The discovery of the stimulated Raman scattering (SRS) by Woodbury and Ng [Woodbury and Ng 1962] occurred accidentally, as Shen points out in [Shen 1975]: “In studying Q-switching of a ruby laser by a nitrobenzene Kerr cell, they [Woodbury and Ng] detected intense infrared radiation emitted from the Kerr cell, whose origin was not immediately identified.” Interestingly, this discovery was made in the same laboratory where the first ruby-laser was built two years before by Maiman [Maiman 1960]. The

effect was interpreted soon thereafter by Eckhardt and observed also in different other liquids and solids [Eckhardt, Hellwarth et al. 1962].

From the numerous theoretical descriptions of SRS [Hellwarth 1963; Buckingham 1965; Shen 1965; Shen and Bloembergen 1965; Bloembergen 1967; Helen 1967; Wang 1969; Shen 1975; Maier 1976], I have chosen the ***polarizability model*** (sometimes also referred to as the ***coupled-wave model***) since it is well suited for computing the Raman gain coefficient, which is addressed in the next paragraph. Therefore, I will only cover this approach to SRS, once again following Wang's description [Wang 1969].

1.2.1 The steady-state limit for SRS

For a high intensity of the incident radiation, the Raman scattered waves can experience an amplification in which an initially scattered Stokes photon can stimulate the emission of additional Stokes photons, such that the Stokes wave exponentially increases in intensity (in the *SRS onset region*, this case will be referred to as the "***small signal limit***"). This process is termed **stimulated Raman scattering** (**SRS**). For SRS, very high quantum yields of over 50% have been reported. As a comparison, in the spontaneous Raman scattering only approximately 1 in 10 million photons is scattered [Wang 1975].

The *intensity of the Stokes field* is given as a function of the distance z travelled in the Raman medium (in the small signal limit)

$$I_s(z) = I_s(0)\ e^{G_{ss}z} = I_s(0)\ e^{g_{ss}I_p(0)z}, \tag{1.25}$$

where G_{ss} denotes the ***steady-state Raman power gain coefficient*** per unit pump intensity, and I_s and I_p are the Stokes and pump intensities, respectively.

In the next section it will be shown that g_{ss} is proportional to the number density *N* of molecules in the Raman-active medium and to the Raman susceptibility $\chi_R^{(3)}$.

1.2.1.1 Polarizability model

In the ***polarizability model*** (or *coupled-wave mode*l) the optical electromagnetic fields are coupled to the material vibration (or optical phonons) by the ***nonlinear Raman polarizability***. This model is a semi-classical model in the sense that the pump and Stokes fields are *not* quantized; this treatment is appropriate for most Raman scattering experiments in which the numbers of photons (and phonons) in the Raman mode are large. If this is not the case, the so-called *second quantization* (of electromagnetic fields) is necessary; this full quantum description is beyond the framework of this diploma thesis and thus is not addressed.

The polarizability model of SRS employs two sets of differential equations, one set describing the time and space dependent electric fields (i.e., the pump and Stokes fields, $\mathbf{E}_P$ and $\mathbf{E}_S$) and another set describing the molecular system as a damped harmonic oscillator coherently driven by a vibrational wave. The coupling of these two sets of differential equations is given by the nonlinear Raman polarization. For the sake of simplicity, only the first Stokes wave generation will be addressed here.
Let $\mathbf{P}$ denote the induced Raman polarization, then the wave equation describing the propagation of the pump and Stokes fields in the Raman medium is given by

$$\vec{\nabla}^2\mathbf{E} - \frac{\varepsilon}{c^2}\frac{\partial^2}{\partial t^2}\mathbf{E} = \frac{4\pi}{c^2}\frac{\partial^2}{\partial t^2}\mathbf{P}. \tag{1.26}$$

Expressing the induced nonlinear polarization by means of equations (1.3), (1.16) and (1.17), we can write

$$\mathbf{P} = N\left(\frac{\partial\alpha}{\partial q}\right)_0 q\mathbf{E} \tag{1.27}$$

if N is the *number density* of molecules in the Raman medium. Using the above expression, with equation (1.26) we obtain the wave equation

$$\vec{\nabla}^2\mathbf{E} - \frac{\varepsilon}{c^2}\frac{\partial^2}{\partial t^2}\mathbf{E} = \frac{4\pi}{c^2}N\frac{\partial^2}{\partial t^2}\left\{\left(\frac{\partial\alpha}{\partial q}\right)_0 q\mathbf{E}\right\}. \tag{1.28}$$

The second equation is that for the Raman medium which is treated as a damped harmonic oscillator, cf. e.g. [William R. Trutna, Park et al. 1979]:

$$\left\{\frac{\partial^2}{\partial t^2}+2\Gamma\frac{\partial}{\partial t}+\omega_\nu^2\right\}q = NF(\mathbf{z},t)\,. \tag{1.29}$$

Here $F(\mathbf{z},t)$ is the driving force, ω_ν is the optical phonon frequency (i.e., the Raman vibration frequency) and Γ is the *damping constant of the coherent vibrational wave*. Γ can be interpreted as the collisional dephasing rate and is given as $1/2T_2$, where T_2 is the dephasing time in the *Bloch equations*, and is equal to the halfwidth at half-maximum (HWHM) for the Raman transition between the initial and final states, $|i\rangle$ and $|f\rangle$.

The potential energy of a molecule in the electric field induced by the incident laser can be expressed with the help of equation (1.15)

$$U = -\boldsymbol{\mu}\bullet\mathbf{E} \cong -\alpha_0\mathbf{E}\bullet\mathbf{E} - \left(\frac{\partial\alpha}{\partial q}\right)_0 q\mathbf{E}\bullet\mathbf{E} \tag{1.30}$$

The displacement force acting on the molecules is given by the negative gradient (with respect to the nuclear coordinate q) of the potential

$$F = -\vec{\nabla}_q U = \left(\frac{\partial\alpha}{\partial q}\right)_0 \mathbf{E}\bullet\mathbf{E}\,, \tag{1.31}$$

so that we can write equation (1.29) as

$$\left\{\frac{\partial^2}{\partial t^2}+2\Gamma\frac{\partial}{\partial t}+\omega_\nu^2\right\}q = N\left(\frac{\partial\alpha}{\partial q}\right)_0 \mathbf{E}\bullet\mathbf{E}\,. \tag{1.32}$$

At this point once again a few *assumptions* are necessary in order to further simplify the solution to the equations (1.28) and (1.32), which constitute the starting point for the polarizability model:

It is common to consider only waves propagating along the direction of the incident laser beam axis, which we shall denote by the z-direction. This assumption is well met

in the case of an isotropic and non-dispersive Raman medium, whereas in the cases of anisotropic or dispersive media phase-matching conditions can lead to off-axis scattering.

Assuming that the Raman media are *isotropic* and *non-dispersive*, we shall only address fields propagating in forward (+ z) and backward (- z) directions.
We shall consider the Stokes and pump fields to be single plane wave fields.

With the above approximations, we can write the following expressions for the electric fields and molecular vibrational coordinates:

$$E_P = \hat{E}_P(z,t)\ e^{ik_P z - i\omega_P t} \tag{1.33}$$

$$E_S = \hat{E}_s^{\,f}(z,t)\ e^{ik_S z - i\omega_S t} + \hat{E}_s^{\,b}(z,t)\ e^{-ik_S z - i\omega_S t} \tag{1.34}$$

$$q = \hat{q}^{\,f}(z,t)\ e^{ik_\nu^{\,f} z - i\omega_\nu t} + \hat{q}^{\,b}(z,t)\ e^{ik_\nu^{\,b} z - i\omega_\nu t}\,. \tag{1.35}$$

In these equations, $\hat{E}_P(z,t)$, $\hat{E}_s^{\,f/b}(z,t)$ and $\hat{q}^{\,f/b}(z,t)$ are the amplitudes of the slowly varying complex fields. The superscripts denote forward and backward waves, respectively. $\hat{E}_P(z,t)$ is treated as a parameter since in the small signal limit, the incident laser electrical field amplitude can be approximated to be a constant.[15]
In the following, the forward and backward directions of the Stokes scattered waves are treated separately, as different phase and frequency-matching conditions apply to these cases, and also the coupled differential equations for the electric laser fields and optical phonon waves are not the same.
By inserting equations (1.33) - (1.35) into the coupled equations (1.28) and (1.32), we obtain equations describing the growth of the Stokes electric field amplitudes.

For the forward scattered Stokes wave, we have the following *phase and frequency-matching conditions*:

$$k_\nu^{\,f} = k_P - k_S \;;\omega_\nu = \omega_P - \omega_S\,, \tag{1.36}$$

[15] Of course, this assumption can no longer be made if the intensities of the incident laser field are higher, such that the incident laser intensity becomes depleted to an extent that cannot be disregarded. Also, some conversion of the first Stokes wave into higher order Stokes and anti-Stokes waves can occur. This is treated e.g. in [Shen 1965; Shen and Bloembergen 1965; Shen 1975].

the coupled equations yielding

$$\begin{cases} \dfrac{1}{\nu_S}\dfrac{\partial \hat{E}_S^f}{\partial t} + \dfrac{\partial \hat{E}_S^f}{\partial z} = iK_2 \left\{q^f\right\}^* \hat{E}_P(z,t) \\ \dfrac{\partial \left\{q^f\right\}^*}{\partial t} + \Gamma \left\{q^f\right\}^* = -iK_1 \hat{E}_S^f \hat{E}_P^*(z,t) \end{cases} \tag{1.37}$$

Here ν_S is the group velocity of the Stokes wave and the constants K_1 and K_2 are given by

$$K_1 = \frac{N}{2\omega_\nu}\left(\frac{\partial \alpha}{\partial q}\right)_0, \tag{1.38}$$

$$K_2 = \frac{2\pi N \omega_S^2}{k_S c^2}\left(\frac{\partial \alpha}{\partial q}\right)_0. \tag{1.39}$$

Analogously, the following equations apply to the backward scattered Stokes wave:

$$k_\nu^b = k_P + k_S \;;\omega_\nu = \omega_P - \omega_S \tag{1.40}$$

$$\begin{cases} \dfrac{1}{\nu_S}\dfrac{\partial \hat{E}_S^b}{\partial t} + \dfrac{\partial \hat{E}_S^b}{\partial z} = iK_2 \left\{q^b\right\}^* \hat{E}_P(z,t) \\ \dfrac{\partial \left\{q^b\right\}^*}{\partial t} + \Gamma \left\{q^b\right\}^* = -iK_1 \hat{E}_S^b \hat{E}_P^*(z,t) \end{cases} \tag{1.41}$$

Making some additional assumptions, equations (1.37) and (1.41) can be solved. These assumptions are summed up as the ***steady-state regime***, i.e., if the relaxation times for Raman scattering are much smaller, the pump pulse temporal width[16] then the incident laser field amplitude can be treated as a time and space-independent parameter:

$$\hat{E}_P(z,t) \approx \hat{E}_P. \tag{1.42}$$

[16] In liquids and solids the Raman scattering relaxation times are in the order of 10^{-11} to 10^{-13} s and for gases in the order of 10^{-9} s [Bret and Denariez 1966; Lallemand, Simova et al. 1966; Clements and Stoicheff 1968; Kato and Takuma 1971; Laubereau, Linde et al. 1971; Linde, Laubereau et al. 1971; Laubereau, Linde et al. 1972; Laubereau, Greiter et al. 1974; Laubereau, Wochner et al. 1976], such that SRS with nanosecond laser pulses can be regarded as a quasi steady-state process, if other nonlinear optical phenomena like self-focusing can be neglected.

Under these assumptions, both equations (1.37) and (1.41) can be solved yielding an exponential growth for the forward and backward scattered Stokes waves according to

$$\hat{E}_S^{f/b} = \hat{E}_S(z=0)\; e^{G_{ss}z/2}, \tag{1.43}$$

where

$$G_{ss} = \frac{2K_1K_2\left|\hat{E}_P\right|^2}{\Gamma} = \frac{2\pi\omega_S^2N^2}{\omega_v k_S c^2\Gamma}\left(\frac{\partial\alpha}{\partial q}\right)_0^2\left|\hat{E}_P\right|^2 \tag{1.44}$$

is the so-called steady-state Raman gain coefficient.

According to W. R. Trutna, Jr. , Park and Byer [William R. Trutna, Park et al. 1979], the Stokes power gain coefficient in the steady-state regime can be related to the so-called *on-resonance Raman susceptibility*[17] $\chi_R^{(3)}$ in the following manner:

$$P_S = \chi_R^{(3)}\hat{E}_P\hat{E}^*_P\hat{E}_S \tag{1.45}$$

$$\chi_R^{(3)} = \frac{2n_Sc}{\omega_S}\frac{K_1K_2}{\Gamma} \tag{1.46}$$

$$G_{ss} = \frac{\omega_S}{n_Sc}\chi_R^{(3)}\left|\hat{E}_P\right|^2 \tag{1.47}$$

1.3 The plane-wave Raman gain coefficient

As we have seen in the previous paragraph, the polarizability model of Raman scattering – though a simple model – is adequate for describing the process of SRS in the sense that correct results are obtained (except for a population difference factor). Also, the magnitude of the Raman gain is not predicted correctly, but it is possible to append some quantum mechanical correction factors in order to obtain the correct results nonetheless.

In this paragraph, I shall give a brief overview of the dependence of the Raman gain on various experimentally accessible parameters. Since maximizing the Raman gain es-

[17] Cf. [Pantell and Puthoff 1969, p. 232ff.].

sentially constitutes our major experimental focus, I shall seek to give a somewhat more detailed derivation of the Raman gain dependence according to the description of Trutna and Byer [Trutna and Byer 1980].

The following wave equation describes the propagation of electric fields in a medium

$$\vec{\nabla}\times\left(\vec{\nabla}\times\mathbf{E}\right)+\mu\varepsilon\frac{\partial^2\mathbf{E}}{\partial t^2}=-\mu_0\frac{\partial^2}{\partial t^2}\mathbf{P} \tag{1.48}$$

where $\mathbf{P}$ is the induced polarization in the medium. For a Stokes field propagating in a Raman medium, the following wave equation applies:

$$-\vec{\nabla}^2\mathbf{E}_S+\mu\varepsilon\frac{\partial^2}{\partial t^2}\mathbf{E}_S=-\mu_0\frac{\partial^2}{\partial t^2}\mathbf{P}_S \tag{1.49}$$

$\mathbf{P}_S$ denotes the driving polarization at the Stokes frequency generated in the medium. The following approach for the steady-state solutions can be made

$$\mathbf{E}_S(\mathbf{r},t)=\tfrac{1}{2}\left\{\hat{\mathbf{E}}_S e^{ik_s z-i\omega_s t}+c.c.\right\} \tag{1.50}$$

$$\mathbf{E}_p(\mathbf{r},t)=\tfrac{1}{2}\left\{\hat{\mathbf{E}}_p e^{ik_p z-i\omega_p t}+c.c.\right\} \tag{1.51}$$

Using the slowly varying amplitude approximation[18], it can be shown that the equation describing the Raman gain and diffraction of the Stokes wave is

$$\left[\nabla_T^2+2ik_s\frac{\partial}{\partial z}\right]\mathbf{E}_S(\mathbf{r})=ik_s G_{ss}\mathbf{E}_S(\mathbf{r}) \tag{1.52}$$

where $\nabla_T^2=\frac{\partial^2}{\partial x^2}+\frac{\partial^2}{\partial y^2}$ is the *transverse component* of the *Laplacian* and the ***plane-wave Stokes power gain***, G_{ss}, which is proportional to the pump intensity I_p and inversely proportional to the Stokes wavelength

$$G_{ss} = \frac{\omega_s}{n_s c} \chi_R^{(3)} \left| \mathbf{E}_p^2 \right| = g_{ss} I_p \tag{1.53}$$

with

$$g_{ss} = 2 \frac{\omega_s \chi_R^{(3)}}{n_s n_p c^2 \varepsilon_0} \tag{1.54}$$

The plane-wave Stokes power gain coefficient given in equation (1.53) is equal to the steady-state Raman gain coefficient of equation (1.47). It can be shown that the following relation between the differential Raman cross section $d\sigma / d\Omega$ given by equation (1.23) and the on-resonance Raman susceptibility $\chi_R^{(3)}$ is valid

$$\chi_R^{(3)} = \frac{(2\pi)^3 n_P c^4 \varepsilon_0 N (d\sigma / d\Omega)}{\pi n_S \omega_P \omega_S^3 \hbar (2\Gamma_R)}. \tag{1.55}$$

In equation (1.55), N denotes the population density, n_S is the index of refraction at the Stokes wavelength λ_S and Γ_R is the HWHM Raman linewidth, yielding for the plane-wave Stokes power gain coefficient

$$G_{ss} = \frac{4\lambda_S^2 N}{n_S^2 \omega_P \hbar (2\Gamma_R)} \left(\frac{d\sigma}{d\Omega} \right) I_p . \tag{1.56}$$

We are interested in solutions to equation (1.52) for the case of *tightly focused Gaussian pump intensity profiles*, which are the experimentally most relevant beam intensity profiles for many pump lasers. This approach has been adressed in detail [Boyd, Johnston et al. 1969; Cotter, Hanna et al. 1975; Trutna and Byer 1980], and since it is beyond the scope of this diploma thesis to address all aspects such as e.g. *gain focussing* etc., I shall only summarize the results of these considerations.

The Gaussian pump profile approach has implications regarding the spot size w_{S0} of the Stokes beam that maximizes the Stokes gain for a given pump spot size w_{P0}. It can be shown that the ***maximum gain*** occurs in the case of so-called *equal confocal parameter ratio*:

---

[18] $\mathbf{E}_S$ is assumed to be slowly varying compared to a wavelength such that

$$\frac{w_{S0}}{w_{P0}} = \sqrt{\frac{\lambda_S}{\lambda_P}}\,. \tag{1.57}$$

It can be further concluded that with this choice of the Stokes spot size, the ***maximum Stokes power gain*** is e^{α}, with

$$\alpha \cong \frac{4P_P G}{\lambda_S + \lambda_P} \arctan\left(\frac{L}{b}\right), \tag{1.58}$$

where L is the cell length and b denotes the *confocal parameter* given by

$$b = \frac{2\pi w_{P0}^2}{\lambda_P}\,. \tag{1.59}$$

Now, because the plane-wave Stokes gain coefficient $G \propto n\lambda_S^{-1}\Gamma_R^{-1}$ is inversely proportional to the Stokes wavelength λ_S and to the Raman width (HWHM) and proportional to the number density of molecules in the Raman medium, we obain for the ***gain coefficient***

$$\boxed{\alpha \propto \frac{nP_P}{\lambda_S\left(\lambda_S + \lambda_P\right)\Gamma_R}} \tag{1.60}$$

The above equation (1.60) can be regarded as the central formula for the construction of our para-hydrogen crystal based Raman shifter since it describes the dependence of the ***maximum plane-wave Stokes power gain*** for tightly focused Gaussian pump beams upon the parameters that can be controlled by the choice of the Raman-active medium and the experimental design. In equation (1.60), *n* denotes the number density of Raman-active molecules, and P_P denotes the pump laser power.

Now we are also in the position to compare different Raman-active media regarding their suitability for SRS-based frequency shifting. Table 1-1 shows the Raman line

---

$\left|\partial^2 \mathbf{E}_S / \partial z^2\right| \ll \left|2ik_s \partial \mathbf{E}_S / \partial z\right|$.

width – among other parameters – for different substances, while **Table 1-2** offers a closer look at the Raman width of the different states of molecular hydrogen.

Table 1-2: *Half-width at half-maximum (HWHM) Raman linewidths for the different states of molecular di-hydrogen.*

state	**Raman width** Γ_R [MHz]	**number density** n [mol/cm^3]
gasesous *n*-H_2 (T=300 K, p= 30 bar)	90 [a]	$4.2 \cdot 10^{-5}$
solid *n*-H_2 (T=4 K)	$13 \cdot 10^3$ [b]	0.044 [e]
solid para-H_2 (T=4 K)	< 7 [c,d]	0.043 [e]

[a] [Sussmann, Weber et al. 1992], [b] [Soots, Allin et al. 1965],

[c,d] [Momose, Weliky et al. 1992; Katsuragawa and Hakuta 2000]

From this table and with the help of equation (1.60), we can readily conclude that the Raman gain factor for solid para-H_2 is **more than 10^4 times** (or **four orders of magnitude**) higher than for the classical Raman shifters utilizing pressurized di-hydrogen gas.

I would like to conclude by drawing some further important **conclusions** from equation (1.60) and its deduction:

- The plane-wave Stokes Raman gain coefficient is *increased* by *tight focusing*.
- The only way to maximize the Raman gain further is to increase the pump power.
- There is a fundamental difficulty for building SRS-based Raman shifters for the IR spectral region since the Raman gain strongly decreases with increasing pump and Stokes wavelengths.

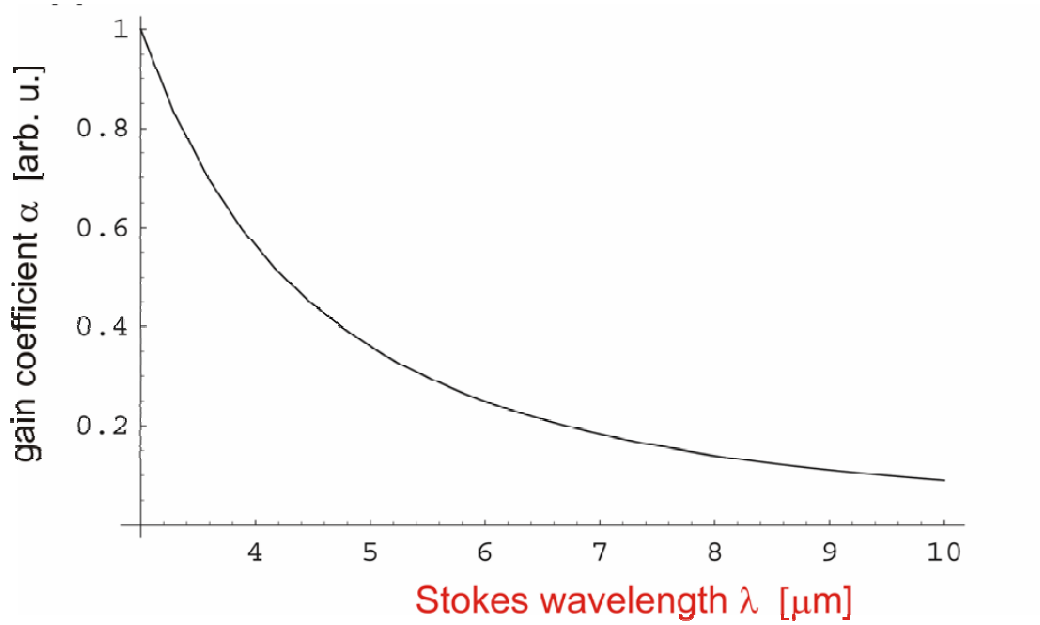

Figure 1-2: *Approximated dependence of gain coefficient α from output (Stokes) wavelength.*

2 Properties of hydrogen molecules

2.1 Isolated hydrogen molecules

Hydrogen is the simplest atom as compared to all elements. Under normal conditions, though, atomic hydrogen is not stable, and thus molecular di-hydrogen forms. The *homonuclear* molecular hydrogen isotopomers (H_2, D_2, and T_2) consist of two distinct species, *para*- and *ortho*-hydrogen (or -deuterium, or -tritium, respectively). These two species are a consequence of the requirements on the symmetry of the wave functions with respect to permutation of the involved nuclei. Species and states composed of an *antisymmetric* spin component are denoted as *para* species (or states), whereas those which are composed of *symmetric* spin components are denoted as ortho species (or states). For reasons discussed at the end of this chapter, these two species cannot convert into each other, except in the presence of a catalyst providing an external inhomogeneous magnetic moment, or, to put it in a more general way, ortho-para conversion can only be induced by magnetic dipole-dipole interaction, which includes interaction between the nuclear spins in neighboring molecules.
The Schrödinger equation for a system consisting of two nuclei and two electrons moving in a Coulomb potential describes the free molecules to a high degree of accuracy.

2.1.1 Born-Oppenheimer-approximation description of the hydrogen molecule

The Schrödinger equation for the simplest molecule, the hydrogen molecule H_2 (and its isotopomers HD, D_2, HT, DT and T_2) is that for a molecule with two nuclei and two electrons, dominated by their mutual Coulomb interaction,

$$\left(\sum_{i=1}^{4} \frac{1}{2m_i} \hat{\mathrm{p}}_i^2 + \sum_{i<j} \frac{q_i q_j}{\left| \mathrm{r}_i - \mathrm{r}_j \right|} \right) \Psi = E' \Psi \,, \tag{2.1}$$

in which the particles with subscripts 1 and 2 refer to the electrons, whereas the subscripts 3 and 4 refer to the nuclei. Thus m_1=m_2 is the electron mass m_e, and m_3 and m_4

are the masses of the nuclei (which need not be the same for the heteronuclear hydrogens). $\hat{\mathrm{p}}_i$ is the operator of linear momentum of particle *i*, q_i stands for the charge of particle i at position r_i , which is –*e* for the electrons and +*e* for the nuclei. Since the Schrödinger equation (2.1) contains the coordinates of *four* particles, it has 12 degrees of freedom. If we chose the center of gravity system description there are still 9 degrees of freedom remaining. We can make the following substitution in order to further simplify the equations: $\mathbf{r} := \mathbf{r_3} - \mathbf{r_4}$, thus introducing the nuclear distance **r** instead of the nuclear coordinates, such that the transformed Schrödinger equation reads in the form of the following eigenvalue equation:[19]

$$\left(\hat{H}_0 + \hat{H}_1 + \hat{H}_2\right)\Phi(\mathbf{r_e}, \mathbf{r}) = E\Phi(\mathbf{r_e}, \mathbf{r}) \tag{2.2}$$

where

$$\hat{H}_0 = \frac{-\hbar^2}{2m_e}\left(\vec{\nabla}_1^{\,2} + \vec{\nabla}_2^{\,2}\right) + \sum_{i<j}\frac{q_i q_j}{|\mathbf{r_i} - \mathbf{r_j}|}, \tag{2.3}$$

$$\hat{H}_1 = \frac{-\hbar^2}{2\mu}\vec{\nabla}_{\mathbf{r}}^{\,2}, \tag{2.4}$$

and

$$\hat{H}_2 = \frac{-\hbar^2}{8\mu}\left(\vec{\nabla}_1 + \vec{\nabla}_2\right)^2. \tag{2.5}$$

The nabla operators $\vec{\nabla}_1$ and $\vec{\nabla}_2$ contain derivatives with respect to the electronic coordinates $\mathbf{r}_i = (x_i, y_i, z_i), i = 1, 2$ in the center of mass system

$$\vec{\nabla}_i := \left(\frac{\partial}{\partial x_i}, \frac{\partial}{\partial y_i}, \frac{\partial}{\partial z_i}\right) \tag{2.6}$$

whereas the nabla operator $\vec{\nabla}_{\mathbf{r}}$ includes derivatives with respect to the coordinate of the internuclear distance $\mathbf{r} = (x, y, z)$

[19] Kolos and Wolniewicz published a series of papers [Kolos and Wolniewicz 1964b; Kolos and Wolniewicz 1964a], in which they put forward very comprehensive accurate first principles calculations on H_2 and its isotopomeres. These calculations serve as the basis of the formulation of solutions to the Schrödinger equation, which are described in this paragraph.

$$\vec{\nabla}_{\mathbf{r}} := \left(\frac{\partial}{\partial x}, \frac{\partial}{\partial y}, \frac{\partial}{\partial z} \right) \tag{2.7}$$

The coordinate $\mathbf{r_e}$ incorporates both electron coordinates $\mathbf{r}_1$ and $\mathbf{r}_2$; the reduced mass μ in equations (2.4) and (2.5) refers to the reduced *nuclear* mass

$$\mu := \frac{m_3 \cdot m_4}{m_3 + m_4} \tag{2.8}$$

The energy eigenvalues and E and E' in equations (3.1) and (3.2) only differ in terms of the translational energy, a quantity that is irrelevant for most spectroscopic purposes. It is

worthwhile noting, that the Hamiltonian $\hat{H}_0$ in equation (2.3) contains the kinetic energies of the electrons, and the total Coulomb interaction potential, but the kinetic energy of the nuclei is not included: $\hat{H}_0$ can therefore be interpreted as the Hamiltonian of the system for infinitely heavy, i.e., resting nuclei; this approach is often also referred to as the ***clamped nuclei approximation***. The eigenvalue equation corresponding to this situation is

$$\hat{H}_0 \psi_n(\mathbf{r_e}, \mathbf{r}) = E_n^0(r) \psi_n(\mathbf{r_e}, \mathbf{r}) \tag{2.9}$$

The above equation thus describes the dynamics of the electrons for *fixed* internuclear distance $\mathbf{r} = (x, y, z)$, consequently the energy eigenvalues E_n^0 in equation (2.9) only depend on the norm $r := |\mathbf{r}|$ of the vector $\mathbf{r}$. The index n in (2.9) indicates the *level* of electronically excited states. $n = 0$ designates the electronic ground state of the hydrogen molecule, which shall be assumed throughout the whole thesis (unless explicitly stated otherwise), since the electronic excitation is extremely large, as compared to the vibrational and rotational excitations: For the hydrogen molecule, we have over 90000 cm^{-1} for the *n*=0 to *n*=1 electronic transition, as compared to 4150 cm^{-1} and 121 cm^{-1} for the vibrational and rotational transitions, respectively [Herzberg 1950]. For each level of electronic excitation *n* there is a set of eigenfuctions ψ_0 that parametrically depends on the nuclear distance. Equation (2.9) cannot be solved analytically but numerically to any desired precision.

The ***Born-Oppenheimer approximation*** (or *adiabatic approximation*) is a consequence of the mass ratio of nuclei and electrons, which is $m_P / m_e \approx 1837$ for H_2. This leads to a slow nuclear motion as compared to the electron dynamics. It can be shown – cf. e. g. [van Kranendonk 1983, p. 1 f.] – that for the electronic ground state the Born-Oppenheimer approximation leads to the following separation equation

$$\Phi_0(\mathrm{r}_e;\mathrm{r}) = \chi_0(\mathrm{r})\psi_0(\mathrm{r}_e;\mathrm{r}) \tag{2.10}$$

where $\psi_0(\mathrm{r}_e;\mathrm{r})$ denotes an eigenfunction of the electronic ground state according to equation (2.9) and $\chi_0(\mathrm{r})$ denotes a solution to the following eigenvalue equation

$$\left[\frac{-\hbar^2}{2\mu}\vec{\nabla}_{\mathrm{r}}^2 + U_0(r)\right]\chi_0(\mathrm{r}) = E_0\chi_0(\mathrm{r}) \tag{2.11}$$

In the above equation $U_0(r)$ represents an *effective internuclear potential*, which can be obtained by using the eigenfuctions $\psi_0(\mathrm{r}_e;\mathrm{r})$ of equation (2.9):

$$U_0(r) = \int \psi_0(\mathrm{r}_e;\mathrm{r})\left(\hat{H}_0 + \hat{H}_1 + \hat{H}_2\right)\psi_0(\mathrm{r}_e;\mathrm{r})\,d\mathrm{r}_e \tag{2.12}$$

$$= E_0^0(r) + \underbrace{\int \psi_0(\mathrm{r}_e;\mathrm{r})\left(\hat{H}_1 + \hat{H}_2\right)\psi_0(\mathrm{r}_e;\mathrm{r})\,d\mathrm{r}_e}_{=:\Delta U_0(r)} \tag{2.13}$$

The effective internuclear potential term does not depend on the electronic coordinates. The term $\Delta U_0(r)$ defined in equation (2.13) is referred to as the *diagonal correction* due to the nuclear motion [van Kranendonk 1983]. In this treatment of the hydrogen molecule, the following simplifications are made:

1. The relativistic corrections of the potential due to the relativistic motion of the electrons, which are of the order 10^{-5} $U_0(r)$ – cf. [van Kranendonk 1983, p. 5] – are not considered in equation (2.13), cf. [Kolos and Wolniewicz 1964a].
2. Quantum electrodynamical corrections, due to the Lamb shift (i.e., the interaction of the electrons with the zero-point radiation field) are neglected as well in equation (2.13), cf. [Garcia 1966].

Equation (2.11) is an equivalent reformulation of the original Schrödinger equation (3.1). The advantage resulting from the reformulation is that equation (2.11) has to be solved in a three-dimensional space given by the coordinates of internuclear distance. The separability of the wave function $\chi_0(\mathrm{r})$ is a consequence of the spherical symmetry of the effective internuclear potential $U_0(r)$: The wave function $\chi_0(\mathrm{r})$ thus can be written as

$$\chi_0(\mathrm{r}) = f_{vJ}(r) Y_J^M(\vartheta,\varphi) \tag{2.14}$$

where the factor $f_{vJ}(r)$ depends only on the absolute value, *r*, and the factor $Y_J^M(\vartheta,\varphi)$ is a spherical harmonic (cf. appendix A1.3: Spherical harmonics) that depends only on the orientation of the vector of internuclear separation **r**. The spherical harmonics describe the probability of finding the molecule in a certain orientation (ϑ,φ), and thus the rotational dynamics of the molecule. The index ν in the equation above designates the vibrational excitation of the molecule in the potential $U_0(r)$. Since the hydrogen molecule is a linear molecule there is only one vibrational mode.

One approach to determine the wave functions of the molecular vibrations $f_{vJ}(r)$ is obtained by introducing the radial functions $u_{vJ}(r) := r f_{vJ}(r)$ in equation (2.11), which yields the following one-dimensional radial equation

$$\left[\frac{-\hbar^2}{2\mu}\frac{d^2}{dr^2} + U_0(r) + \frac{J(J+1)\hbar^2}{2\mu r^2}\right] u_{vJ}(r) = E_{vJ} u_{vJ}(r) \tag{2.15}$$

where $E_{vJ} \equiv E_0$. The above equation can be integrated numerically provided the effective internuclear potential $U_0(r)$ is given.

The *Dirac notation* for the rovibrational wave functions is defined as

$$\left|J,M\right\rangle_v := \chi_0(\mathrm{r}) = f_{vJ}(r) Y_J^M(\vartheta,\varphi) \tag{2.16}$$

and is particularly useful for computing matrix elements.

The ***Dunham model*** is a universal method for describing the rovibrational energies of a diatomic molecule, which can be used to solve equation (2.15): Using the nuclear masses and the effective internuclear potential a new set of constants is determined, with which the rovibrational energies of the molecule are computed by means of a series expansion. The starting point of this method is the Schrödinger equation (2.15), which is generally valid for the rovibrational dynamics of diatomic molecules. If we introduce a new transformed coordinate

$$x := \frac{r - r_e}{r_e} \tag{2.17}$$

where r_e denotes the equilibrium internuclear distance, at which the effective potential $U_0(r)$ takes a minimum value (equilibrium distance), we can expand the potential into a Taylor series

$$U_0(r) = hca_0x^2(1 + a_1x + a_2x^2 + a_3x^3 + O(x^4)) . \tag{2.18}$$

The new variable *x* is dimensionless and describes the displacement of the internuclear distance from the equilibrium distance. The constant a_0 represents the *deformation for the harmonic part of the potential* and has the dimension of wave number (cm^{-1}). The constants $a_1, a_2, a_3, ...$ are dimensionless *anharmonicity constants* of the vibrational potential, and are known as the ***Dunham potential constants***. For a purely harmonic potential, the vibrational wave number of the diatomic molecule is determined by the deformation constant by means of the following relation:

$$\tilde{\nu}_e = \sqrt{\frac{\hbar a_0}{\pi \mu c r_e^2}} \tag{2.19}$$

where μ is the reduced nuclear mass. The rotational term in equation (2.15) can also be expressed in terms of the dimensionless variable *x* as

$$U_J(r) = \frac{J(J+1)\hbar^2}{2\mu r^2} = hcB_e \frac{J(J+1)}{(x+1)^2} . \qquad (2.20)$$

In equation (2.20) B_e is the equilibrium rotational constant of the molecule, which has the dimension of wave number like $\tilde{\nu}_e$. For the H_2 molecule these two constants are:

$$\tilde{\nu}_e = 4401.21 \ cm^{-1}$$
$$B_e = 60.853 \ cm^{-1}$$

cf. [Herzberg 1950]. By means of equations (2.18) and (2.20), the total potential term $U_0(r)+U_J(r)$ can be expanded into a power series in the coordinate *x*. Starting with this approach for the potential, Dunham deduced the following double power series expansion for the energy eigenvalues of a vibrating rotor using the ***Wentzel-Kramers-Brillouin (WKB) method*** [Dunham 1932]:

$$E_{vJ} = hc\sum_{i,j} D_{ij}(v+\tfrac{1}{2})^i \left[J(J+1)\right]^j \qquad (2.21)$$

The coefficients D_{ij} in this series are termed the ***Dunham coefficients*** of the molecule. In the paper cited above, Dunham deduced analytical expressions for the Dunham coefficients D_{ij} as a function of $\tilde{\nu}_e$, B_e and the potential constants a_n. For many purposes, though, these analytical expressions are not of interest, since the Dunham expansion (2.21) is used to empirically fit the Dunham coefficients to the observed transition frequencies, as e.g. in the data reduction of diatomic molecule spectra. This empirical procedure was also used to obtain the Dunham coefficients for the free H_2 molecule listed in Table.2-1, cf. [Foltz, Rank et al. 1966] and [Fink, Wiggins et al. 1965].
The equilibrium internuclear distance r_e for hydrogen has the value

$$r_e = 1.441 \ a.u. = 0.762 \ \text{Å}$$

according to *ab initio* computations, cf. [Kolos and Wolniewicz 1964b]. However, the expectation value for the internuclear distance in the ground state is slightly larger than this value due to the zero-point energy. Table 2-2 lists a few adiabatic matrix elements

$$r_{vv'} := \langle v | r | v' \rangle \tag{2.22}$$

for the internuclear separation of the hydrogen molecule in terms of its vibrational excitation in the rotational ground state.

Table.2-1: Dunham coefficients for the H_2 molecule

ij	D_{ij} [cm^{-1}] [a]	D_{ij} [cm^{-1}] [b]
10	4401.21	4401.213
20	-121.34	-121.336
01	60.853	60.853
11	-3.062	-3.0622
30	0.831	0.8129
21	0.058	0.0577
02	-0.0467	-0.0471
31	0.0051	--
12	0.0018	0.00274
03	5×10^{-5}	4.9×10^{-5}
22	-1.4×10^{-5}	--
13	--	-5×10^{-6}

a [Foltz, Rank et al. 1966]
b [Fink, Wiggins et al. 1965]

***Table 2-2**: Adiabatic matrix elements for the internuclear separation in the H_2 molecule*

vv'	$r_{vv'}$ [a.u.]	$r_{vv'}$ [Å]
00	1.4484 [a]	0.7662
11	1.5447 [a]	0.8172

a [Kolos and Wolniewicz 1964b]

2.1.2 Multipole moments of the hydrogen molecule

The hydrogen molecules do not possess a permanent dipole moment, but it possesses higher order moments of its molecular charge distribution. We can expand the electrostatic potential for any given finite charge distribution $\rho(\mathbf{r})$ by means of the *Racah spherical harmonics*[20]

$$\phi(R) = \sum_{l,m} Q_{lm} \frac{1}{R^{l+1}} C^*_{lm}(\Theta, \Phi), \tag{2.23}$$

where $C^*_{lm}(\vartheta, \varphi)$ denotes the complex conjugate of the Racah spherical harmonics, cf. Appendix A, and Q_{lm} denotes the *spherical multipole moments* defined by

$$Q_{lm} = \int \rho(\mathbf{r}) r^l C_{lm}(\vartheta, \varphi) d\mathbf{r}. \tag{2.24}$$

In equations (2.23) and (2.24), we used the definitions $\mathbf{R} = (R, \Theta, \Phi)$, $\mathbf{r} = (r, \vartheta, \varphi)$, $d\mathbf{r} = r^2 dr \sin\vartheta d\vartheta d\varphi$, and by definition $R > \mathbf{max}_{\rho(\mathbf{r})\neq 0} \{ r = |\mathbf{r}| \}$. It is a general theorem of classical electrodynamics that a finite number of spherical multipole moments Q_{lm} suffice to represent any given finite charge distribution $\rho(\mathbf{r})$. Because of the large intramolecular separation in solid hydrogen, it is useful to keep in mind that in general the greater the distance *R* is, the less terms one needs in the multipole expansion (2.23) for the representation of the potential.

The two lowest-order multipole moments in the multipole expansion are the ***total charge*** q of the charge distribution $\rho(\mathbf{r})$

$$Q_{00} \equiv q, \tag{2.25}$$

and the spherical components of the ***dipole moment*** μ_m

$$Q_{1m} \equiv \mu_m. \tag{2.26}$$

For the hydrogen molecule, these two lowest-order multipole moments vanish, i.e. ,

[20] Cf. e.g. [Jackson 1999], p. 145f.

$$q = \mu_m \equiv 0 \,. \tag{2.27}$$

Since in the case of the hydrogen molecule the potential is cylindrically symmetric, i.e. , $\rho(\mathbf{r}) = \rho(r, \vartheta)$, it is obvious that only the moments with $m = 0$ contribute in the expansion (2.23). This leads to a substantial simplification in the case of the hydrogen molecule, as there remains only one multipole moment for the order l of the multipoles yielding:

$$Q_{l0} = \int \rho(\mathbf{r}) r^{2l} P_l\ (\cos \vartheta) dr \sin \vartheta d\vartheta \tag{2.28}$$

in which $P_l\ (\cos \vartheta)$ denotes a *Legendre polynomial*. In the case of hydrogen molecules, we can replace the charge density in the above equation by the discrete charge distribution of the electrons and nuclei of the hydrogen molecule, with the coordinates given in (2.2) such that the integral is replaced by a simple summation yielding for the multipole moment Q_l

$$Q_l = Q_l(\mathbf{r}_e; r_3, r_4) = \sum_{i=1}^{4} q_i r_i^l P_l(\cos \vartheta_i) \tag{2.29}$$

with the point charges at $\mathbf{r}_i$. For a *homonuclear* molecule, the center of mass is in the origin of the coordinate system, such that we have $\mathbf{r}_4 = -\mathbf{r}_3$ in this case. Now we can make use of the symmetry of the Lengendre polynomials to further simplify the equations.

For *even* l we have

$$P_l(\cos \vartheta_3) = P_l(\cos \vartheta_4) \ \Rightarrow \ Q_l = Q_l(\mathbf{r}_e; r) \tag{2.30}$$

with

$$r := |r_3 - r_4| \,. \tag{2.31}$$

For *odd* l we have

$$P_l(\cos \vartheta_3) = -P_l(\cos \vartheta_4) \ \Rightarrow \ Q_l \equiv 0 \,. \tag{2.32}$$

For the homonuclear hydrogen isotopomers, all multipole moments of odd order vanish. Applying the adiabatic approximation, we obtain the following equation for the even-order multipole moments

$$Q_l(r) = \int \left|\Phi_0\left(\mathbf{r}_e;r\right)\right|^2 Q_l\left(\mathbf{r}_e;r\right) d\mathbf{r}_e \tag{2.33}$$

by virtue of the wave functions of the electronic ground state given in equation (2.10). $Q_l(r)$ is therefore termed as *adiabatic multipole moment*.

Given the radial wave functions $u_{vJ}(r)$ of the hydrogen molecule defined as solutions of equation (2.15), it is possible to define the so-called adiabatic matrix elements between different rovibrational states of the hydrogen molecule

$$\left\langle vJ \left| Q_l \right| v'J' \right\rangle := \int_0^\infty u_{vJ}(r) Q_l(r) u_{v'J'}(r) dr\,. \tag{2.34}$$

Numerical methods for computing these adiabatic matrix elements are discussed in [MISHRA and BALASUBRAMANIAN 1997].

2.1.3 Polarizability of the hydrogen molecule

Because of its importance for the Raman scattering, the polarizability of the hydrogen molecule shall be discussed briefly. The mathematical description of the molecular polarizability is achieved by the definition of the *polarizability tensor*. The homonuclear hydrogen molecules do not possess a permanent dipole moment, but due to the action of an electric field, a displacement between the negative and the positive charge distribution is induced. In the case of sufficiently weak electric fields, we can represent the induced dipole moment as a linear function of the electric field. We define the (linear) *polarizability tensor* in Cartesian coordinates by

$$\mu_i(r) := \sum_{i,j} \alpha_{ij}(r) E_j \tag{2.35}$$

where $i, j \in \{X, Y, Z\}$ are the Cartesian components of the nuclear coordinates, and E_j and μ_i are the Cartesian components of the electric field and of the induced electric dipole moment, respectively. The (linear) polarization tensor is a tensor of rank two, and depends on the internuclear distance r in the adiabatic approximation.

As we have seen in chapter 1, in order to understand the vibrational Raman spectrum, the polarizability tensor has to depend on the vibrational coordinates.

A graphical representation of the polarizability tensor is given by the ***polarizability ellipsoid***, which is determined by the following equation, cf. e.g. [Long 2002]:

$$\alpha_{xx}x^2 + \alpha_{yy}y^2 + \alpha_{zz}z^2 + 2\{\alpha_{xy}xy + \alpha_{yz}yz + \alpha_{zx}zx\} = 1, \tag{2.36}$$

in which α_{ij}, $i, j \in \{x, y, z\}$ are the Cartesian components of the polarizability tensor $\vec{\vec{\alpha}}$

$$\vec{\vec{\alpha}} := \begin{pmatrix} \alpha_{xx} & \alpha_{xy} & \alpha_{xz} \\ \alpha_{yx} & \alpha_{yy} & \alpha_{yz} \\ \alpha_{zx} & \alpha_{zy} & \alpha_{zz} \end{pmatrix}. \tag{2.37}$$

The polarizability ellipsoid is shown in **Figure 2-1**.

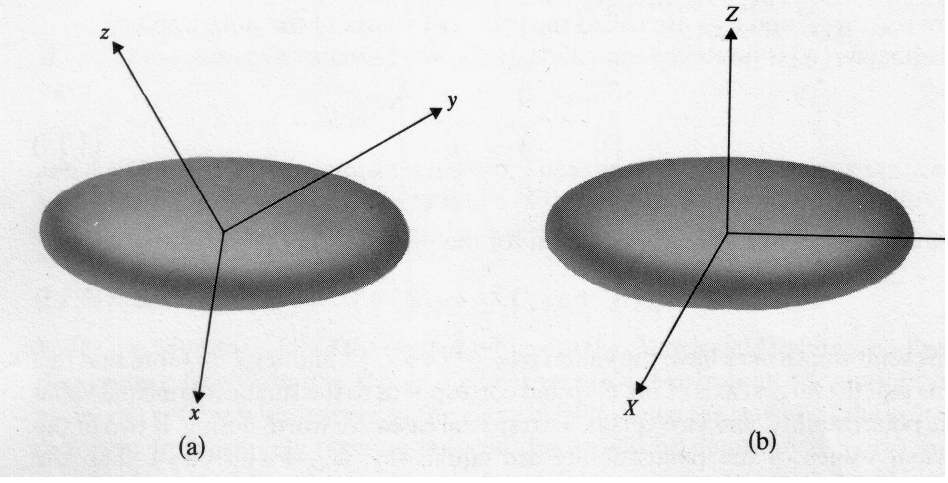

Figure 2-1: *The polarizability ellipsoid. Case (a): principal axes not coincident with system axes, case (b): principal axes coincident with system axes.*[21]

It can be shown that only along the directions of the principal axes, the direction of the induced electric dipole moment $\mathbf{P}$ is the same as the direction of the external electric

field $\mathbf{E}$: In the molecular principal axis system (x, y, z), the polarizability tensor is diagonal.

In the case of the cylindrically symmetric hydrogen molecule, we have

$$\alpha_{xx}(r) = \alpha_{yy}(r) =: \alpha_{\perp}(r), \tag{2.38}$$

in which $\alpha_{\perp}(r)$ is called the *perpendicular component* of the polarizability. The *parallel component* of the polarizability is given as

$$\alpha_{zz}(r) =: \alpha_{\parallel}(r). \tag{2.39}$$

This means that the polarizability of the hydrogen molecule is completely determined by the two scalar values $\alpha_{\perp}(r)$ and $\alpha_{\parallel}(r)$. It is common, though, to decompose the polarizability into an *isotropic* and an *anisotropic* part $\alpha(r)$ and $\gamma(r)$, respectively by the following definitions:

$$\alpha(r) := \frac{1}{3}\left(\alpha_{xx}(r) + \alpha_{yy}(r) + \alpha_{zz}(r)\right) = \frac{1}{3}\left(2\alpha_{\perp}(r) + \alpha_{\parallel}(r)\right), \tag{2.40}$$

$$\gamma(r) := \left(\alpha_{\parallel}(r) - \alpha_{\perp}(r)\right). \tag{2.41}$$

In analogy to the case of the multipole moments and in the case of the isotropic and anisotropic parts of the polarizability, one can compute the adiabatic matrix elements by using the radial wave functions $u_{vJ}(r)$, cf. the previous paragraph.

2.1.4 Ortho- and para-hydrogen: The nuclear spin modifications of the hydrogen molecule

2.1.4.1 Introduction: The influence of nuclear spin upon the structure of rotational spectra

In rotational spectra and rovibrational spectra of homonuclear diatomic atoms like H_2, N_2, and O_2, and more generally in the spectra of molecules possessing a center of inversion, like CO_2, there is a characteristic difference in line intensities between lines

[21] from [Long 2002].

that belong to *even* rotational quantum states *J*, as compared to states possessing an *odd* rotational quantum number *J*, see for example **Figure 2-2**, which shows the rovibrational Raman spectrum of the di-nitrogen isotopomer $^{14}N_2$. The Q-branch ($\Delta J=0$) appears in the centre of **Figure 2-2** (at approximately 2330 cm^{-1}) as a broad line. The change in intensities in consecutive lines with an intensity ratio of 1:2 can be seen very nicely for nitrogen molecules with $I(^{14}N)=1$. This effect is caused by the influence of the nuclear spin upon the spectra, and more precisely it is a consequence of the ***symmetrization postulate***: The nuclear spin influences the incidence with which a certain molecular state can be realized. This phenomenon has to be kept apart from the hyperfine structure splitting, which is due to the interaction between nuclear spin and magnetic moment of the nuclei and the electron shell of the molecule and results in a different and much weaker effect upon the electronic spectra. For homonuclear molecules, the observed change in intensity in the spectra is due to the effect of the nuclear spin upon the symmetry of the *total* wave function of the molecular state.

This fact was observed in rotational Raman spectrum of gaseous N_2 as early as 1929 by F. Rasetti[22] [Rasetti 1929; Stoicheff 2002], and explained by Heitler and Herzberg in the same year [Heitler and Herzberg 1929]: The relation of the line intensities in the $^{14}N_2$ spectrum is explained by the ^{14}N nuclei being bosons - not fermions as previously believed - since the theories of that time assumed nuclei to be composed of protons and electrons, as neutrons were unknown at that time.

[22] Rasetti discovered some key processes leading to nuclear fission together with E. Fermi.

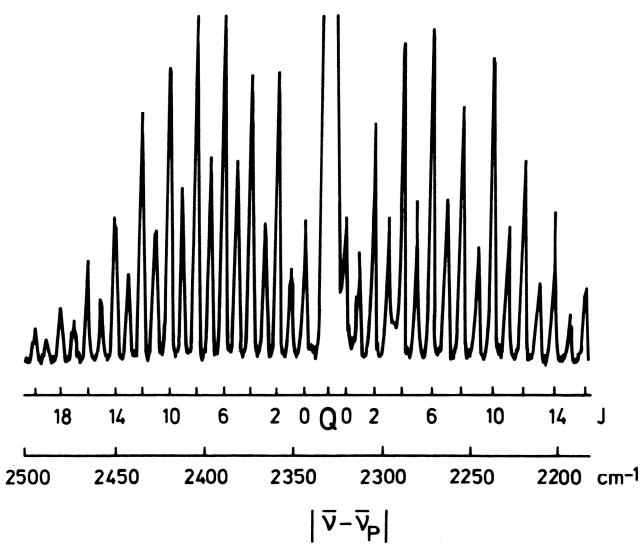

Figure 2-2: *Rovibrational Raman spectrum of di-nitrogen, $^{14}N_2$. Reproduction according to Hellwege in [Haken and Wolf 1998, p. 248].*

As an example, let us consider the H_2 molecule, see **Figure 2-3**. Both nuclei in the hydrogen molecule are fermions possessing spin ½. There are two different ways these spins can be aligned: *parallel* or *anti-parallel*. In the first case, in which the proton spins are aligned parallel, the total nuclear spin of the molecule is $I = 1$. In this case, the spin wave function is *symmetrical* upon particle permutation. This isotopomer of molecular hydrogen is termed *ortho*-hydrogen, *o*-H_2. In the second case, the proton spins are aligned *anti-parallel*, the total nuclear spin in this case is $I = 0$, the total nuclear spin wave function being *anti-symmetrical* upon particle permutation. This isotopomer is termed *para*-hydrogen, *p*-H_2. The statistical weight of those two isotopomeres is **3:1**, cf. the following paragraph.

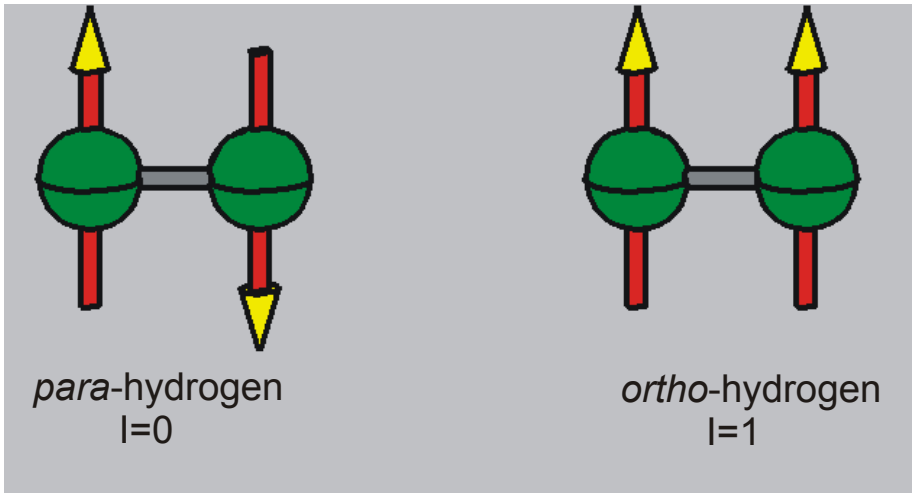

Figure 2-3: *Ortho- and para-hydrogen, the two spin-isomers of the H_2 molecule.*

2.1.4.2 Nuclear spin modifications of the hydrogen molecule

The homonuclear isotopomeres of the hydrogen molecule quantum mechanically represent a system of identical particles. This statement refers to the *electrons* as well as to the *nuclei*, and implies that the rules of quantum mechanics have to be applied for the hydrogen molecule: The *symmetrization postulate* requires the ***total*** wave function of the hydrogen molecule to have a definite parity, i. e., either positive or negative, with respect to particle commutation. If the commutable particles are *bosons* (particles with integer spin), the parity has to be *positive*, whereas for *fermions* (particles with half-integer spin) the parity is required to be *negative*. The latter case is also known as the ***Pauli exclusion principle*** [Pauli 1925; Pauli 1940; Pauli 1946][23].

The total wave function of a system consisting of many particles can be represented by a linear combination of the tensor products of single particle wave functions describing the particles constituting that system. A particle with spin *S* is described by the spin states $|S,M\rangle$ with $M \in \{-S,-S+1,...,S-1,S\}$, cf. Appendix A1: The mathematical treatment of spin. In this description, the quantum number *S* can posses integer as well as half-integer values. The multiplicity of the spin state $|S,M\rangle$ is (2*S*+1). The total spin wave function of a system consisting of two particles with spin S, $|S,M_1\rangle$ and $|S,M_2\rangle$, is given by equation (6.42) in appendix A1.4: Clebsch-Gordan coefficients, which applied to the present case results in

$$|I,M_I\rangle = \sum_{M_1,M_2} C^{S,S,I}_{M_1,M_2,M_I} |S,M_1\rangle_1 \otimes |S,M_2\rangle_2 . \qquad (2.42)$$

In equation (2.42), *I* is the total spin, which can take values from 0 to 2*S*. The definite parity of the total spin wave function $|I,M_I\rangle$ follows from the symmetry relations of the *Clebsch-Gordan coefficients* $C^{m_1,m_2,m}_{j_1,j_2,j}$, cf. Appendix A1.4: Clebsch-Gordan coefficients, p. 99f.

There are two distinguished nuclear spin modification of the H_2 molecule, *ortho*-H_2 and *para*-H_2. The nuclear spin wave function of *ortho*-H_2 has positive parity, and that of *para*-H_2 has negative parity with respect to nuclear commutation. The nuclei of the H_2 molecule are protons, and thus fermions with nuclear spin quantum number *S*=½. If we adopt the following abbreviatory notation for the one-particle spin wave functions

$$\left|\uparrow\right\rangle = \left|S = \frac{1}{2}, M_S = \frac{1}{2}\right\rangle \tag{2.43}$$

$$\left|\downarrow\right\rangle = \left|S = \frac{1}{2}, M_S = -\frac{1}{2}\right\rangle \tag{2.44}$$

we obtain the following possible coupled nuclear spins for the H_2 molecule using equation (2.42) (or simply by the addition of two spin-½'s, as put forward in Appendix A1.2: Addition of two spins ½'s)

***o*-H_2:**
$$\begin{cases} \left|I = 1, M_I = 1\right\rangle = \left|\uparrow\right\rangle_1 \otimes \left|\uparrow\right\rangle_2 \\ \left|I = 1, M_I = 0\right\rangle = \frac{1}{\sqrt{2}}\left(\left|\uparrow\right\rangle_1 \otimes \left|\downarrow\right\rangle_2 + \left|\downarrow\right\rangle_1 \otimes \left|\uparrow\right\rangle_2\right) \\ \left|I = 1, M_I = -1\right\rangle = \left|\downarrow\right\rangle_1 \otimes \left|\downarrow\right\rangle_2 \end{cases} \tag{2.45}$$

***p*-H_2:**
$$\left|I = 0, M_I = 0\right\rangle = \frac{1}{\sqrt{2}}\left(\left|\uparrow\right\rangle_1 \otimes \left|\downarrow\right\rangle_2 - \left|\downarrow\right\rangle_1 \otimes \left|\uparrow\right\rangle_2\right). \tag{2.46}$$

It is obvious that only the total wave function (2.46) of *p*-H_2 with total nuclear spin *I*=0 has *negative* parity upon permutation of the nuclei. In contrast to that, all the three wave functions describing *o*-H_2 (*I*=1) have *positive* parity with respect to permutation of the nuclei.

According to equations (2.10), (2.14) and (2.42), the *total* wave function of the H_2 molecule (including the nuclear spins) can be written as

$$\Psi_{tot} = \Phi_0\left(\mathrm{r}_e; \mathrm{r}\right) f_{vJ}(r) Y_J^M(\vartheta, \varphi)\left|I, M_I\right\rangle. \tag{2.47}$$

The electronic wave function $\Phi_0\left(\mathrm{r}_e; \mathrm{r}\right)$ and the vibrational wave functions possess *positive* parity with respect to the nuclear interchange operation P_{12}, as these depend only on the *magnitude* of the internuclear separation r. Thus, the interchange operation only acts on the rotational part $Y_J^M(\vartheta, \varphi)$ and nuclear spin part $\left|I, M_I\right\rangle$ of the wave function

[23] The *Pauli exclusion principle* was formulated in 1924 [Pauli 1925], well before the "modern" quantum theories of Heisenberg and Schrödinger, and states that the ***total*** wave function of *fermions* is *anti-symmetrical* with respect to particle permutation. Pauli later derived it from the more general *spin-statistics theorem* [Pauli 1940, 1964].

$$P_{12}\Psi_{tot} = \Phi_0\left(\mathrm{r}_e;\mathrm{r}\right) f_{vJ}(r) P_{12}\left(Y_J^M(\vartheta,\varphi)\middle|I,M_I\right\rangle\right). \tag{2.48}$$

In other words, **the parity of the total molecular wave function is equal to the parity of the product of the rotational wave function and the nuclear spin wave function**. The nuclear interchange operation P_{12} in this case is identical to the reflection at the center of mass (or origin, in this case) of the molecule O^*, which for the rotational part yields

$$P_{12}Y_J^M(\vartheta,\varphi) = O^* Y_J^M(\vartheta,\varphi) = Y_J^M(-\vartheta,-\varphi) = (-1)^J Y_J^M(\vartheta,\varphi) \tag{2.49}$$

according to the symmetry relation of the spherical harmonics, cf. Appendix A1.3: Spherical harmonics, equation (6.39). The rotational wave functions thus have *positive* parity for *even* values of the molecular angular momentum quantum number *J*, and *negative* parity for *odd J* values. This result is of major importance for the homonuclear hydrogens, since it implies that because of symmetry the spin-isomers of hydrogen and the quantum number *J* are linked together: Since the total molecular wave function has to be of negative parity for a *fermionic* system, the following angular momentum restriction rule applies to the H_2 molecule:

- for ***even*** rotational states (*J* = 0,2,4,…) only molecules with ***antiparallel*** nuclear spins can exist (*para*-H_2)

- for ***odd*** rotational states (*J* = 1,3,5,…) only molecules with ***parallel*** nuclear spins can exist (*ortho*-H_2).

A similar restriction for vibrational states does not exist. Between these two spin modifications of the H_2 molecule - which can be separated macroscopically ** - transitions are quantum-mechanically strictly forbidden. Only transitions within the term system with *even J* and within the term system with *odd J* are allowed, if the nuclei are strictly decoupled. The weak coupling between nuclear and electron spins however facilitates transitions between the two term systems with very small probability. The contribution of the relative nuclear spin orientation in the hydrogen molecule to the total energy of the molecule is very small (in the order of 10^{-5} cm^{-1}) and thus negligible for most considerations. As a consequence, in the limit of high temperatures (compared to the

characteristic rotational temperature of approximately 175 K for H_2) the ratio of *ortho*-H_2 and *para*-H_2 is **3:1**, corresponding to their different ***statistical weights*** [24].

But at very low temperatures only *para*-H_2 is stable because the lowest rotational level in *ortho*-H_2 is J=1 (i.e., the molecule is rotationally excited in that state), and as a consequence, *ortho*-H_2 is ***metastable***. However, the spontaneous conversion of *o*-H_2 into *p*-H_2 through a flip of nuclear spins occurs very slowly, in a timescale of many months.[25]

If we consider the rotational energy of the H_2 molecule - e. g. according to equation (2.21) – neglecting the vibrational excitation (which for ν=1 has a characteristic temperature of approx. 6300 K), we obtain the following *ortho*-H_2 to *para*-H_2 ratio of

$$\frac{N[o-H_2]}{N[p-H_2]} = \frac{3\sum_{J=1,3,5,\ldots} 2(J+1)e^{-\frac{E_{0J}}{kT}}}{\sum_{J=0,2,4,\ldots} 2(J+1)e^{-\frac{E_{0J}}{kT}}} \tag{2.50}$$

for the thermal equilibrium. The factor 3 in the numerator is the nuclear spin degeneracy factor for *o*-H_2. The *molar concentration* of *o*-H_2 in a sample of H_2 is defined as

$$X[o-H_2] = \frac{N[o-H_2]}{N[p-H_2]+N[o-H_2]}, \tag{2.51}$$

and yields $X[o-H_2] = \frac{3}{4} = 75\%$ in the high-temperature limit in thermal equilibrium, cf. the figure below.

[24] The degeneracy of a rotational level as a consequence of the nuclear spin I is termed the *statistical weight* of that level because it determines – together with the rotational degeneracy factor (2J+1) and the specific Boltzmann factor – the equilibrium distribution of the molecules over the rotational levels, cf. [van Kranendonk 1983, p. 25]. Because of the angular momentum restriction rule this means that (in the limit of high temperatures) there are three times more molecules in odd-J states than in even-J states for H_2 at thermal equilibrium.

[25] Cf. [Silvera 1980].

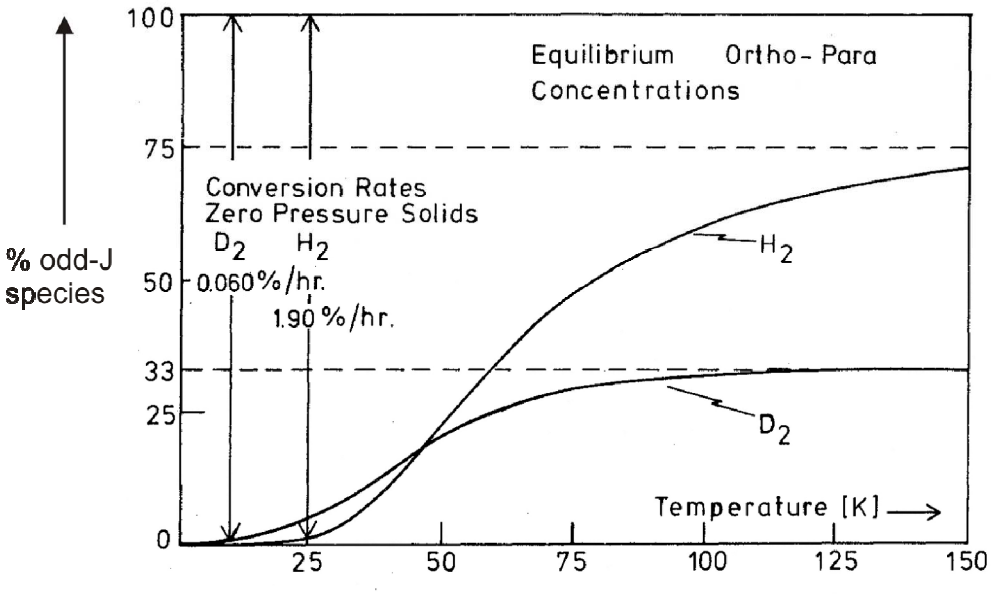

Figure 2-4: *Temperature dependence of homonuclear hydrogen odd-J species at thermal equilibrium. The dotted lines denote the high temerature asymptotic limits.*[26]

The deuterium molecule can be treated in a similar manner, but it has to be taken into account that the nuclei are *bosons* in this case with the nuclear spin quantum number I=1. In the case of the deuterium molecule, the *para*-deuterium spin isomer is that with the negative parity of the nuclear spin wave function (in analogy to the case of hydrogen), and the spin-isomer with positive parity of the nuclear wave function is called *ortho*-deuterium, such that we have the following angular momentum rule for the D_2 molecule:

- ***ortho*-D_2**: ***even*** J states – J = 0,2,4,…
- ***para*-D_2**: ***odd*** J states – J =1,3,5,…

In thermal equilibrium and in the limit of high temperatures, the ***abundance ratio*** of *ortho*-D_2 and *para*-D_2 is **2:1,** following the general rule

$$\frac{g_s}{g_a} = \frac{I+1}{I} \tag{2.52}$$

[26] from [Silvera 1980, p. 415]

for the ratio of the statistical weights of the symmetric (g_s) and anti-symmetric (g_a) nuclear spin wave function, respectively. The deduction of this general rule can be found e.g. in [Haken and Wolf 1998], p. 519f. The molar concentration of *para*-D_2 in a sample of D_2 is defined in analogy to the case of H_2, which explains why in the case of D_2 we have the following high-temperature limit in thermal equilibrium for the molar concentration of D_2: $X[p-D_2] = \frac{1}{3} = 33.\overline{3}\%$, cf. Figure 2-3.

2.2 The condensed phases of hydrogen molecules

2.2.1 Ortho-para conversion

The experimentally relevant question for our purpose is what happens to normal hydrogen gas when cooled down to cryogenic temperatures.

In the previous paragraph, we have seen that the transition of a H_2 (or D_2) molecule between an ortho and para state involves not only a transition of the form $\Delta J = \pm 1, \pm 3, ...$ in the rotational terms but due to the symmetrization postulate (or Pauli principle, in this case) also a change in the relative orientation of the two nuclear spins. In the H_2 molecule, this change can only be brought about by an inhomogeneous magnetic field that executes a differential torque between the two spins, or by the spin dependent interaction of the nuclei with an incident nuclear particle (e.g. a neutron).[27]

Since the nuclei in the D_2 molecule possess an electric quadrupole moment, conversion in D_2 molecules can also occur in an inhomogeneous electric field. In pure H_2 free from magnetic impurities, the nuclear spins and the rotational magnetic moments of the molecules cause the ortho-para conversion.

2.3 The condensed phases of hydrogen molecules

In the condensed phase, hydrogen has many remarkable features. Solid hydrogen is termed a ***quantum solid*** or ***quantum crysta***l. Except at ultra-high pressures, hydrogen forms a molecular crystal in which its constituents retain their to a high degree

[27] Very comprehensive treatments of ortho para conversion processes are found in e. g. in [van Kranendonk 1983, p. 256 ff.] and [Silvera 1980, p.414 ff.].

properties as individual molecules. For instance, the rotation of the molecules is observed even down to temperatures approaching 0 K.

The solid state properties of solid hydrogen are dominated by quantum effects, such as the so-called ***quasi-free rotation*** of the molecules in the lattice mentioned above. Quasi-free rotation can be understood as follows: In spite of the crystal lattice bond, the rotational quantum number *J* is a good quantum number, meaning that *J* is appropriate for the description of rotational states in the crystal.
Another remarkable effect is the very large amplitude of the zero-point lattice vibrations, which is still 18% of the nearest neighbour distance at temperatures approaching the absolute zero. At such values of the vibrational amplitude classical solids would melt. These quantum effects are a consequence of the weak intramolecular forces and the small mass and small moment of inertia of the hydrogen molecules and can be characterized by the de Boer parameter Λ^* and the ratio V_0 / R_0^3.

The de *Boer parameter* Λ^* is defined as

$$\Lambda^* := \frac{h}{R_0 \sqrt{m\varepsilon}} \tag{2.53}$$

and thus is given by the ratio of the de Broglie wavelength of relative motion to the distance of closest approach R_0. The ratio of the volume occupied by the particles at 0 K, V_0, and the volume they would occupy in a classical lattice, which is proportional to R_0^3, is another measure of the zero-point vibration.

Table 2-1: *Comparison of quantum properties of different materials (used for matrix isolation spectroscopy). According to [Toennies and Vilesov 2004].*

species	ε [K]	R_m [Å]	α [Å^3]	Λ*	V_0/R_0^3	T_{tp} [K]
Xe	283	4.37	4.01	0.06	0.933	161
Kr	201	4.01	2.48	0.11	0.951	116
Ar	143	3.76	1.64	0.20	0.976	83.8
Ne	43.3	3.09	0.397	0.62	1.09	24.6
H_2	34.8	3.44	0.803	1.97	1.32	14
^{4}He	11.0	2.97	0.205	2.87	1.87	no t.p.
^{3}He	11.0	2.97	0.205	3.31	2.82	no t.p.

In this table, ε is the potential well depth (expressed in Kelvin), R_m is the well position, α is the dipole polarizability, and T_{tp} is the triple point temperature.

2.3.1 The intermolecular potential

The intermolecular potential is the key to understanding and describing the condensed phases of any substance. This has been addressed in detail by Silvera and van Kranendonk [Silvera 1980; van Kranendonk 1983]. In this paragraph, I shall give a brief summary of the theory necessary for the understanding of the condensed phases of hydrogen molecules.

The *pairwise additive potentials* (or interactions) and *nonadditive potentials* (or interactions) have to be discerned. While the pairwise additive potentials account for many of the properties of the solid and liquid phase, the nonadditive potentials give rise to some distinguishing properties of solid hydrogen. Because the gas phase single molecule properties of the hydrogen molecules remain almost unvaried in the solid phase, only small corrections to the pair potentials of an isolated pair have to be amended in order to describe the properties of the solid.

2.3.1.1 Coordinate system for the description of the solid phase

In order to describe the solid phase, an adequate choice of the coordinate system has to be made. The definition of the set of variables describing two molecules is shown in **Figure 2-5**.

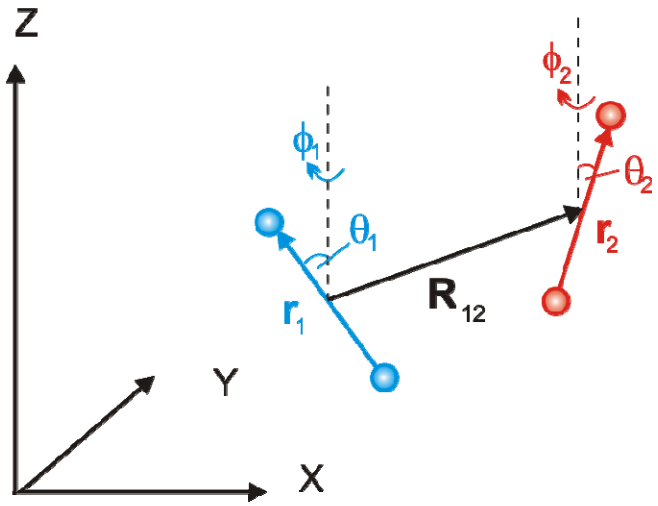

Figure 2-5: *Definition of variables for a pair of homonulear, diatomic molecules in the* ***crystal-fixed frame****. According to [van Kranendonk 1983].*

Here the coordinates (X,Y,Z) describe the *crystal-fixed frame*, and the vectors $\mathbf{r}_1$, $\mathbf{r}_2$ and $\mathbf{R}_{12}$, given by

$$\begin{aligned} \mathbf{r}_i &= (r_i, \Omega_i) = (r_i, \theta_i, \phi_i) \quad , i = 1,2 \\ \mathbf{R}_{12} &= (R_{12}, \Omega_{12}) = (R_{12}, \theta_{12}, \phi_{12}) \end{aligned} \tag{2.54}$$

suffice in order to define the pair configuration of two molecules 1 and 2 in the crystal fixed frame. $\mathbf{r}_i = (r_i, \Omega_i) = (r_i, \theta_i, \phi_i)$ are the rovibrational coordinates of molecule *i*=1,2 as defined by **Figure 2-5**, and the vector $\mathbf{R}_{12} = (R_{12}, \Omega_{12}) = (R_{12}, \theta_{12}, \phi_{12})$ is the vector of internuclear separation.

If the orientation of the molecules in the crystal-fixed coordinate system is not of relevance, the pair of molecules can be described in another coordinate system, which I shall refer to as the "***pair system"***, as described by van Kranendonk [van Kranendonk 1983]. We shall use this coordinate system throughout the paragraph for the description of hydrogen molecules in the solid phase. The variables are defined as shown in **Figure 2-6**.

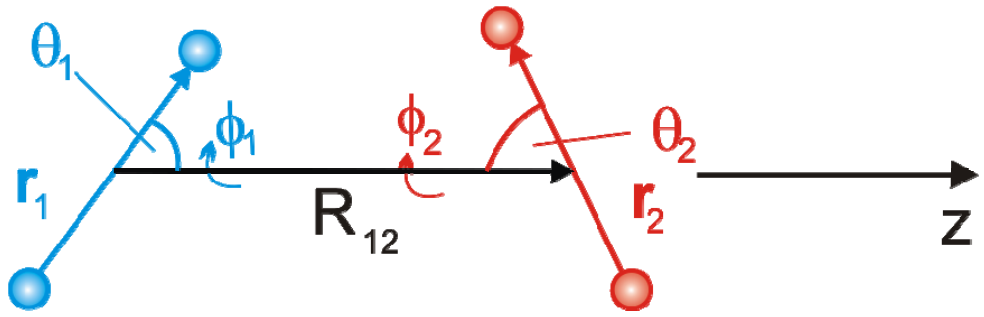

Figure 2-6: *Standard set of variables for a pair of homonuclear, diatomic molecules in the "**pair-system**". According to [van Kranendonk 1983].*

The z-axis of the pair system is defined by the intermolecular axis, such that the solid angle Ω_{12} describing the orientation of the intermolecular axis $\mathbf{R}_{12}$ is no longer required in the description. Also, the vector $\mathbf{R}_{12}$ reduces to the scalar value of the intermolecular distance $R_{12} =: R$. In order to distinguish between the pair system and the coordinate system shown in **Figure 2-5**, we shall denote the solid angles of the pair system by $\boldsymbol{\omega}_i$, $i = 1,2$.

2.3.1.2 Separation of the intermolecular potential

According to van Kranendonk, the potential energy terms can be separated into the following expressions:

$$\begin{aligned} &V(X) = V_0(R) + A(\boldsymbol{\omega}_1, \boldsymbol{\omega}_2, R) + F(r_1, r_2, R) + M(r_1, r_2, \boldsymbol{\omega}_1, \boldsymbol{\omega}_2, R) \\ &\textit{with } X = (r_1, r_2, \boldsymbol{\omega}_1, \boldsymbol{\omega}_2, R), \textit{ and} \\ &\left|M(r_1, r_2, \boldsymbol{\omega}_1, \boldsymbol{\omega}_2, R)\right| \ll \max\left\{\left|V_0(R)\right|, \left|A(\boldsymbol{\omega}_1, \boldsymbol{\omega}_2, R)\right|, \left|F(r_1, r_2, R)\right|\right\} \end{aligned} \tag{2.55}$$

in which the terms denote the *isotropic*, *anisotropic*, *vibrational*, and *mixed* (or *rotation-vibration*) parts of the potential.

The largest contribution to the potential $V(X)$ is given by the isotropic term, which describes the *van-der-Waals interaction*, and is independent of the rovibrational excitation of the molecules. Thus, the isotropic potential can be interpreted as a first-order approximation of the lattice potential energy of the crystal. In the case of solid hydrogen

with quasi-free rotational states, the anisotropic part $A(\omega_1, \omega_2, R)$ only contributes for molecules with $J \neq 0$.

2.3.1.3 The isotropic contribution

The isotropic pair potential according to Silvera and Goldman is shown in **Figure 2-7**. It has a potential well minimum of 34.3 K depth and a minimum internuclear distance of R_m=6.75 a.u. =3.57 Å.

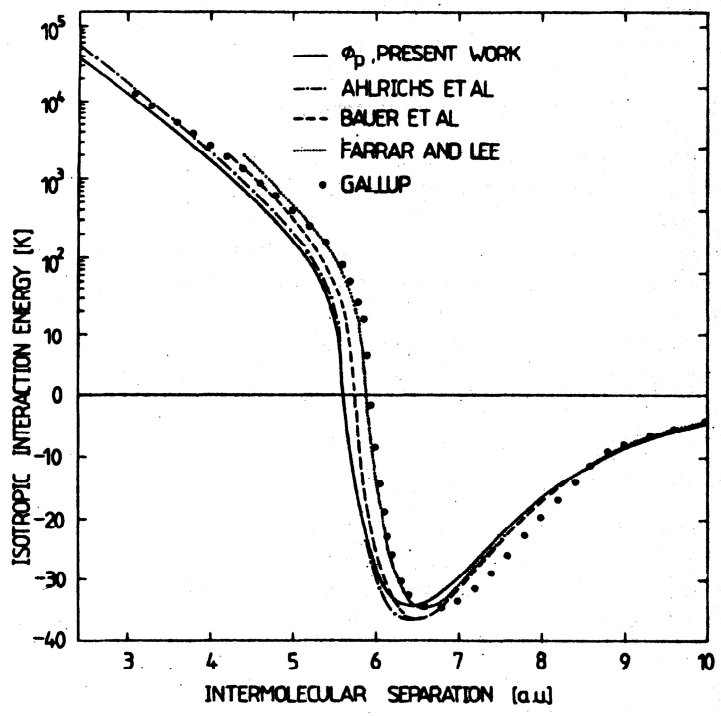

Figure 2-7: *Silvera-Goldman pair potential for hydrogen molecules. The solid line shows the results of ab initio calculations by Silvera and Goldman [Silvera and Goldman 1978].*

The anisotropic potential term and the vibrational potential term are addressed in detail in [Silvera 1980; van Kranendonk 1983] and shall not be discussed here.

2.3.1.4 The fcc and hcp crystal structures

Solid hydrogen crystals – both pure crystals and ortho/para mixtures – always have a *close-packed structure* in which every molecule is surrounded by twelve nearest neighbour molecules [van Kranendonk 1983]. The only ordered three-dimensional

structures are the hexagonal close-packed structure (hcp) and the face-centered cubic (fcc) structures, whereas there is an infinite variety of disordered close-packed structures. Pure para-hydrogen forms hcp-crystals, which has been proved by X-ray diffraction of p-H_2 crystals at T = 4 K as early as 1930 [Keesom, Smedt et al. 1930]. This fact can be very easily explained since the hcp structure has a slightly lower lattice energy of approximately 8.5 mJ/mol as compared to the fcc structure [Silvera 1980]. This small energy difference of the two different crystal structures becomes important when discussing the relation between ortho concentration in a crystal and crystal structure, since there is an anisotropic pair potential between two ortho molecules that can be of the order of some wavenumbers. Thus, hcp is not always the preferred crystal structure: It turns out that the crystal structure depends on many factors (temperature, ortho concentration, growing method and pressure), and also mixed structures were described [Silvera 1980].

2.3.1.5 Crystal growth methods

Though several methods for growing *p*-H_2crystal have been reported, e.g. the direct condensation from the gas phase at 7 K cell temperature [Weliky, Byers et al. 1994], we chose to grow the crystals from the pressurized liquid phase (at p=30 bar, T=14 K), since this method has been reported to produce crystals of highest optical quality and damage thresholds, cf. [Momose, Weliky et al. 1992; Weliky, Byers et al. 1994; Suzuki, Katsuragawa et al. 1998; Hakuta 2002]. These values for the pressure p and temperature T were chosen, because liquid hydrogen at 30 bar has the same density as solid hydrogen at 4.2 K, such that the crystal defects are minimized and the crystal can be cooled to the final temperature of 4 K or below temperature without cracking.

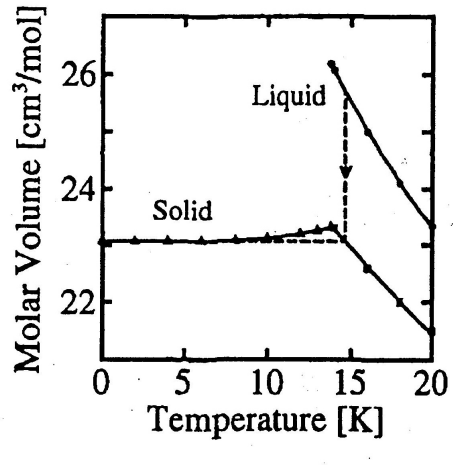

Figure 2-8: *Molar volume of liquid and solid hydrogen. According to [Souers 1986; Suzuki, Katsuragawa et al. 1998].*

Solid hydrogen has a large change in length of -3% upon cooling down from approximately 14 K to 4 K which leads to cracking if the crystal is cooled too fast, whereas with the growth from the pressurized liquid phase one does not encounter that problem, cf. [Suzuki, Katsuragawa et al. 1998].

Table 2-2: Properties of solid normal hydrogen and para-hydrogen. [a]

property	*n*-H_2	*p*-H_2
molar volume at 4.2 K [cm^3/mol]	22.82	23.06
molecular weight [u]	2.0157	2.0157
critical point pressure [bar]	13.15	12.928
critical point temperature [K]	33.19	32.976
boiling point temperature (1013 mbar) [K]	20.39	20.268

[a] according to [Souers 1986].

History of solid hydrogen spectroscopy

Because of the existence of two different spin-isomers of hydrogen with negative (*p*-H_2) and positive parity (*o*-H_2) with respect to nuclear permutation, an arbitrary mixture between molecules in the spherically symmetric rotational ground state J=0 (*p*-H_2) and molecules in the asymmetric rotational excited state J=1 (*o*-H_2) can be produced in the solid state with any desired ortho concentration, which allows the study of the anisotropic intermolecular interaction, cf. [van Kranendonk 1983].
But solid hydrogen is also an interesting system to study in molecular spectroscopy because it has an infrared absorption spectrum, while isolated hydrogen molecules in the electronic ground state do not possess any allowed dipole transitions due to the fact that isolated homonuclear diatomic molecules have no electric dipole moment. The first electronically excited state of the singlet state has an excitation energy of approximately 11.2 eV corresponding to approximately 90.300 wavenumbers, which lies in the UV, cf. [Herzberg 1950]. In the solid phase, there are infrared-active rovibrational transitions due to induced dipole moments as a consequence of the intermolecular interactions [van Kranendonk 1983].

It is intuitively clear that the lower the temperature of the crystal, the narrower the (vibrational) line widths are. Koroda, Koreeda, Hakuta et al. have studied the temperature dependence of the Raman line width for the $Q_1(0)$ vibrational transition in *para*-hydrogen crystals [Kuroda, Koreeda et al. 2003]. Their results are shown in **Figure 2-9** and **Figure 2-10**.

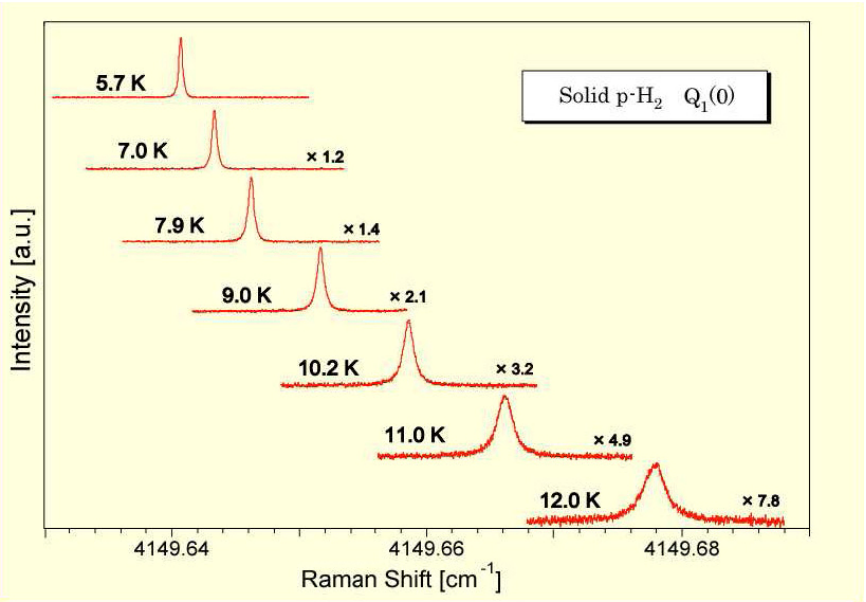

Figure 2-9: *Temperature dependence of the vibrational Raman line width and line positions, according to [Kuroda, Koreeda et al. 2003].*

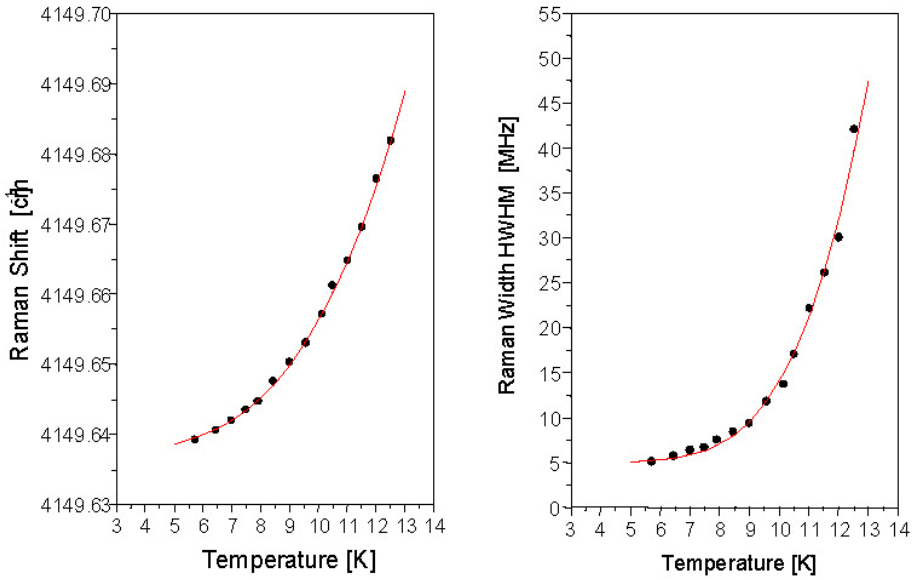

Figure 2-10: *Plot of temperature dependence of Raman line width and Raman shift in p-H_2 crystals, according to [Kuroda, Koreeda et al. 2003].*

Matrix isolation spectroscopy is a widely used method in chemical spectroscopy for the stabilization and detection of active molecules, and has been also used to study reactions, cf. e.g. [Momose, Miki et al. 1995; Momose, Katsuki et al. 1997; Momose, Masaaki et al. 1997; Momose, Hoshina et al. 1998; Tam, Fajardo et al. 1999; Bargheer, Dietrich et al. 2001; Berghof, Martins et al. 2002; Gühr and Schwentner 2005]. The technique relies on the vapor deposition of the unstable molecules onto a cryogenic surface, such that these molecules are deposited in combination with an excess amount of the matrix isolation species producing a crystal containing the molecules being investigated in a "diluted form" allowing, for example, IR-spectroscopic analysis of these molecules similar to gas-phase IR-spectroscopy. The crystal is generally an inert gas crystal and termed the *matrix*. But due to the interaction between the molecules and the host crystal lattice (of the matrix), the molecules inside the cryogenic matrix are of course not exactly equivalent to the free molecules. For instance, the rotational degree of freedom is hindered in the matrix (***quenching*** of rotational structure), as well as the vibrational frequencies being shifted with respect to the gas-phase frequencies.

Table 2-1 would suggest that the ideal matrix isolation material is helium due to its large intramolecular separation which minimizes the interaction between host molecules and the molecules trapped inside the matrix. But helium cannot be used as a material for matrix isolation spectroscopy since it solidifies only under a pressure of approximately 25 atm. Therefore, another technique has to be employed: ***helium***

nano-droplet spectroscopy, cf. e.g. [Nauta and Miller 2001; Toennies and Vilesov 2004; Merritt, Rudic et al. 2006; Rudic, Merritt et al. 2006].

A few years ago, solid-parahydrogen was reported as being used as a matrix medium for matrix isolation spectroscopy for the study of rotationally resolved IR-spectroscopy of CH_4 and CO molecules [Simon, Mario et al. 1999; Miki and Momose 2000; Tam and Fajardo 2000] and photochemical reactions. The matrix isolation spectroscopy employing para-hydrogen crystals as the matrix species offers some advantages as compared to inert gas matrices: There is no so-called "*cage effect"* in solid para-hydrogen, facilitating the performance of photolytic reactions in solid *p*-H_2 as compared to photolytic reactions in rare gas matrices. The existence of so-called "multitrapping sites" is a problem in inert gas matrix spectroscopy leading to broadening and splitting of absortption lines. This effect is caused by the different ways the molecules can be built into the matrix. This is not the case in the matrix *p*-H_2: In *p*-H_2 the lattice forces are sufficiently weak to allow the lattice to "adapt" to the built-in molecules.

3 Experimental setup and procedures

Cryogenic solids such as solid hydrogen are unique not only from the theoretical point of view but also for the experimentalist it is a challenge to find and ensure the optimal conditions for ortho/para conversion and crystal growth. The molecular solid H_2 as a so-called *quantum crystal* is characterized by its weak intermolecular forces. Solid hydrogen forms a perfectly transparent crystal only in the absence of impurities and mechanical stress.

In this chapter, the experimental design and procedures are described. The central component of the apparatus is an optical cryostat with a low temperature hydrogen cell (see **Figure 3-1**), in which the crystal is grown. The crystal growth can be observed through the optical windows of the cryostat and the hydrogen cell windows. Another crucial component for the successful operation of the Raman shifter is the ortho/para converter.

When I joined the research group of André Fielicke at the Fritz-Haber-Institute, the optical cryostat, the temperature controller and the vacuum pumps needed for the operation of the cryostat were already available. Some initial plans for the hydrogen Raman cell were already being worked out based on the design by Vilesov [Kuyanov, Momose et al. 2004]. The experimental part of the present diploma thesis (Diplomarbeit) consisted in the development of the converter system (including necessary adaptations of the cryostat), the hydrogen cell, the gas inlet and vacuum system, the ortho/para converter and the tube system that joins the different components of the system and the optical setup. The design of the components was created using SolidEgde ® (by UGS, Inc.), a 3D CAD software application for industrial product design. After the construction was completed, the optimization of the crystal growth was the major issue. The optimization resulted in a high gain factor of the SRS process, thus yielding a quantum efficiency of up to 0.59±0.02 (or 59±2%) for the backscattered first Stokes wave at intensities of approximately 20 mJ per pulse (averaged over 20 pulses) pump energy, and up to over 0.90±0.02 at energies below 1 mJ per pulse energies (averaged).

3.1 Experimental setup

The experiment is divided into two phases, the first of which is a ***test phase*** in which we pump the crystal using a frequency-doubled Nd:YAG laser (model Quanta-Ray, INDI-40-10, Spectra Physics, Inc.) at a wavelength of 532 nm yielding a first Stokes wavelength of 683 nm. In the second phase, we shall modify the optical elements to IR-optics and pump the crystal by a difference frequency mixing/optical parametric amplifier (DFM/OPA) system, which we tune from 1.5 – 2 μm in order to get an output of approx. 4 – 10 μm, cf. **Figure 3-10**.

Inside an optical cold finger cryostat (model SHI-4, Janis Research Company, Inc.), the Raman hydrogen cell (see **Figure 3-1**) - which is made of stainless steel and is equipped with two optical windows - is attached to the cold finger at the second stage of the closed cycle refrigerator system (cold head: model RDK-408D2 and helium compressor: model CSW-71D, Sumitomo Heavy Industries) via an oxygen-free high conductivity (OFHC) copper heat conductor that is brazed into the upper part of the cell.

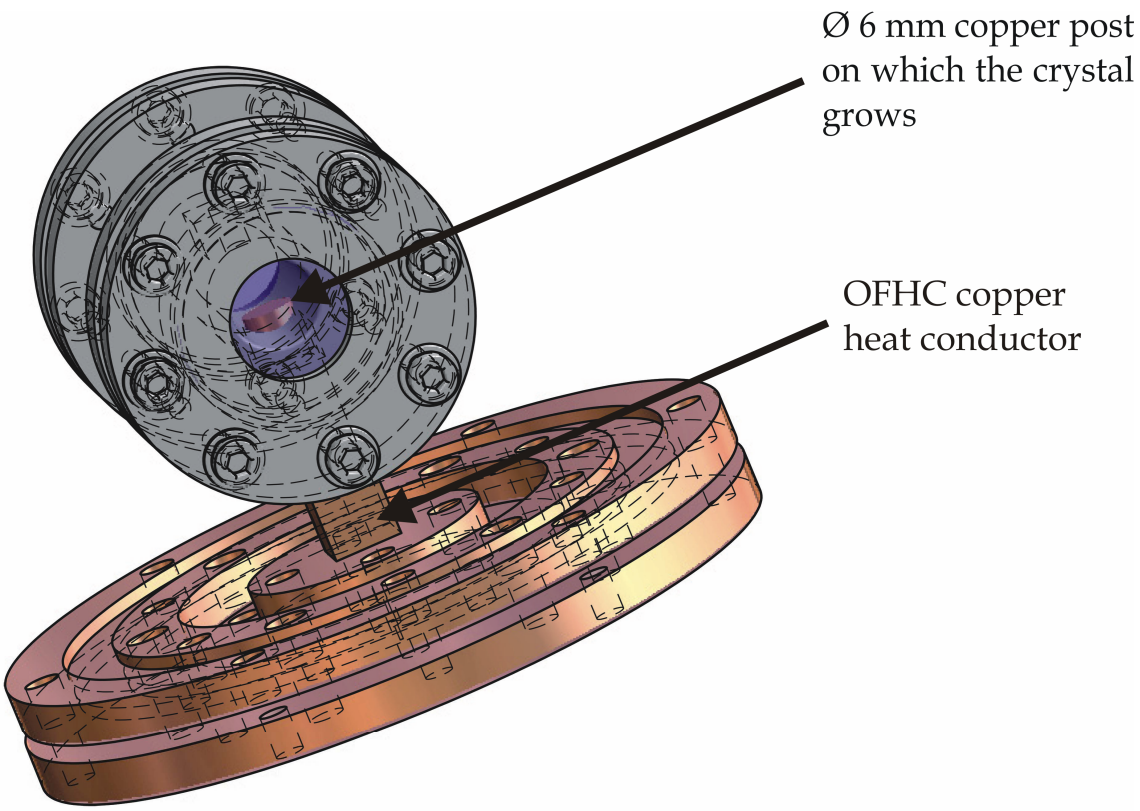

Figure 3-1: *Detail of the Raman cell (SolidEdge ® construction); view through optical window inside the cell (which is mounted upside down).*

The cell temperature can be varied in the range of approximately 4 K to 40 K by a 25 W by a resistive heater which is attached to the second stage of the refrigerator – see **Figure 3-5** – and controlled by loop 1 of the temperature controller (model TC-340, Lake Shore Cryotronics, Inc.). The temperature controller can drive two independent control loops (but only one is fully programmable) and read the temperatures of up to ten sensors, three of which are used at the moment. We use three identical silicon diodes (model DT-670 CU, Lake Shore Cryotronics, Inc.), two for measuring and controlling the temperatures at the cold finger (which is in good thermal contact with the copper post that is brazed into the upper part of the cell) and at the second stage of the ortho/para converter. The temperature of the second converter stage is varied by a 25 W cartridge heater (model HTR-25, Lake Shore Cryotronics, Inc.), cf. **Figure 3-5**. The third silicon diode sensor is used for measuring the temperature of the hydrogen cell.
The silicon diodes are activated by a constant current of 10 μA provided by the temperature controller in a four-wire configuration that compensates the effect of the potential drop across the wire lead connected to the diode. This configuration ensures that the 36 AWG phosphor bronze wire used (36 American wire gauge corresponds to a diameter of 0.127 mm) has a potential drop of less then three orders of magnitude smaller than the diode voltage. A problem arises only if the silicon diode sensors are used in a magnetic environment: Especially below liquid nitrogen temperatures, the sensor voltage changes significantly if the sensor is introduced into a magnetic field of say 1 Tesla, resulting in false temperature readings. Typical magnetic field-dependent temperature errors are $\Delta T / T = -10\%$ at 20 K but $\Delta T / T = -200\%$ at liquid helium temperature, both values are given for a field of 1 T *parallel to the sensor base* for the silicon diode temperature sensor we used in our experiment.[28]

The gas inlet system consists of a mass flow controller (model HFC-302, Teldyne Hastings Instruments) that allows for a maximum flow rate of 150 standard cubic centimeters per minute (sccm), three bellows-sealed valves, a safety high-pressure proportional relief valve and a tube system leading into the hydrogen cell inside the cryostat (see **Figure 3-3**). We use swagelok ® tube fittings and tube adapters for all the necessary connections inside the cryostat (except a few unavoidable hard-soldered or welded connections) and swagelok VCR ® metal gasket face seal fittings for the gas inlet system outside the cryostat. Before an experimental run, it is therefore important

[28] Cf. LakeShore Cryotronics Catalogue, 2004, p. 33.

to thoroughly leak-test the tube system and the hydrogen cell using a helium leak-tester (model QualyTest ™ HLT 270, Pfeiffer Vacuum, Inc.).

The average values we found for the leak rate of the gas system – including the hydrogen cell - was in the order of ≤ 5 x10^{-9} mbar l/s.[29] The optical windows of the hydrogen cell, which are indium gasket sealed, are a critical point as far as the leak-proofness is concerned. Therefore, special care had to be taken to assure that the indium wire used as a sealing agent was deformed to a thin annulus without voids between the cell body and the window (see **Figure 3-2**) forming a perfect sealant when carefully tightening the screws of the cell flange.

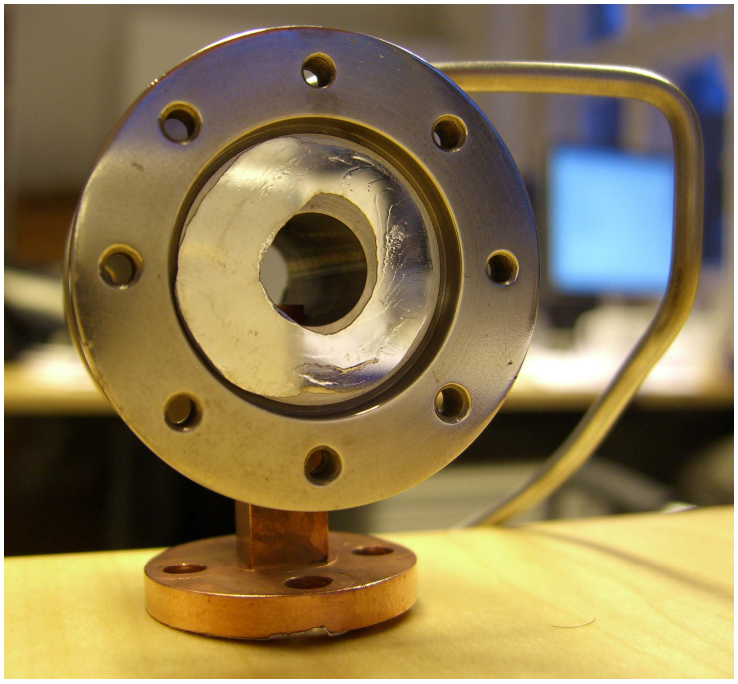

Figure 3-2: *Hydrogen Raman cell with brazed-in copper post. The annular indium gasket can be seen on the sealing face.*

Of course, the only hard test for leak-proofness under cryogenic conditions is an experimental cooling cycle, which we performed before actually growing the *para*-hydrogen crystals. The procedure for this test is very simple: We introduce hydrogen gas (at approx. 2 bar) into the tube system and the cell and start cooling down the system to approximately 4 K (which takes about an hour and a half) while constantly

[29] This value has little practical relevance, since in the experiment the system is first cooled down to approx. 14 K, where the leak rates can in principle be completely different due to the different thermal expansion coefficients of the different materials used. But since it is obviously not possible to leak-test the system mounted inside the cryostat, the measured leak rate nonetheless serves as a reference value. A somewhat more relevant test was also performed: Upon pressurizing the tube system with gaseous H_2 at approximately 30 bar, we used a so-called “sniffer” adapter to the leak-tester to check if the hydrogen gas, which is highly diffusive, escapes at some point of the system.

pumping the cryostat with the helium leak-tester (which has a small turbo pump and a pre-pump built in). If the initial leak rate of the “warm” system starts to increase while the temperature drops, we would have a serious problem. But in different experimental runs, we found that the system tends to get leak-tighter as the temperature drops to low temperatures, if the system is initially free of major leaks.

This behavior is easily explained if we look at the thermal expansion coefficients of the different materials involved at the cell windows: The cell-body and flanges as well as the screws are made of stainless steel which contracts to a much higher degree than the fused silica substrate of the optical cell windows: stainless steel of type 304 has a change in length of -0.306% when cooled down from room temperature to liquid helium temperatures, whereas fused silica has a thermal contraction of almost two orders of magnitude less (-0.0032%) [30], such that the contact pressure increases as the temperature drops. Of course this temperature dependence of the system leak-rate can only be seen if the leak-rates for the numerous other connections remain constant (or have the same temperature dependence).

In order to ensure this, the material properties of the materials used for the cryogenic environment have to be taken into account with respect to thermal expansion coefficients and thermal conductivity, so that for instance no excessive mechanical strain occurs at welding points and at soldering joints at low temperatures.

3.2 Crystal growth

Normal industrial grade hydrogen gas of very high purity (Westfalen, hydrogen 5.0, corresponding to 99.999% purity) is liquefied in the cryostat and converted into *para*-H_2 by passing it through two converter tubes (made of copper, 5 mm outer diameter) filled with globules of the catalyst (hydrous ferric oxide, mesh size 30x50, Sigma Aldrich). The ortho para conversion is achieved by a combination of two converters, approximately 40 cm and 20 cm long (see **Figure 3-4** and **Figure 3-5**), operating at temperatures of ~ 40 K and 14.5 K, respectively.

[30] Cf. e. g. R. P. Reed and A. F. Clark (Eds.): “Materials at Low Temperatures”, Amer. Soc. for Metals, Metals Park, OH, 1983, Chap. 3 and G. K. White: “Heat Transfer”, Oxford University Press, London, 1968, App. IX.

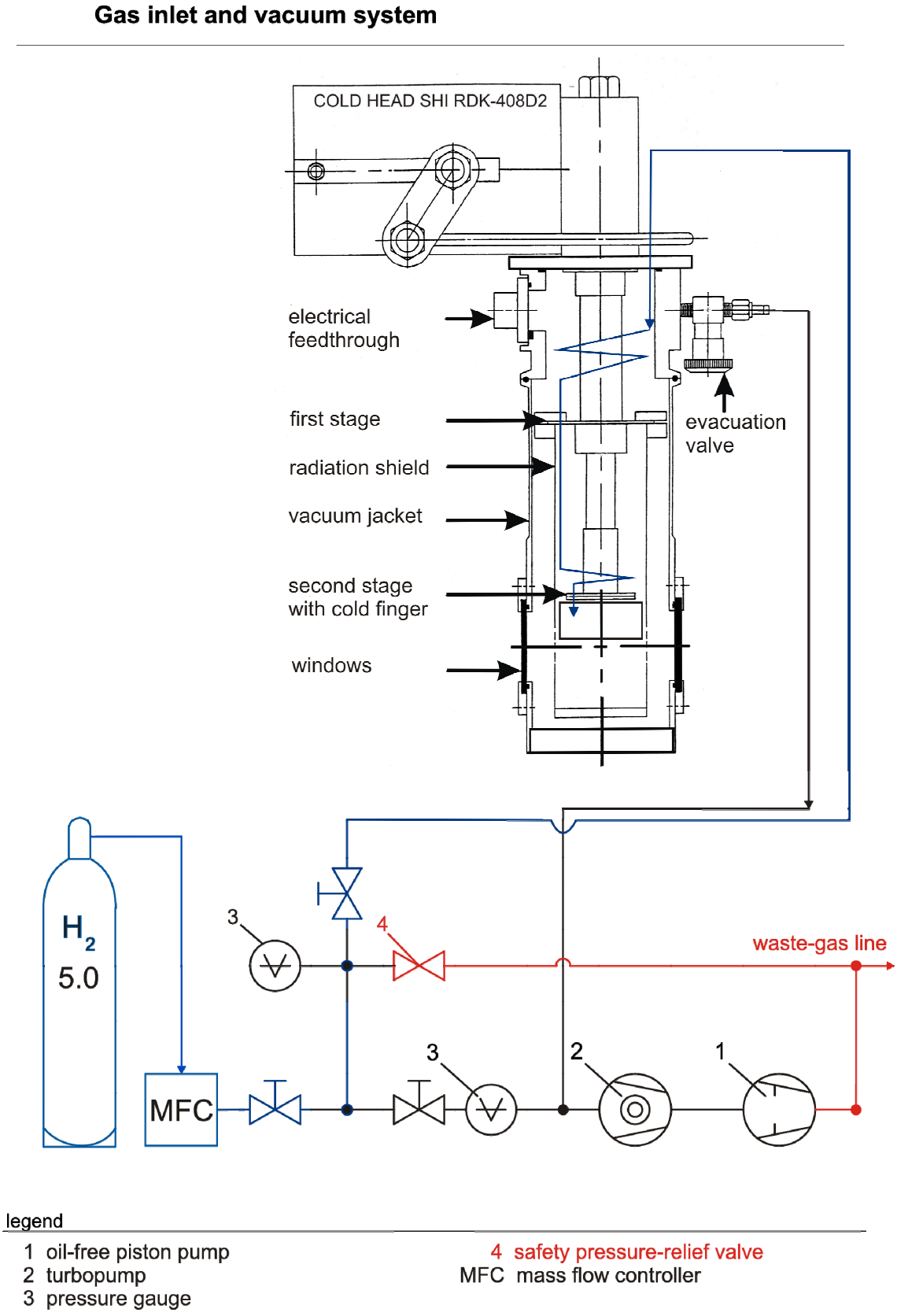

Figure 3-3: *Scheme of the gas inlet and vacuum system.*

A scheme of the setup inside the cryostat is shown in **Figure 3-4**, whereas **Figure 3-5** shows a photograph of the setup.

The two copper converter tubes are connected by a thin-walled stainless steel tube of 1/8'' outer diameter to minimize the heat load carried from the first refrigerator stage, where the temperature is approx. 40 K, to the second stage, which is at approx. 3 - 4 K. While the average thermal conductivity values for copper and stainless steel differ by a factor of over 30 in the temperature range from room temperature to liquid nitrogen temperatures, the situation is even more pronounced for lower temperatures (of 40K to 4 K of the first and second stages of our refrigerator, respectively), where the thermal conductivity of stainless steel is less then 1/500 of the value for copper[31].

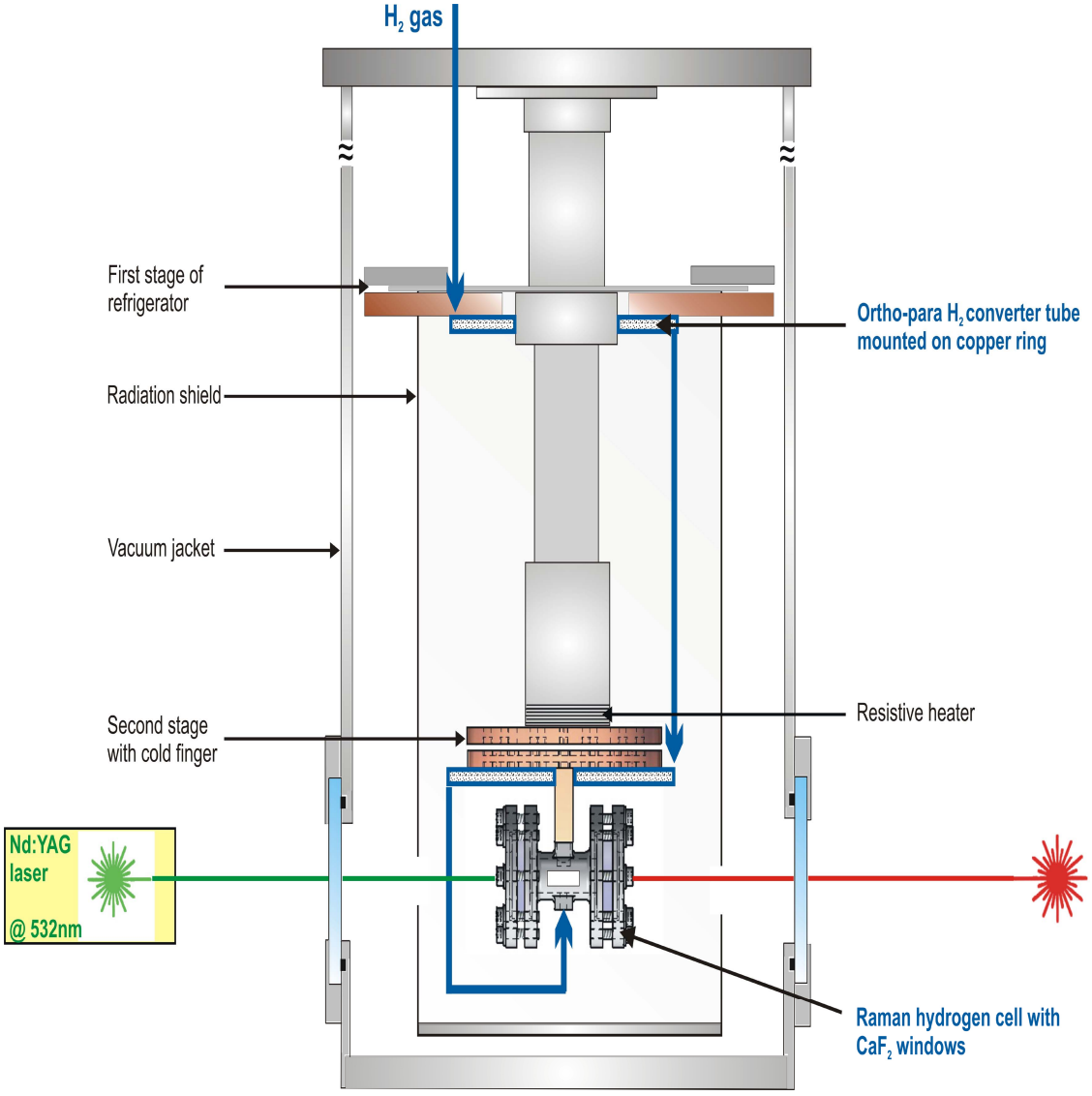

Figure 3-4: *Scheme of the experimental design inside the optical cryostat.*

[31] Ibid, Chap. VII.

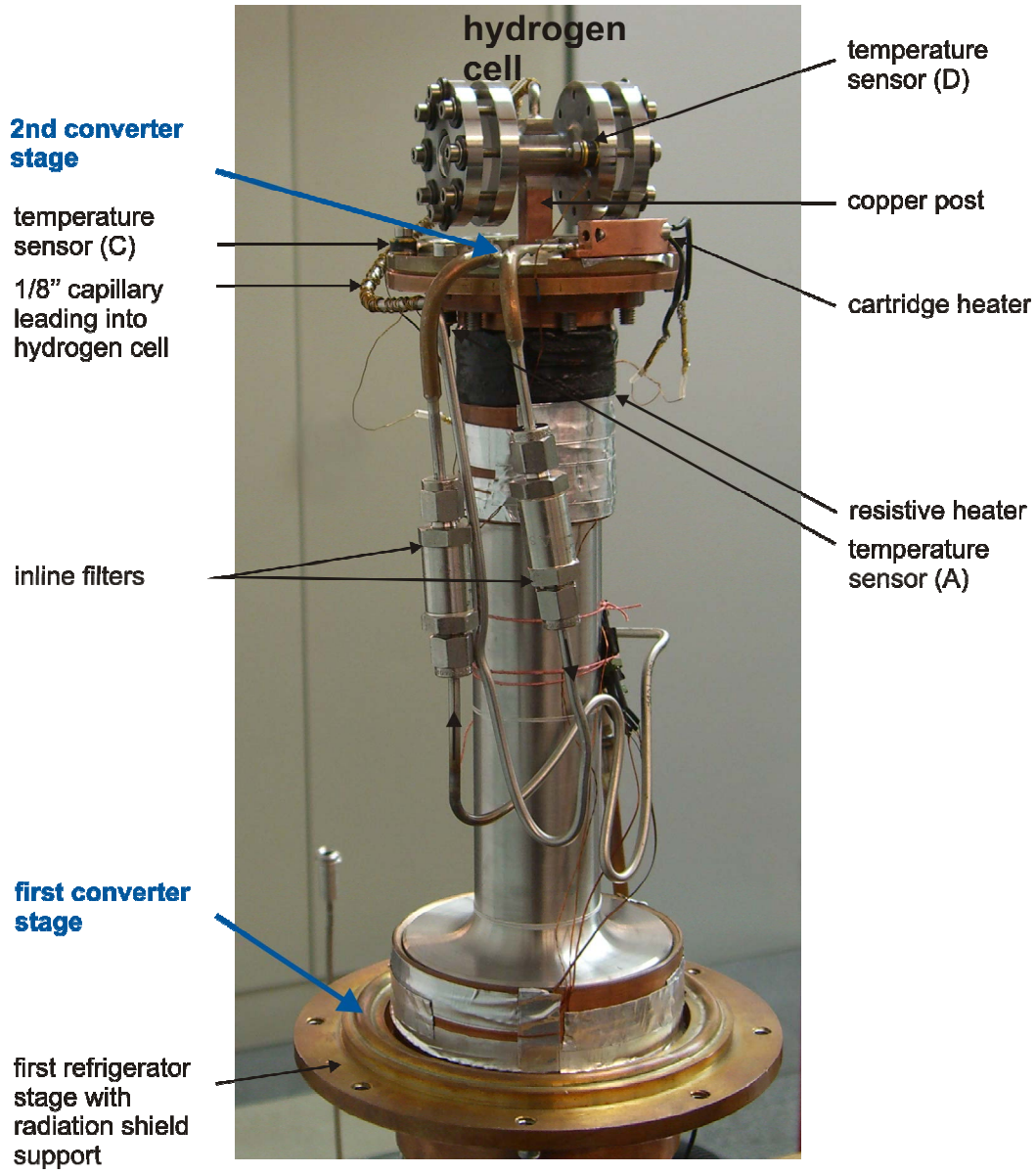

Figure 3-5: *Cryostat with ortho-para converter and 30 mm hydrogen Raman cell (mounted up-side down).*

Before introducing the hydrogen gas, it is important to evacuate the tube system and hydrogen cell to a residual pressure of less than approx. 10^{-5} mbar (measured with a pressure gauge which is quite far from the relevant tube system, so that the pressure in the 1/8''-tube system and hydrogen cell is still somewhat higher, cf. **Figure 3-3**) in order to remove all possible impurities such as air and water vapor, etc. Then the compressor of our cryostat is turned on, and starts cooling the cold finger - temperature (A) in the above figure - to about 3 K in approximately two hours. The hydrogen gas is introduced with an initial flow rate of 75 sccm into the cell until the whole cell is filled with liquid *p*-H_2. With a 70 mm long cell this takes about 45 min. The cell temperature is approximately 17 K – measured with sensor (D) in **Figure 3-5** – at this time, while the

temperature of the second converter stage at (C) is set at approximately 14.1 K (set-point for loop 2 of the temperature controller), which is only slightly above the triple point of *p*-H_2. The temperature at the cold finger (A) is controlled by loop 1 of the temperature controller and set at approximately 12.5 K while filling the cell. We could select a higher value for the cold finger temperature (A), but because the temperatures at (C) and (A) are not completely decoupled, this would lead to a slight increase of the temperature at the second converter stage (C), which is not favorable since this shifts the temperature-dependent ortho-para ratio towards the ortho species of molecular hydrogen, cf. **Figure 2-4**.

After the cell is completely filled with liquid *p*-H_2, the flow rate is increased to the maximum value which the flow controller permits (150 sccm), such that a pressure of ~ 30 bar builds up in about 40 minutes. The temperature is lowered at a rate of approx. 0.1 K/hr. at the cold finger (A) which is in very good thermal contact with the copper post brazed into the upper part of the cell, so that the *p*-H_2 crystal starts growing from the 6 mm diameter copper post downwards until the entire cell is filled with a perfectly transparent crystal (see **Figure 3-6**). The lowering of the temperature at the cold finger – point (A) in **Figure 3-5** – is achieved by programming loop 1 of the temperature controller. At this point, the temperature of the second converter stage (C) is kept at approximately 15 K, so that the hydrogen does not solidify in the second converter stage or in the stainless steel capillary brazed into the bottom of the cell. This is extremely important since otherwise the crystal growing pressure of approx. 30 bar could not be maintained. We found that in this case, the crystals usually cracked at a cell temperature of about 8 K (when the pressure in the growing phase was not at least approx. 20 bar).
When the temperature is lowered at point (A), the cell temperature (D) also drops even if the second converter stage – point (C) – is at temperatures of 1 - 2 K above the triple point of *p*-H_2. When the cell temperature (D) reaches approximately 12-13 K, almost the entire cell is filled by a *p*-H_2 crystal. We found that it is necessary to heat the capillary brazed into the bottom of the cell by a small heating current of approx. 50 mA corresponding to a heating power of approx. 110 mW (in **Figure 3-5** one can see a manganine wire of 0.2 mm diameter, approximately 2 m long with a resistance of ~ 45 Ω twisted along the stainless steel capillary), to ensure that the hydrogen does not solidify in the capillary.
When the crystal fills the entire cell and is perfectly transparent, the temperature of the second converter stage (C) is slowly ramped down to 3 K (at a rate of approx. 0.2 K/min by turning on the “ramp” function on control loop 2 of the temperature controller), and the temperature of the copper post is lowered by ramping the temperature of the

first control loop (A) down to 2.5 K. As the control loops are independent, the ramp for the first control loop can be set at a different value of approx 0.1 K/min. The cell temperature consequently drops to approximately 4 K within about one hour and 40 min[32], so that a pump beam focused into the crystal by a (f = +60 mm) lens can now precipitate the process of SRS.

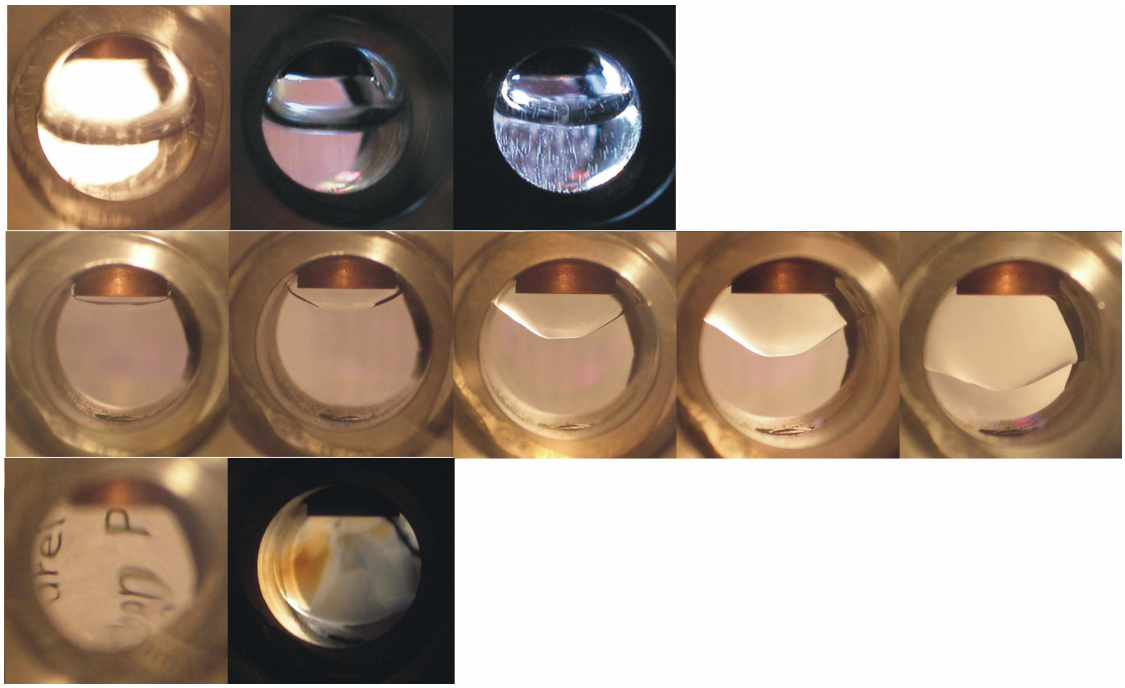

Figure 3-6: Hydrogen condensation and crystal growth. *The first three pictures show the condensation into liquid p-H_2 at the bottom of the cell. In the next five pictures, the crystal growth from the copper post downwards can be seen very clearly, producing a perfectly transparent crystal. The last two pictures show a picture of the view through the crystal: One can read the letters through the crystal. The last picture was taken using crossed polarizers revealing some mechanical stress on the crystal causing the colors seen in the image due to non-ideal growth parameters: The crystal was grown at a pressure of less than 10 bar. No grain boundaries were observed.* [33]

The entire setup is shown in **Figure 3-7**.

[32] A “recipe” for crystal growing with all relevant growing parameters and procedures is given in Appendix B 7.1.

[33] Cf. [Chan, Lee et al. 1991; Chan, Okumura et al. 1991b; Chan, Okumura et al. 1991a].

Figure 3-7: *The entire setup with vacuum system on the right, gas inlet system, and temperature controller.*

3.3 Optical setup

3.3.1 Test phase experiment (crystal pumped by Nd:YAG laser at λ=532 nm)

In the first phase of the experiment, we pump the crystal using the output of a frequency-doubled Nd:YAG laser at a wavelength of 532 nm. The beam is focused into the hydrogen cell using a planoconvex lens (f = +60 mm). A combination of a λ/2-waveplate and a BK-7 cube polarizer is used to attenuate the incident laser beam. The backscattered first Stokes wave is coupled out by means of a dichroic mirror (DM) and its energy measured using laser power sensors (mod. J25LP-MB and J8LP, Coherent, Inc.) and power meters (mod. Energy Max 500, Molectron Detector, Inc). The setup is shown in **Figure 3-8**.

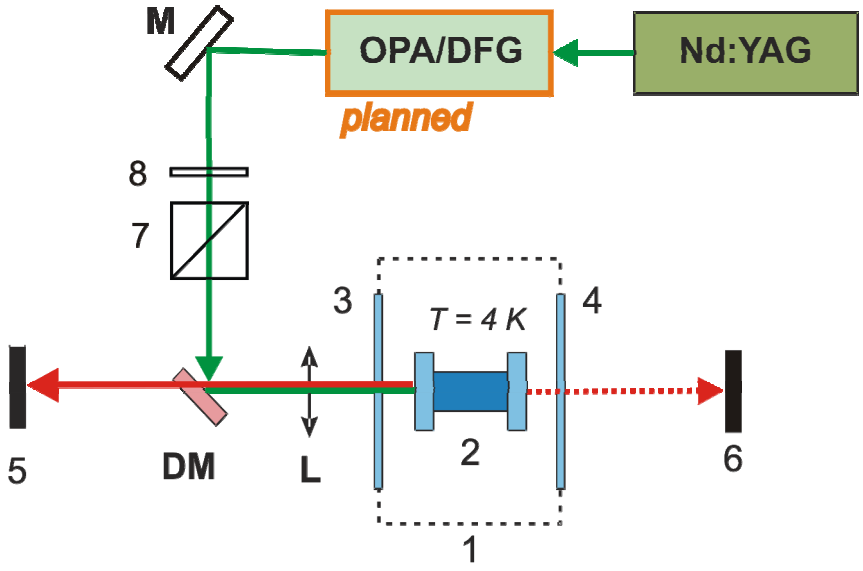

Figure 3-8: Optical setup: *The dichroic mirror (DM) is HR at 532 nm and HT at 683 and 436 nm, the frequencies of the first Stokes and anti-Stokes waves, respectively.*

Figure 3-9 shows a picture of the optical setup with the Nd:YAG pump laser.

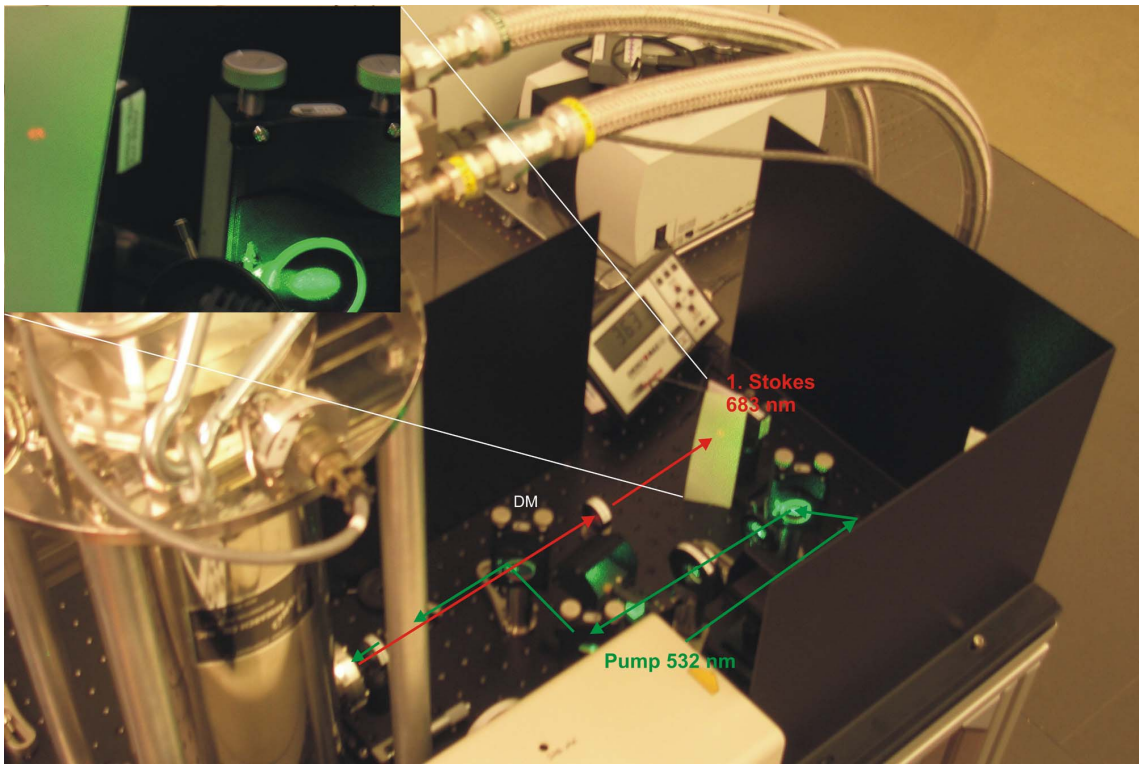

Figure 3-9: *Photography of the optical setup. One can see the Stokes wave beam on the detection screen.*

3.3.2 Near-IR pump laser system

In order to obtain m-IR radiation, the crystal will be pumped by a difference frequency mixing/optical parametric (DFM/OPA) amplifier laser system shown in Figure 3-10.

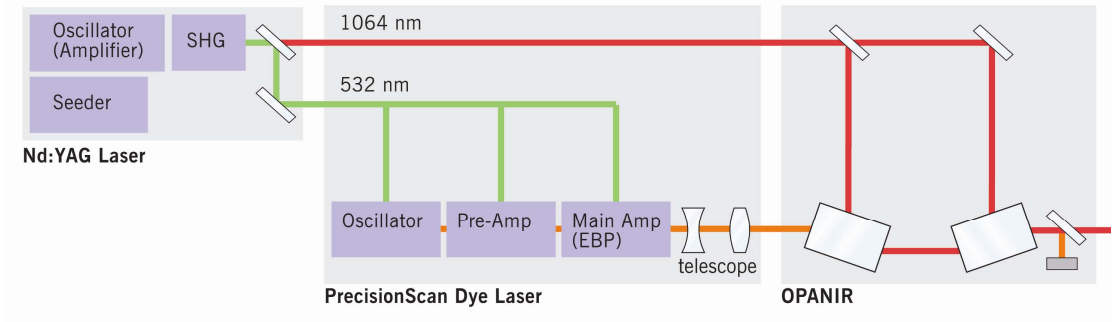

Figure 3-10: *Near-infrared pump laser system © by Sirah.*

A type 2 potassium di-deuterium phosphate (KD*P) crystal is used for the second harmonic generation (SHG) of an injection seeded Nd:YAG laser, the output of which is used to pump a dye laser. In a $LiNbO_3$ crystal, the difference frequency mixing of the

dye laser output and the fundamental of the Nd:YAG is achieved, yielding an output frequency that can be tuned between 1.5 and 2 μm in order to pump the hydrogen crystal of the Raman shifter.

4 SRS in solid *para*-H_2: results and discussion

As mentioned in the preceding sections, the experiment is divided into two phases. In the first phase the *p*-H_2 crystal is pumped by a frequency-doubled Nd:YAG laser at a wavelength of 532 nm. This phase was intended as a *test phase*, in which the crystal growth was optimized in order to produce crystals of high optical quality and with high SRS gain factors.
In the second phase, the Raman shifter shall be pumped by a DFM/OPA system, which can be tuned from 1.5 to 2 μm in order to produce m-IR radiation from approximately 3-10 μm.

4.1 Test-phase experiment with Nd:YAG second harmonic at λ=532 nm

We conducted SRS experiments with different condensed phases of para-hydrogen, i.e., we studied SRS in liquid *p*-H_2 as well as in solid *p*-H_2. Crystal growth was performed with a set of different growth methods and parameters (growing pressure, crystal growth rate, conversion temperature, conversion flow rate). Though growth from the gas phase has been reported [Weliky, Byers et al. 1994], the results were quite disappointing producing crystals with central voids that were not perfectly transparent, and usually cracked when cooled to temperatures below approximately 9 K.
The best results were achieved with the method of growth under a pressure of approximately 30 bar, as reported by Suzuki et al. and Kuyanov, Momose and Vilesov [Suzuki, Katsuragawa et al. 1998], [Kuyanov, Momose et al. 2004].

4.1.1 SRS in *liquid p*-H_2

The first successful operation of the Raman shifter was achieved in the *liquid phase* at a cell temperature of approximately 17 K and a pressure of approximately 20 bar. The output of the backscattered first Stokes wave as a function of the per pulse pump energy (both averaged over 20 pulses) revealing a very high conversion efficiency for the liquid phase is shown in Figure 4-1.

It is interesting to note that the liquid phase has not been the subject of many studies since Stoicheff [Stoicheff 1965], but a recent study by McCall, Fushitani, Lindsay, Saykally, Momose and Oka [McCall, Fushitani et al. 2003] revealed much lower absolute conversion efficiency (of roughly 0.075 or 7.5% at pump energies below approximately 20-30 mJ) than the Raman shifter used in our study, which achieved 0.20±0.04 or (20±4) % conversion efficiency corresponding to a quantum yield of 0.32±0.05.

The quantum yield is computed by using the following relation between the averaged per pulse energies of the pump and backscattered first Stokes beams [Kuyanov, Momose et al. 2004]:

$$\eta = \frac{\bar{E}_{1.S}}{\bar{E}_P} \frac{\lambda_{1.S}}{\lambda_P} \gamma \tag{4.1}$$

where γ is a factor taking into account losses from the reflection of four surfaces (a focusing lens, the cell windows) and a red filter, that is highly transmissive (HT) for the wavelength of λ=683 nm, which corresponds to the wavelength of the first Stokes wave. We measured a value of 1.60±0.05 for the factor γ.

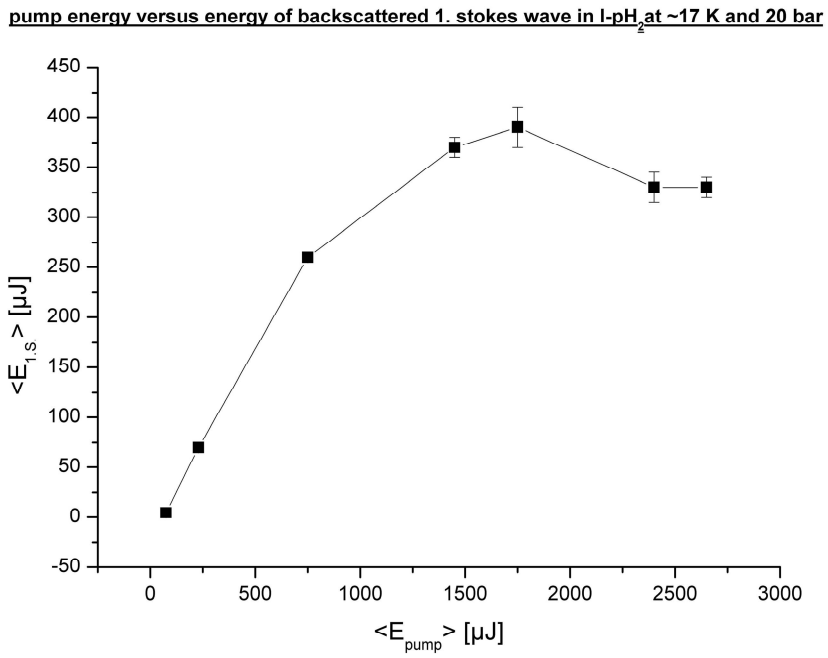

Figure 4-1: Conversion efficiency for liquid p-H_2 at T=17 K and p=20 bar.

4.1.2 SRS in *solid p*-H_2

The first experiments in the solid phase were carried out at approximately 12 K cell temperature and revealed high quantum yields of 0.68±0.04 but only for low energies up to 0.3 mJ (per pulse energy, averaged), see Figure 4-2. At higher energies, the quantum yield dropped to only 0.05±0.01.

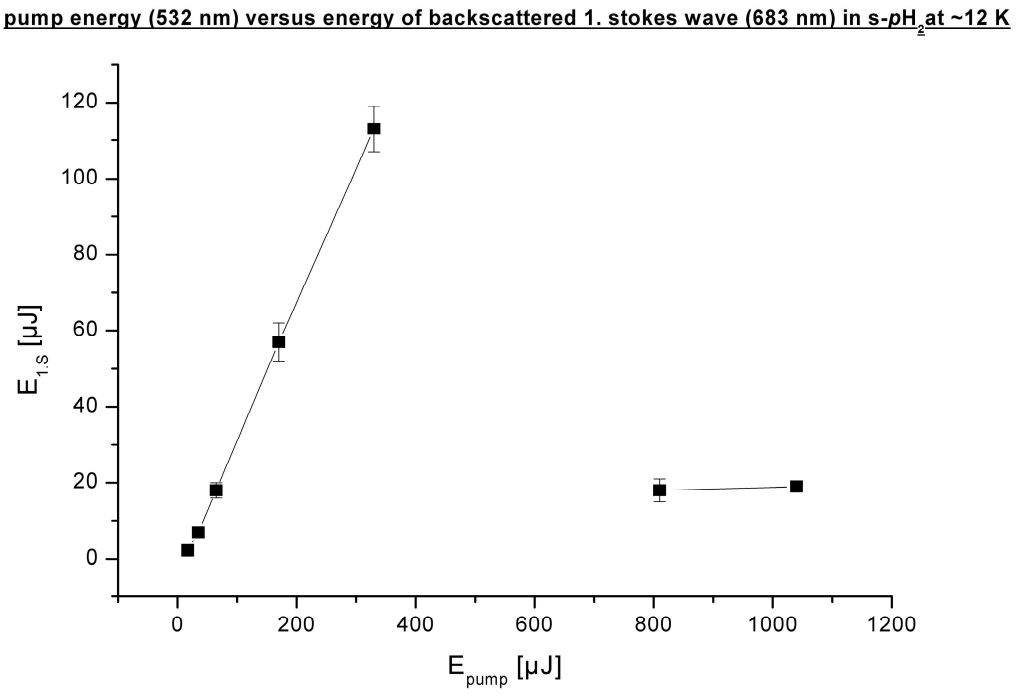

Figure 4-2: First results of SRS in solid p-H_2.

The first crystals could not be cooled to temperatures below approximately 9 K without cracking, which obviously makes the crystal useless for optical experiments. The experimental problem was that the hydrogen froze in the thin stainless steel capillary brazed into the bottom part of the cell when the cell temperature (D) fell below the triple point temperature, such that the pressure in the growth phase was not maintained. We tried to solve this by increasing the second stage converter temperature (C) to approximately 20 K but still the crystals kept cracking under the cooling process. We also tried to grow the crystals at higher pressures revealing no improvement.

To overcome this problem, a manganine wire heater of 0.2 mm was twisted around the stainless steel capillary to prevent the hydrogen from freezing in the growth phase. The

heater current we used was approximately I_h= 50 mA corresponding to a heater power of P_h≈ 50 mW.

This finally allowed us to produce crystals of high optical quality that can be cooled to any desired temperature; the lowest achievable cell temperature (D) is ≈ 4 K with our closed-cycle refrigerator. **Figure 4-3** shows the output energy of the first Stokes wave as a function of the pump energy, both averaged over 20 pulses, indicating a quantum yield of 0.42±0.04.

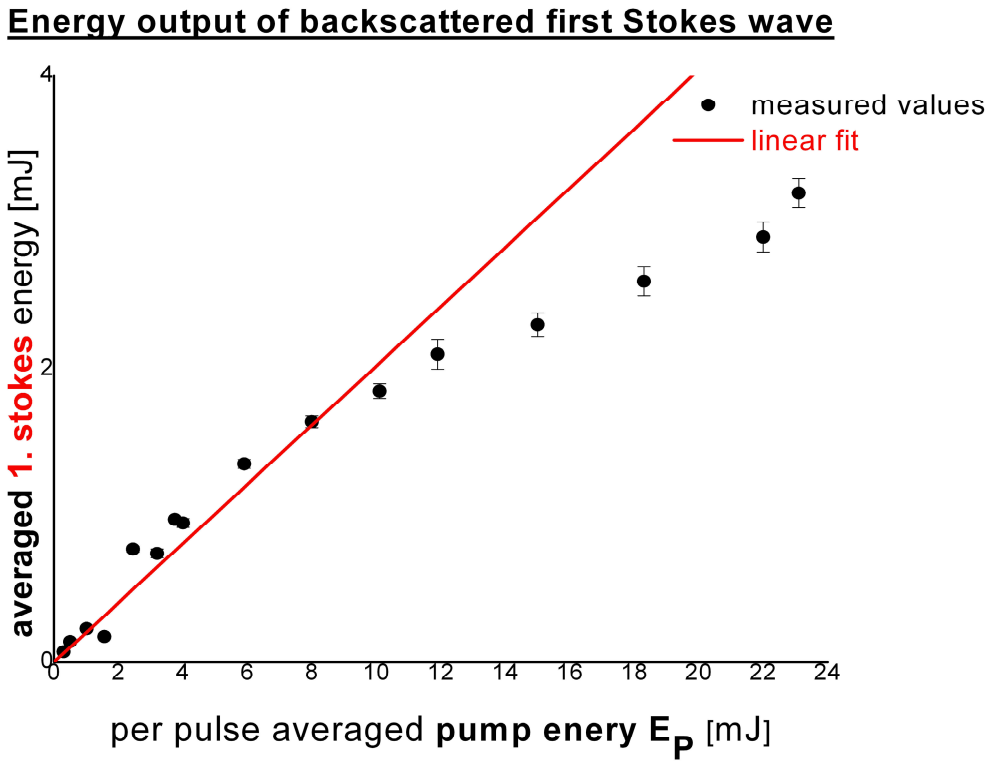

Figure 4-3: *Per-pulse averaged energy of the backscattered first Stokes wave as a function of pump energy. 30 mm Raman hydrogen cell, crystal temperature ≈ 4 K.*

Another problem was related to laser power absorption from small “dirt” particles, which typically showed up at cell temperatures around 13 – 14 K at the inner surfaces of the cell windows since these are not built into the crystal lattice but rather freeze out at the cell windows. At this instant of the experiment, the cell windows are the warmest spots, so it appears plausible that the “dirt” particles sediment there. At first we thought that these particles were small fractions of the catalyst, which is filled inside the copper tubes on the first and second converter stages, operating at temperatures of approximately 40 K and 14 K, respectively. The manufacturer specifies the catalyst particle size with a so-called mesh size of 30x50, which corresponds to a mean particle size of

300 – 600 microns. We believed that these small particles were fragments of the catalyst that were carried through the stainless steel sinter filter elements (of 5 microns nominal pore size) at the end of each converter stage. Therefore, we replaced these filter elements by swagelok inline filters (with exchangeable filter elements), and used the finest nominal pore size filter elements (of 0.5 microns nominal pore size). We also tried to chemically detect traces of copper oxides that could have been produced on the inner copper tube surfaces from the hard-soldering processes. But the test reaction produced a negative result.

We found that it was probable that some of the particles originate from the fluxing agent and hard solder used in the brazing processes (brazing of the copper post and the stainless steel capillary into the hydrogen cell), while other particles seem to get washed though the filters. After replacing the primarily used filters, we could see a significant improvement. But we also did see an improvement with each experimental run after the cell and cell windows were thoroughly cleaned, which indicates that the particles from the inner cell surface are washed out increasingly with each experimental cycle. After approximately 30 or more experimental cycles, we came to the conclusion that most likely we have to deal with *both* types of particles. The strongest indication favoring this explanation originates from the different patterns produced by the different types of particles: While the particles from the soldering processes display a *diffuse*, smeared-out pattern, the fractions of the catalyst display a *regular*, crescent pattern below the cell axis.

These particles also explain the drop in the Stokes wave intensities, which were probably due to absorption caused by the particles: Upon examining the cell windows, we could clearly see dark spots of burnt-in particles on the inner surface of the front cell window in experimental runs that initially produced results indicating high quantum yields, while there was a sudden drop-down at certain intensities.

We used two different second converter stages (approximately 15 and 25 cm long, respectively), and also two different cells. One cell was 30 mm long, while the other was 68.5 mm long. The reason we built the longer cell was that we wanted to find out if an increased interaction length would improve the SRS gain, but the longer cell is also favorable for our focusing geometry: The pump laser beam is focused using a lens with short focal length of f= +60 mm, so that it is possible to use higher laser powers up to 100 mJ per pulse energy with the longer cell, since the beam diverges at the cell windows, while the focal point is approximately in the cell centre. The longer cell is built asymmetrically making use of the fact that the scattering intensity with respect to forward and backward direction is different, such that the intensity of the forward scattered laser beam is much lower and less focused than in the backward direction, and at the

same time the pump pulse is significantly depleted while traveling through the cell. Thus, the posterior part of the cell body (seen from the direction of the incident beam) can be built shorter than the front part of the cell body.

After the optimization of the crystal growth, the best conversion efficiencies to date were achieved using the 30 mm long cell. The results are shown in **Figure 4-4**.

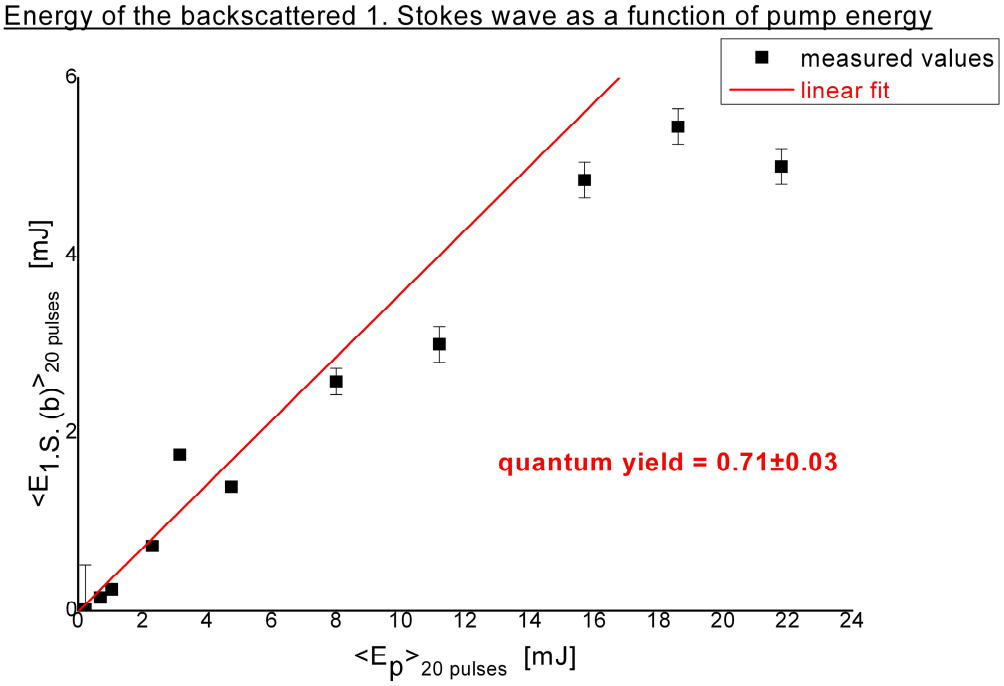

Figure 4-4: *30 mm cell conversion efficiency at T= 4 K cell temperature.*

As a comparison, the best results to date using the long cell are shown in Figure 4-5.

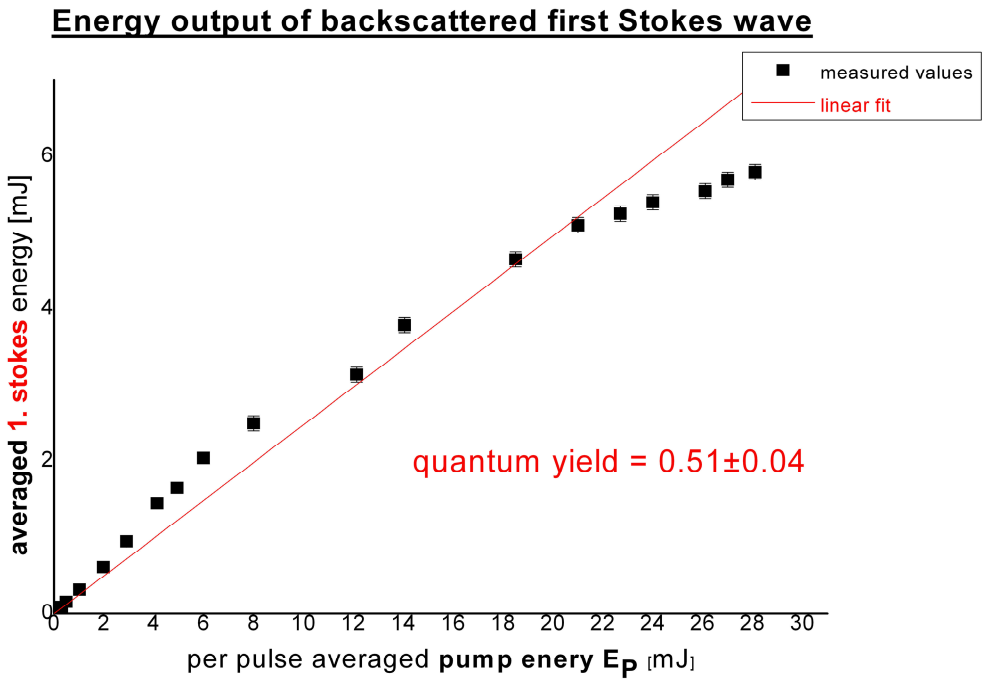

Figure 4-5: Conversion efficiency for the 68.5 mm hydrogen cell.

We did not study the purity of the para-hydrogen crystals, in order to determine the remaining fraction of ortho-hydrogen molecules in the crystal. But according to Kuyanov, Momose and Vilesov [Kuyanov, Momose et al. 2004], the residual fraction of ortho-hydrogen is approximately $2 \cdot 10^{-4}$ at the temperature of their second converter stage, which is 16 K. This value is in agreement with the value found in Souers [Souers 1986, p. 26.]. Since the conversion temperature we used was approximately 14.1 K, the residual ortho fraction is estimated to be even smaller: According to Souers [Souers 1986, p. 26.], it is **$4.6 \cdot 10^{-5}$ at 14 K.** Together with the fact that the second converter stage we used for all the experiments mentioned in the present work is approximately 25 cm long (i.e., five times longer than the one used by Kuyanov, Momose and Vilseov), this explains the higher SRS gains (and thus higher quantum yields) in our experiments.

As a comparison to the results presented in the present work, Kuyanov, Momose and Vilesov reported a quantum yield of approximately **0.32 ± 0.05** for the backscattered first Stokes wave, from Fig. 2 in [Kuyanov, Momose et al. 2004].

The ***threshold pump energy*** for the generation of the backward scattered Stokes beam was 5 ± 1 μJ (corresponding to a pump power density of approximately 10 ± 2 MW/cm^2) for the 30 mm cell and approximately 85 ± 5 μJ for the 68.5 mm cell. The first value is slightly lower than the value reported in the work of Vilesov's group (12 ± 4 μJ).

We found that the backward scattered Stokes beam has good optical quality with a beam divergence and polarization almost equal to the pump laser: The beam divergence measurement yielded 2 ± 1 mrad and the polarization was 96 ± 3 % vertically polarized output radiation (pump laser beam divergence < 1.5 mrad, >99% vertical polarization).

4.2 Near-IR pump laser

Unfortunately the near-infrared pump laser is not available to date, such that the measurements of SRS gain factors for the Stokes-shifted radiation in the IR could not been investigated.

5 Conclusions and outlook

It has been shown that solid *p*-H_2 is an outstanding medium for SRS-based Raman shifters.

It is planned to automate the process of crystal growth using LabView ® (National Instruments Corp.) to control the temperature and pressure values using a PC in order to ensure optimal conditions for the crystal growth while the operation of the Raman shifter is significantly simplified for the user.

As a first application, it is planned to use the m-IR output of the Raman shifter to study bio-molecules in the gas phase (e.g. the *hemin* molecule, $C_{34}H_{32}FeN_4O_4$•Cl, and CO-stretch in CO-hemin complexes) in the group of Gert van Helden at the Fritz-Haber-Institut der Max-Planck-Gesellschaft. Also *peptides* can be studied using the Raman shifter, since the *amide I* and *amide II modes* of peptides lie in the wavebands 1600 cm^{-1} – 1700 cm^{-1} and 1500 cm^{-1} – 1600 cm^{-1}, respectively. In general, the Raman shifter output can be used to study a great number of bio-molecules in the gas-phase, e. g. conformational analysis of amino acids etc.

A further application is planned for the study of transition metal oxide and transition metal carbonyl clusters using the Raman shifter m-IR output radiation in the group of André Fielicke.

6 Appendix A: Mathematical supplements

A1: The mathematical treatment of spin[34]

A1.1: General properties

The spin is an intrinsic property of particles. The mathematical space to describe a particle with spin is the tensor product of the Hilbert space $\mathcal{H}_r$, the orbital state space, in which the observables of space **R** and momentum **P** operate, and the spin space $\mathcal{H}_s$. This means that we have to add spin variables to the fundamental observables **R** and **P**, whose spin operator **S** has to conform to the following postulates:

(S1) **S** is an *angular momentum*, i.e., its components have to obey the commutation relations:

$$\left[S_x, S_y\right] = i\hbar S_z \text{, and cyclic permutations hereof.} \tag{6.1}$$

(S2) **S** is operating in a new space, the spin space, in which $\mathbf{S}^2$ and S_z are constituting a complete set of commuting operators (C.S.C.O.). This means the following: The space is spanned by the set of mutual eigenstates $|s,m\rangle$ of S^2 and S_z:

$$\mathbf{S}^2 |s,m\rangle = s(s+1)\hbar^2 |s,m\rangle \tag{6.2}$$

$$S_z |s,m\rangle = m\hbar |s,m\rangle, \tag{6.3}$$

where s is either integer or half-integer and m = -s,….,+s. Thus the Hilbert space $\mathcal{H}_s$ has the dimension (2s+1).

(**S3)** The state space $\mathcal{H}$ is the tensor product of $\mathcal{H}_r$ and $\mathcal{H}_s$:

$$\mathcal{H} = \mathcal{H}_r \otimes \mathcal{H}_s \tag{6.4}$$

Thus all spin observables commute with the orbital observables, i.e., a complete characterization of a particle state is a linear combination of tensor products formed by a ket vector from $\mathcal{H}_r$ and a ket from $\mathcal{H}_s$.

(S4) The electron is a spin-½ particle, thus the dimension of its spin space is

$$\dim \mathcal{H}_s = (2s+1) = 2,$$

since in this case s = ½ .

Properties of spin ½'s

As mentioned above $\dim \mathcal{H}_s = 2$. As a basis, we select the ONS $\{|+\rangle, |-\rangle\}$, which consists of eigenvectors of $\mathbf{S}^2$ and S_z:

$$\mathbf{S}^2 |\pm\rangle = \tfrac{3}{4}\hbar^2 |\pm\rangle \tag{6.5}$$

$$\mathbf{S}^2 |\pm\rangle = \tfrac{3}{4}\hbar^2 |\pm\rangle \tag{6.6}$$

$$\langle +|-\rangle = \langle -|+\rangle = 0 \text{ and } \langle +|+\rangle = \langle -|-\rangle = 1 \tag{6.7}$$

$$|+\rangle\langle +| + |-\rangle\langle -| = 1 \tag{6.8}$$

Thus the most general spin state can be represented by the vector $|\chi\rangle \in \mathcal{H}_s$:

$$|\chi\rangle = c_+ |+\rangle + c_- |-\rangle \tag{6.9}$$

where $c_+, c_- \in \mathbb{C}$ and $|c_+|^2 + |c_-|^2 = 1$. In analogy to the case of angular momentum operators, we can define the operators $S_\pm = S_x + iS_y$, which act in the following manner on the basis vectors:

$$S_+ |+\rangle = 0\,,\; S_+ |-\rangle = \hbar|+\rangle\,,\; S_+ |+\rangle = 0\,,\; S_- |+\rangle = \hbar|-\rangle \text{ and } S_- |-\rangle = 0 \tag{6.10}$$

---

[34] A very comprehensive elementary treatment can be found in [Cohen-Tannoudji, Diu et al. 1999], which also served as a basis for the description in this Appendix.

A1.2: Addition of two spins ½'s

Let us consider a system consisting of two spin-1/2 particles whose spin operators are $\mathbf{S_1}$ and $\mathbf{S_2}$, respectively. The state space of such a system is the tensor product of the spin states of the two particles, resulting in a four-dimensional space. An orthonormal basis (O.N.B.) of this space is the following basis, which we denote by $\left\{ \left|\varepsilon_1\right\rangle, \left|\varepsilon_2\right\rangle \right\}$:

$$\left\{ \left|\varepsilon_1\right\rangle, \left|\varepsilon_2\right\rangle \right\} = \left\{ \left|+,+\right\rangle, \left|+,-\right\rangle, \left|-,+\right\rangle, \left|-,-\right\rangle \right\}. \tag{6.11}$$

We know that these vectors spanning the four-dimensional tensor product space are eigenstates of the extensions of the fours observables $\mathbf{S}_1^2$,$\mathbf{S}_2^2$, S_{1z} and S_{2z} into that tensor product space, i.e., we define for example the extension of the operator $\mathbf{S}_1^2$, which is only defined in the first spin state, as $\mathbf{S}_{1(\text{ext})}^2 := \mathbf{S}_1^2 \otimes \mathbb{1}$, and $\mathbf{S}_{2(\text{ext})}^2 := \mathbb{1} \otimes \mathbf{S}_2^2$, respectively.

$$S_i^2 \left|\varepsilon_1, \varepsilon_2\right\rangle = \frac{3}{4}\hbar^2 \left|\varepsilon_1, \varepsilon_2\right\rangle, i = 1,2, \tag{6.12}$$

$$S_{iz} \left|\varepsilon_1, \varepsilon_2\right\rangle = \frac{\hbar}{2}\varepsilon_i \left|\varepsilon_1, \varepsilon_2\right\rangle, i = 1,2. \tag{6.13}$$

(The extensions of) the observables $\mathbf{S}_1^2$, $\mathbf{S}_2^2$, S_{1z} and S_{2z} (into the tensor product space) form a C.S.C.O.

The *total spin* **S** of the system defined as

$$\mathbf{S} = \mathbf{S}_1 + \mathbf{S}_2 \tag{6.14}$$

is an angular momentum operator as well, since both $\mathbf{S}_1$ and $\mathbf{S}_2$ are angular momentum operators, which can easily be verified by computing e.g. the commutator of S_x and S_y:

$$\begin{aligned} \left[S_x, S_y\right] &= \left[S_{1x} + S_{2x}, S_{1y} + S_{2y}\right] = \left[S_{1x}, S_{1y}\right] + \left[S_{2x}, S_{2y}\right] \\ &= i\hbar S_{1z} + i\hbar S_{2z} = i\hbar S_z, \text{ cyclically.} \end{aligned} \tag{6.15}$$

The operator $\mathbf{S}^2$ is the scalar square of **S**,

$$\mathbf{S^2} = \mathbf{S_1}^2 + \mathbf{S_2}^2 + 2\,\mathbf{S_1} \bullet \mathbf{S_2} \tag{6.16}$$

where

$$\mathbf{S_1 \cdot S_2} = S_{1x}S_{1x} + S_{1y}S_{1y} + S_{1z}S_{1z} = \frac{1}{2}(S_{1+}S_{2-} + S_{1-}S_{2+}) + S_{1z}S_{2z} \tag{6.17}$$

We can now find a **new** basis of eigenvectors (in the tensor product space) consisting of the new set of commuting observables $\left\{\mathbf{S}_1^{\,2}, \mathbf{S}_2^{\,2}, \mathbf{S}^2, S_z\right\}$, which form a C.S.C.O. as well.

We shall denote the vectors of this new basis by $|S, M\rangle$, with the eigenvalues $\mathbf{S}_1^{\,2}$ and $\mathbf{S}_2^{\,2}$ (which is trivial, since they not only remain the same in both bases, but are actually merely multiples of the identity operator $\mathbb{1}$). The new observables satisfy the following set of equations:

$$\mathbf{S}_1^{\,2}|S, M\rangle = \mathbf{S}_2^{\,2}|S, M\rangle = \frac{3}{4}\hbar^2|S, M\rangle \tag{6.18}$$

$$\mathbf{S}^2|S, M\rangle = S(S+1)\hbar^2|S, M\rangle \tag{6.19}$$

$$S_z|S, M\rangle = M\hbar|S, M\rangle \tag{6.20}$$

Since **S** is an angular momentum, the quantum number *S* must be either a positive integer, or half-integer. Then $M \in \{-S, -S+1, -S+2, \ldots S-1, +S\}$. Furthermore, we need to recall the action of the following ladder operators[35] upon the basis vectors $|S, M\rangle$:

$$S_{\pm}|S, M\rangle = \hbar\sqrt{S(S+1) - M(M+1)}\,|S, M \pm 1\rangle \tag{6.21}$$

With the aforementioned, we have set the stage for considering the coupling of two spin-1/2's:

---

[35] There are plenty of other methods to find an expression for these new basis vectors $|S, M\rangle$ in terms of those of the old basis, e.g. elementary computation and diagonalization of the resulting 4x4 matrices, and the general somewhat more formal methods involving definitions such as the Clebsch-Gordan coefficients or the Wigner 3j-symbols etc., which are discussed in Appendix A1.4: Clebsch-Gordan coefficients, cf. also equation (6.49).

The coupling of two spin-½'s.

A system consisting of two spin-½'s can possess the total spin *S*=1 and *S*=0.***

From the fundamental Lemma of representation theory[36] it follows that

$$D^{(j_1)} \otimes D^{(j_2)} = \bigoplus_{m=|j_1-j_2|}^{j_1+j_2} D^{(m)} \tag{6.22}$$

where in our simplest possible case $j_1 = j_2 = ½$, so that we have to consider the direct sum of merely two orthogonal subspaces $\mathcal{H}$ *(S=1)* and $\mathcal{H}$ *(S=0)* (which we shall examine separately); in our notation used before this results in:

$$\mathcal{H}^{(1/2)} \otimes \mathcal{H}^{(1/2)} = \mathcal{H}(S=1) \oplus \mathcal{H}(S=0)\,, \tag{6.23}$$

which is plausible: If we consider the dimensions of the involved Hilbert spaces, equation (6.23) immediately implies

$$\begin{array}{ccccccc} \dim\left\{\mathcal{H}^{(1/2)} \otimes \mathcal{H}^{(1/2)}\right\} & = & \dim \mathcal{H}(S=1) & + & \dim \mathcal{H}(S=0) & \Leftrightarrow & \\ 2 & \bullet & 2 & = & 3 & + & 1 \end{array}$$

The subspace $\mathcal{H}$ (*S*=1)

In this subspace we find a ***spin triplet***, since *M* is varying between –*S* and +*S* in integer steps. In the tensor product space $\mathcal{H} := \mathcal{H}(½,½) := \mathcal{H}^{(1/2)} \otimes \mathcal{H}^{(1/2)}$ the ket vector $|+,+\rangle$ is the only eigenvector of S_z associated with *M=1.* $\left[\mathbf{S}^2, S_z\right] = 0$, and the value *M*=1 is not degenerate, thus $|+,+\rangle$ is an eigenvector of $\mathbf{S}^2$ as well. The corresponding value of *S* must be 1 as well (**). Accordingly, we can choose the phase of the ket $|S=1,\ M=1\rangle$ such that:

$$|S=1,\ M=1\rangle = |+,+\rangle\,. \tag{6.24}$$

---

[36] This simply means when applied to our examined case: The tensor product formed by two arbitrary spin state spaces belonging to the spins j_1 and j_2 , respectively, can be expressed by the direct sum of the irreducible representations ****.

In order to find the other states of the triplet, we can now apply the ladder operator $S_{\pm}$ of equation (6.21) successively to get the states with lower M values yielding in the first step:

$$S_- \ |1,1\rangle = \hbar\sqrt{1(1+1)-(1(1-1)} \ |1,0\rangle = \hbar\sqrt{2} \ |1,0\rangle \tag{6.25}$$

Thus

$$|1,0\rangle \ = \ \frac{1}{\hbar\sqrt{2}} S_- |+,+\rangle . \tag{6.26}$$

But since $S_- = S_{1-}+S_{2-}$ we obtain:

$$\begin{aligned} |1,0\rangle \ &= \ \frac{1}{\hbar\sqrt{2}}(S_{1-}+S_{2-}) \ |+,+\rangle \\ &= \ \frac{1}{\hbar\sqrt{2}}\left[\hbar \ |-,+\rangle + \hbar \ |+,-\rangle\right] \\ &= \ \frac{1}{\sqrt{2}}\left[|-,+\rangle + \hbar \ |+,-\rangle\right] \end{aligned} \tag{6.27}$$

In a second step, we can apply S_- to the state $|1,0\rangle$ which results in the following:

$$\begin{aligned} |1,-1\rangle \ &= \ \frac{1}{\hbar\sqrt{2}} S_- \ |1,0\rangle \\ &= \ \frac{1}{\hbar\sqrt{2}}(S_{1-}+S_{2-}) \ \frac{1}{\sqrt{2}}\left[|-,+\rangle + |+,-\rangle\right] \\ &= \ \frac{1}{2\hbar} \ \left[\hbar|-,-\rangle + \hbar|-,-\rangle\right] \\ &= |-,-\rangle \end{aligned} \tag{6.28}$$

The subspace $\mathcal{H}$ (S=0)

For S=0 there is only one state, because M can only have the value 0. We can determine this vector $|0,0\rangle$ by applying the condition that it has to be orthogonal to the aforementioned three vectors $|1,M\rangle$. From the fact that this ket vector has to be or-

thogonal simultaneously to $|1,1\rangle = |+,+\rangle$ as well as to $|1,-1\rangle = |-,-\rangle$, we gather that it must be a linear combination of the form:

$$|0,0\rangle = a|+,-\rangle + b|-,+\rangle \tag{6.29}$$

with the normalization condition $|a|^2 + |b|^2 = 1$. But the scalar product with the third ket vector $|1,0\rangle$ of the eigenvectors of the three-dimensional subspace $\mathcal{H}$ (*S*=1) must vanish, and thus

$$\frac{1}{\sqrt{2}}(a+b) = 0 \tag{6.30}$$

so that we finally get the following representation of $|0,0\rangle$ in the old basis:

$$|0,0\rangle = \frac{1}{\sqrt{2}}\left[|+,-\rangle - |-,+\rangle\right]. \tag{6.31}$$

Comment. In the case of the H_2 molecule, the application of the procedure described above to the two nuclei in the molecule leads to the existence of the two nuclear spin modifications of the hydrogen molecule, since the protons in the nuclei are fermions with spin ½. The spin-triplet modification of hydrogen is termed *ortho*-hydrogen (*o*-H_2), whereas the spin singlet modification is termed *para*-hydrogen (*p*-H_2).

A1.3: Spherical harmonics

The spherical harmonics $Y_l^m(\vartheta,\varphi)$ are single-valued, continuous, bounded, complex functions of the angular coordinates ϑ and φ. By definition, the Y_l^m s are the angular portion of the solution to *Laplace's equation* in spherical coordinates (r,ϑ,φ), which if we choose the separation approach $F(\vartheta,\varphi) = \Phi(\varphi)\Theta(\vartheta)$ reads

$$\frac{\Phi(\varphi)}{\sin\vartheta}\frac{d}{d\vartheta}\left(\sin\vartheta\frac{d\Theta}{d\vartheta}\right) + \frac{\Theta(\vartheta)}{\sin^2\vartheta}\frac{d^2\Phi(\varphi)}{d\varphi^2} + l(l+1)\Theta(\vartheta)\Phi(\varphi) = 0\,. \tag{6.32}$$

Here $\vartheta \in [0, \pi]$ is the polar coordinate, and $\varphi \in [0, 2\pi)$ the azimuthal coordinate. For our purposes, it is more convenient to see the spherical harmonics as the angular parts of the eigenfunctions of the z-component $\hat{L}_z$, and of the square the operator of angular momentum $\hat{\mathbf{L}}^2$ (in units of $\hbar$), which of course is equivalent to equation (6.32):

$$\hat{L}_z \, Y_l^m(\vartheta, \varphi) = m\hbar \cdot Y_l^m(\vartheta, \varphi) , \tag{6.33}$$

$$\hat{\mathrm{L}}^2 Y_l^m(\vartheta, \varphi) = l(l+1)\hbar^2 \cdot Y_l^m(\vartheta, \varphi) , \tag{6.34}$$

with $l \in \mathbb{N}_0$ and $-l \le m \le l$. It is worthwhile noting that the spherical harmonics represent the wave functions of the rotational states $\left| l, m \right\rangle$ of a linear molecule, i.e.,

$$\left| l, m \right\rangle \equiv Y_l^m(\vartheta, \varphi) . \tag{6.35}$$

The Y_l^m s constitute a mutually orthogonal and normalized set of eigenfunctions, on the unit sphere, i.e.,

$$\left\langle l, m \middle| l', m' \right\rangle = \int Y_l^m(\vartheta, \varphi)^* Y_{l'}^{m'}(\vartheta, \varphi) \, d\Omega = \delta_{ll'} \delta_{mm'} \tag{6.36}$$

where $d\Omega$ is an infinitesimal element of the solid angle, $d\Omega = \sin\vartheta d\vartheta d\varphi$. Applying the definition for the phases according to Condon and Shortley [Condon and Shortley 1951] gives.

$$Y_l^m(\vartheta, \varphi)^* = (-1)^m Y_l^{-m}(\vartheta, \varphi) . \tag{6.37}$$

Sometimes it is useful to use the ***Racah spherical harmonics*** defined as

$$C_{lm}(\vartheta, \varphi) = \left(\frac{4\pi}{2l+1} \right)^{1/2} Y_l^m(\vartheta, \varphi) , \tag{6.38}$$

since many expressions are simplified by their introduction. The Racah spherical harmonics constitute an orthogonal system, but obviously this system is not normalized. The spherical harmonics have a definite symmetry upon reflection of coordinates at the

origin. If we denote the reflected coordinates as ϑ', φ' we have the following symmetry relation:

$$C_{lm}(\vartheta', \varphi') = (-1)^l C_{lm}(\vartheta, \varphi) \tag{6.39}$$

The product of two spherical harmonics with the same arguments is given by the following linear combination of spherical harmonics

$$C_{l_1 m_1}(\vartheta, \varphi) C_{l_2 m_2}(\vartheta, \varphi) = \sum_{l,m} C^{0,0,0}_{l_1,l_2,l} C^{m_1,m_2,m}_{l_1,l_2,l} C_{lm}(\vartheta, \varphi) \tag{6.40}$$

The coefficients $C^{m_1,m_2,m}_{l_1,l_2,l}$ in the expansion formula (6.40) are called the ***Clebsch-Gordan coefficients***, and are defined in the following paragraph.

A1.4: Clebsch-Gordan coefficients

The wave function for a system consisting of two *uncoupled* quantum-mechanical rotators with rotational quantum numbers j_1 and j_2 is obtained by forming the (tensor) product of one-particle wave functions:

$$\left| j_1, j_2;\ m_1, m_2 \right\rangle = \left| j_1, m_1 \right\rangle \otimes \left| j_2, m_2 \right\rangle . \tag{6.41}$$

In the case of coupling between the two rotators, the total wave function of the system is obtained as the following linear combination of the uncoupled two-particle wave functions (6.41) with different values of the total magnetic quantum number *m*:

$$\left| j_1, j_2;\ j, m \right\rangle = \sum_{m_1,m_2} \left| j_1, j_2;\ m_1, m_2 \right\rangle \underbrace{\left\langle j_1, j_2;\ m_1, m_2 \middle| j_1, j_2;\ j, m \right\rangle}_{=:\ C^{m_1,m_2,m}_{j_1,j_2,j}} \tag{6.42}$$

corresponding to the vector addition $\mathbf{j} = \mathbf{j_1} + \mathbf{j_2}$. Equation (6.42) describes a *unitary* transformation which implies the following relations:

$$\sum_{m_1,m_2} C^{m_1,m_2,m}_{j_1,j_2,j} C^{m_1,m_2,m'}_{j_1,j_2,j'} = \delta_{jj'}\delta_{mm'} \tag{6.43}$$

$$\sum_{m_1,m_2} C^{m_1,m_2,m}_{j_1,j_2,j} C^{m_1',m_2',m}_{j_1,j_2,j} = \delta_{m_1 m_1'}\delta_{m_2 m_2'} \tag{6.44}$$

The vector addition $\mathbf{j} = \mathbf{j_1} + \mathbf{j_2}$ implies the two following conditions for non-vanishing Clebsch-Gordan coefficients:

(i) $$m = m_1 + m_2 \text{, and} \tag{6.45}$$

(ii) "*triangle condition*" $$j \in \left\{ j_1 + j_2, j_1 + j_2 - 1, \ldots, \left| j_1 - j_2 \right| \right\}. \tag{6.46}$$

The phases of the coupled wave functions (6.42) are chosen such that

$$C^{m_1,m_2,m}_{j_1,j_2,j} \in \mathbb{R} \text{, and} \tag{6.47}$$

$$C^{j_1,j_2,j_1+j_2}_{j_1,j_2,j_1+j_2} = 1. \tag{6.48}$$

The symmetry of the total wave functions is intimately related to the symmetry of the Clebsch-Gordan coefficients, which are most conveniently expressed in terms of the ***Wigner 3-j symbols*** defined by

$$\begin{pmatrix} j_1 & j_2 & j_3 \\ m_1 & m_2 & m_3 \end{pmatrix} := \frac{(-1)^{j_2 - j_1 + m_3}}{\sqrt{(2j_3+1)}} C^{m_1,m_2,-m_3}_{j_1,j_2,j_3}. \tag{6.49}$$

The Wigner 3-j symbols are invariant under cyclic permutations of the columns, for non-cyclic permutations, they have to be multiplied by a phase factor:

$$\begin{pmatrix} j_1 & j_2 & j_3 \\ m_1 & m_2 & m_3 \end{pmatrix} = \begin{pmatrix} j_2 & j_3 & j_1 \\ m_2 & m_3 & m_1 \end{pmatrix} = (-1)^{j_1+j_2+j_3} \begin{pmatrix} j_2 & j_1 & j_3 \\ m_2 & m_1 & m_3 \end{pmatrix}, etc. \tag{6.50}$$

$$\begin{pmatrix} j_1 & j_2 & j_3 \\ -m_1 & -m_2 & -m_3 \end{pmatrix} = (-1)^{j_1+j_2+j_3} \begin{pmatrix} j_1 & j_2 & j_3 \\ m_1 & m_2 & m_3 \end{pmatrix}. \tag{6.51}$$

Using the relation (6.49) we can easily find the following symmetry relations for the Clebsch-Gordan coefficients:

$$
\begin{aligned}
C_{j_1,j_2,j_3}^{m_1,m_2,m_3} &= (-1)^{j_1+j_2-j_3}\, C_{j_1,j_2,j_3}^{-m_1,-m_2,-m_3} \\
&= (-1)^{j_1-m_1} \sqrt{\frac{2j_3+1}{2j_2+1}} C_{j_1,j_2,j_3}^{m_1,-m_2,-m_3} \\
&= (-1)^{j_1+j_2-j_3}\, C_{j_2,j_1,j_3}^{m_2,m_1,m_3} \\
&= (-1)^{j_2+m_2} \sqrt{\frac{2j_3+1}{2j_2+1}} C_{j_2,j_3,j_1}^{-m_2,m_3,m_1} \\
&= (-1)^{j_2+m_2} \sqrt{\frac{2j_3+1}{2j_2+1}} C_{j_3,j_2,j_1}^{-m_3,m2,-m_1} \\
&= (-1)^{j_1-m_1} \sqrt{\frac{2j_3+1}{2j_2+1}} C_{j_3,j_1,j_2}^{m_3,-m_1,m_2}
\end{aligned}
\tag{6.52}
$$

7 Appendix B: Experimental details and technical drawings

7.1 Crystal growing parameters

The parameters for optimal crystal growth are given in the following short overview which is meant as a brief step-by-step instruction manual or “recipe” for the experimentalist seeking to produce *para*-hydrogen crystals of high optical quality.

1. Evacuate the recipient (cryostat) and tube system to approximately 10^{-5} mbar by switching on the pump system and keeping the valves V2-V5 open while V1 is closed, see Figure 7-1.
2. Set the flow rate to 75 sccm at the mass flow controller (MFC) and close valves V2-V4. Then carefully open valve V1 until the pressure in the tube system reaches approx. 10 bar, then close the valve V1.
3. Turn the compressor on by turning the key switch at the compressor control unit.

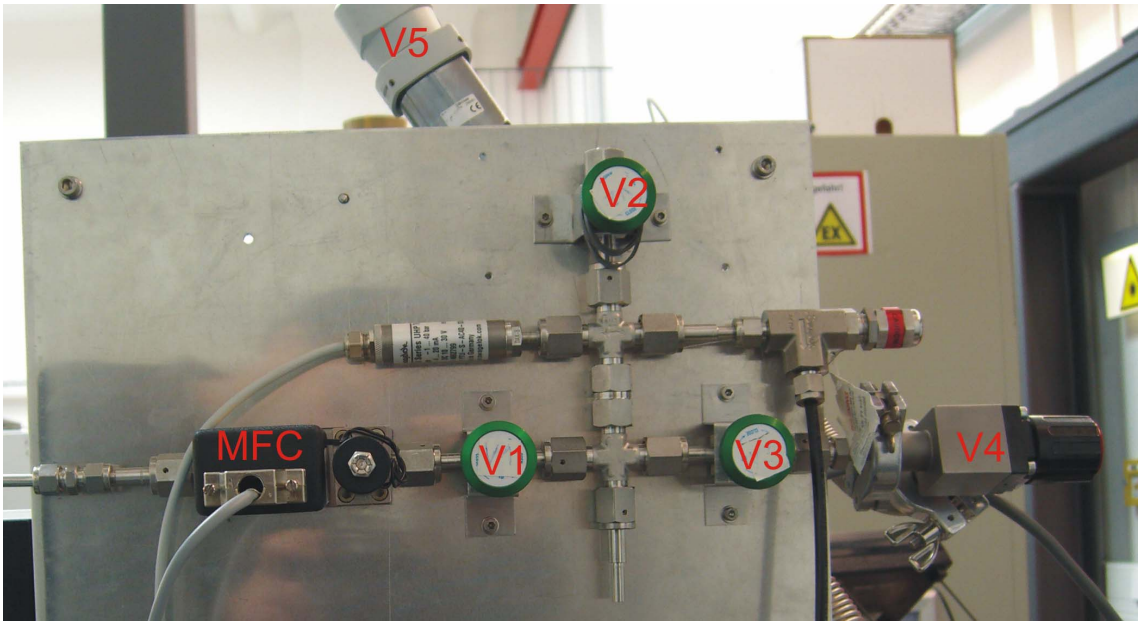

Figure 7-1: Gas inlet and pump system.

4. At the temperature controller, set the temperature for loop 1 – controlling the temperature at (A) – to 13.95 K and for loop 2 – controlling the temperature at (C) – to 15.1 K. It takes approximately one hour and a half to cool down from room temperature.
5. Slowly open valves V1 and V2. Wait until the entire cell is filled with liquid *p*-H_2. This takes approximately one hour for the 68.5 mm long cell.
6. When the cell is filled, set the flow rate to the maximum value of 150 sccm until the pressure reaches 30 bar.
7. Set the temperature at (A) to approximately 14.2 K so that the crystal just starts growing at the copper post in the upper part of the cell.
8. Ramp down the temperature at (A) at a rate of 1.5 K in 2 hours by running the appropriate program on the temperature controller (by pressing the PROGRAM and ENTER button on the controller). Set the additional heater current to 60 mA.
9. Ramp down the temperatures at (A) and (C) at a rate of 0.1 K/hr and 0.2 K/hr by pressing the RAMP button on the temperature controller.
10. At the end of this process, the temperatures reach approximately T(A)= 2.4 K, T(C)= 3.5 K, and T(D)= 3.6 K: The crystal is now ready for the frequency conversion !

7.2 Technical drawings

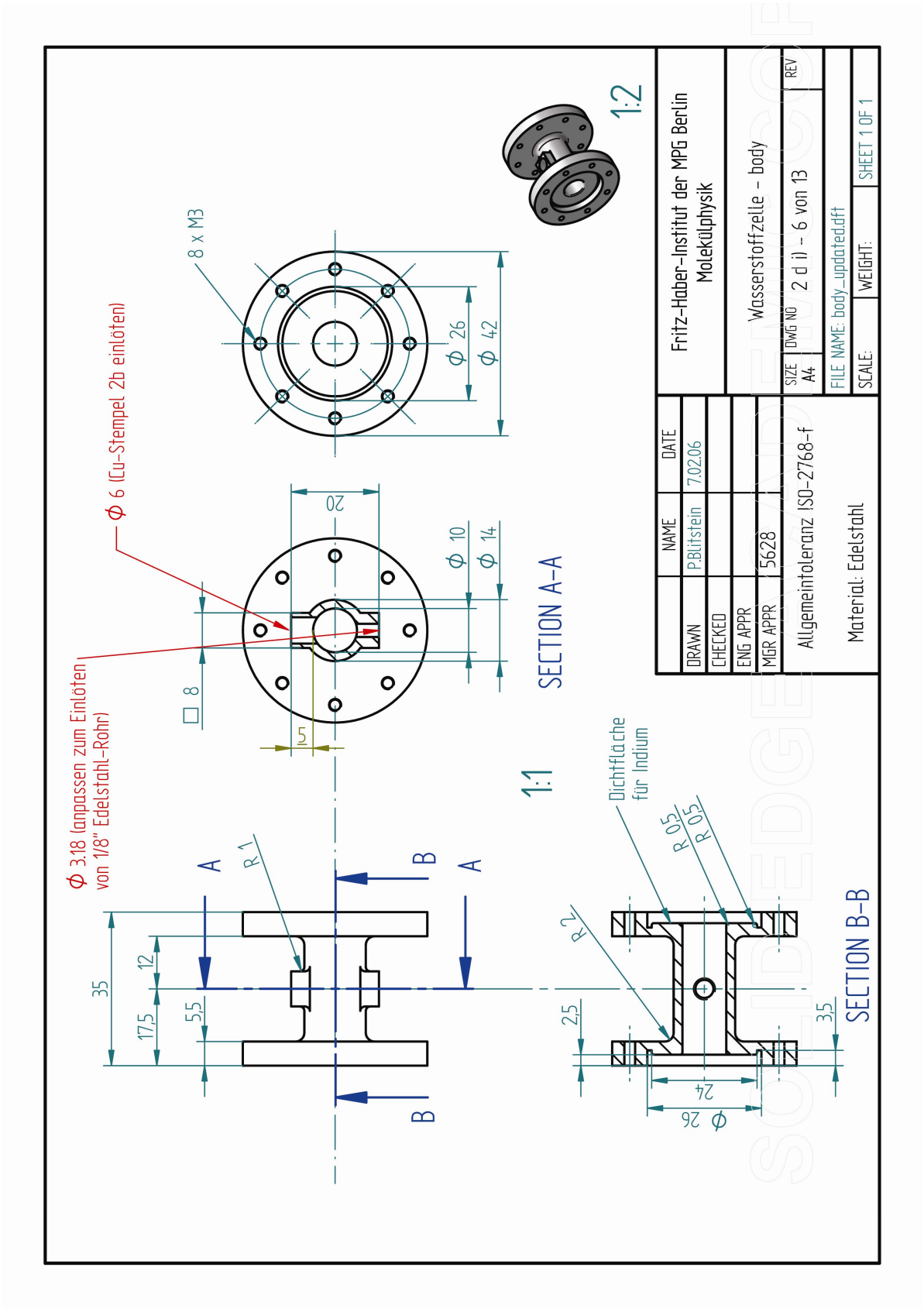

Figure 7-2: SolidEdge ® draft of the 30 mm hydrogen Raman cell body.

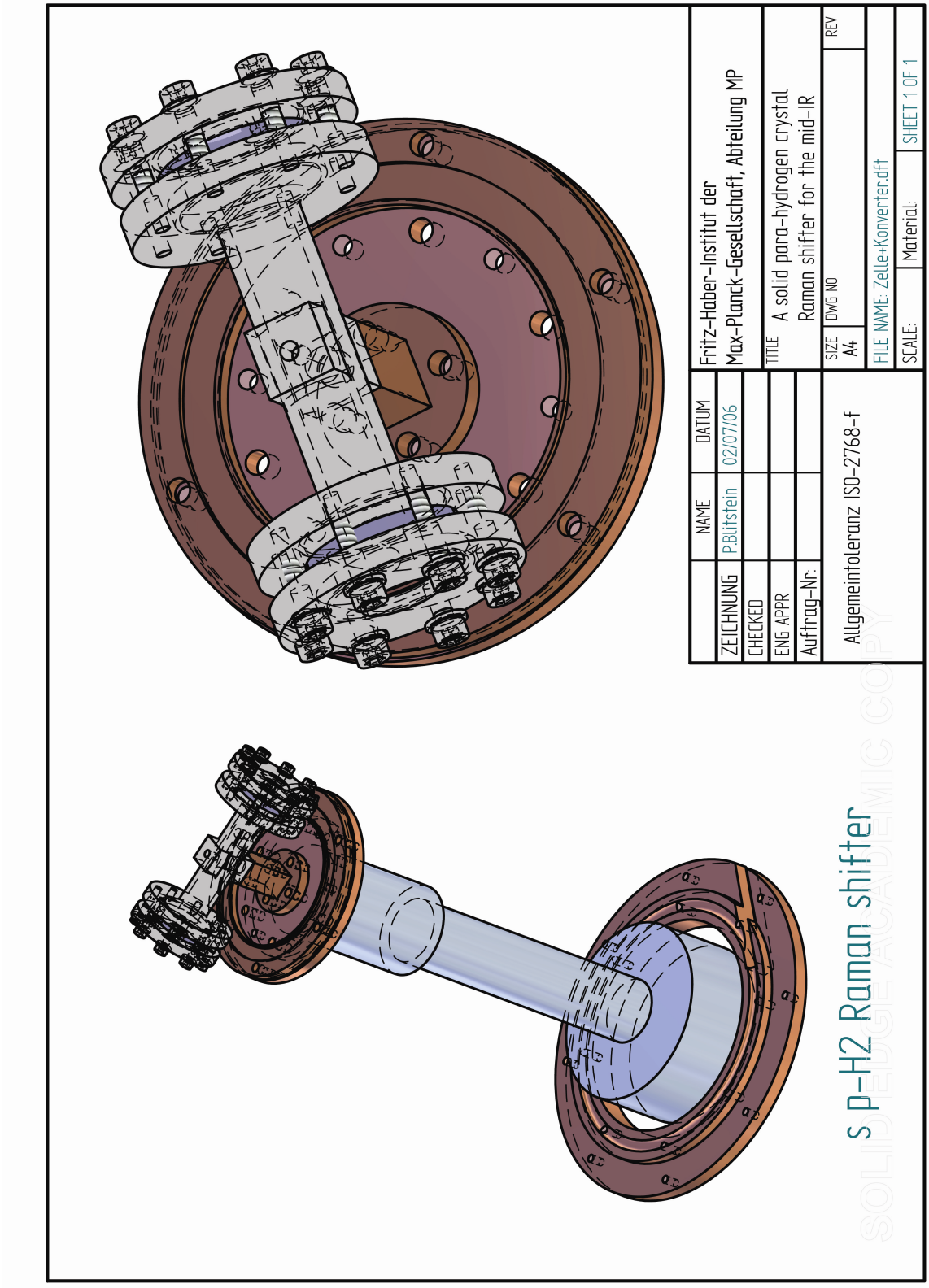

Figure 7-3: *SolidEdge ® assembly of asymmetric 68.5 mm hydrogen Raman cell mounted on the cold finger of the closed-cycle refrigerator cryostat.*

8 Bibliography

Bargheer, M., P. Dietrich and N. Schwentner (2001). "Spectroscopy and photodissociation of ClF in rare gas solids." The Journal of Chemical Physics **115**(1): 149-157.

Berghof, V., M. Martins, B. Schmidt and N. Schwentner (2002). "Vibrational overtones and rotational structure of HCl in rare gas matrices." The Journal of Chemical Physics **116**(21): 9364-9373.

Bloembergen, N. (1967). "The Stimulated Raman Effect." American Journal of Physics **35**(11): 989-1023.

Boyd, G., W. Johnston and I. Kaminow (1969). "Optimization of the stimulated Raman scattering threshold." IEEE Journal of Quantum Electronics **5**(4): 203-206.

Bret, G. G. and M. M. Denariez (1966). "STIMULATED RAMAN EFFECT IN ACETONE AND ACETONE---CARBON-DISULFIDE MIXTURES." Applied Physics Letters **8**(6): 151-154.

Buckingham, A. D. (1965). "Theory of the Stimulated Raman and Related Effects." The Journal of Chemical Physics **43**(1): 25-31.

Casaes, R., R. Provencal, J. Paul and R. J. Saykally (2002). "High resolution pulsed infrared cavity ringdown spectroscopy: Application to laser ablated carbon clusters." The Journal of Chemical Physics **116**(15): 6640-6647.

Chan, M.-C., S. S. Lee, M. Okumura and T. Oka (1991). "Laser spectroscopic studies of the pure rotational $U_0(0)$ and $W_0(0)$ transitions of solid parahydrogen." The Journal of Chemical Physics **95**(1): 88-97.

Chan, M.-C., M. Okumura, C. M. Gabrys, L.-W. Xu, B. D. Rehfuss and T. Oka (1991a). "Erratum: High-resolution infrared spectroscopy of solid hydrogen [Phys. Rev. Lett. **66**, 2060 (1991)]." Physical Review Letters **67**(15): 2113.

Chan, M.-C., M. Okumura, C. M. Gabrys, L.-W. Xu, B. D. Rehfuss and T. Oka (1991b). "High-resolution infrared spectroscopy of solid hydrogen." Physical Review Letters **66**(16): 2060-2063.

Clements, W. R. L. and B. P. Stoicheff (1968). "RAMAN LINEWIDTHS FOR STIMULATED THRESHOLD AND GAIN CALCULATIONS." Applied Physics Letters **12**(8): 246-248.

Cohen-Tannoudji, C., B. Diu and F. Laloë (1999). Quantenmechanik. Berlin, De Gruyter.

Condon, E. U. and G. Shortley (1951). The Theory of Atomic Spectra Cambridge, England, Cambridge University Press.

Cotter, D., D. C. Hanna and R. Wyatt (1975). "Infrared stimulated Raman generation: Effects of gain focussing on threshold and tuning behaviour." Applied Physics A: Materials Science & Processing **8**(4): 333-340.

Dunham, J. L. (1932). "The Energy Levels of a Rotating Vibrator." Physical Review **41**(6): 721-731.

Eckhardt, G., R. W. Hellwarth, F. J. McClung, S. E. Schwarz, D. Weiner and E. J. Woodbury (1962). "Stimulated Raman Scattering From Organic Liquids." Physical Review Letters **9**(11): 455-457.

Fink, U., T. A. Wiggins and D. H. Rank (1965). "Frequency and intensity measurements on the quadrupole spectrum of molecular hydrogen." Journal of Molecular Spectroscopy **18**(4): 384-395.

Foltz, J. V., D. H. Rank and T. A. Wiggins (1966). "Determinations of some hydrogen molecular constants." Journal of Molecular Spectroscopy **21**(1-4): 203-216.

Garcia, J. D. (1966). "Radiative Corrections to the Energies of Atoms and Molecules." Physical Review **147**(1): 66-68.

Gühr, M. and N. Schwentner (2005). "Effective chromophore potential, dissipative trajectories, and vibrational energy relaxation: Br[sub 2] in Ar matrix." The Journal of Chemical Physics **123**(24): 244506.

Hagenlocker, E. E., R. W. Minck and W. G. Rado (1967). "Effects of Phonon Lifetime on Stimulated Optical Scattering in Gases." Physical Review **154**(2): 226-233.

Haken and Wolf (1998). Molekülphysik und Quantenchemie, Springer.

Hakuta (2002). Slow Light in Solid Hydrogen

Hakuta, K., M. Suzuki, M. Katsuragawa and J. Z. Li (1997). "Self-Induced Phase Matching in Parametric Anti-Stokes Stimulated Raman Scattering." Physical Review Letters **79**(2): 209-212.

Hartig, W. and W. Schmidt (1979). "A broadly tunable IR waveguide Raman laser pumped by a dye laser." Applied Physics A: Materials Science & Processing **18**(3): 235-241.

Heitler, W. and G. Herzberg (1929). Naturwissenschaft **17**: 673.

Helen, S. F. (1967). "Quantum Theory of Stimulated Raman Scattering." The Journal of Chemical Physics **47**(8): 2554-2556.

Hellwarth, R. W. (1963). "Theory of Stimulated Raman Scattering." Physical Review **130**(5): 1850-1852.

Herriott, D., H. Kogelnik and R. Kompfner (1964). "Off-axis paths in spherical mirror interferometers." Appl. Opt. **3**: 523.

Herriott, D. R. and H. J. Schulte (1965). "Folded optical delay lines." Appl. Opt. **4**: 883.

Herzberg, G. (1950). Spectra of Diatomic Molecules. Toronto, Van Nostrand.

Jackson, J. D. (1999). Classical Electrodynamics. N.Y., John Wiley & Sons, Inc.

Kato, Y. and H. Takuma (1971). "Experimental Study on the Wavelength Dependence of the Raman Scattering Cross Sections." The Journal of Chemical Physics **54**(12): 5398-5402.

Katsuragawa, M. and K. Hakuta (2000). "Raman gain measurement in solid parahydrogen " Optics Letters **25**(3): 177-179.

Keesom, D. Smedt and Moody (1930). "On the Crystal Structure of para-Hydrogen at Liquid Helium temperature." Proc. Kon. Acad. v. Amsterdam **33**: 814.

Kolos, W. and L. Wolniewicz (1964a). "Accurate Adiabatic Treatment of the Ground State of the Hydrogen Molecule." The Journal of Chemical Physics **41**(12): 3663-3673.

Kolos, W. and L. Wolniewicz (1964b). "Accurate Computation of Vibronic Energies and of Some Expectation Values for H_2, D_2, and T_2." The Journal of Chemical Physics **41**(12): 3674-3678.

Kuroda, K., A. Koreeda, S. Takayanagi, M. Suzuki and K. Hakuta (2003). "High-resolution coherent Raman spectroscopy of vibrons in solid parahydrogen." Physical Review B (Condensed Matter and Materials Physics) **67**(18): 184303-184305.

Kuyanov, K., E., T. Momose and A. F. Vilesov (2004). "Solid Hydrogen Raman Shifter for the Mid-Infrared Range (4.4-8 μm)." Applied Optics **43**(32): 6023-6029.

Lallemand, P., P. Simova and G. Bret (1966). "Pressure-Induced Line Shift and Collisional Narrowing in Hydrogen Gas Determined by Stimulated Raman Emission." Physical Review Letters **17**(25): 1239-1241.

Laubereau, A., L. Greiter and W. Kaiser (1974). "Intense tunable picosecond pulses in the infrared." Applied Physics Letters **25**(1): 87-89.

Laubereau, A., D. v. d. Linde and W. Kaiser (1971). "Decay Time of Hot TO Phonons in Diamond." Physical Review Letters **27**(12): 802-805.

Laubereau, A., D. v. d. Linde and W. Kaiser (1972). "Direct Measurement of the Vibrational Lifetimes of Molecules in Liquids." Physical Review Letters **28**(18): 1162-1165.

Laubereau, A., G. Wochner and W. Kaiser (1976). "Ultrafast coherent excitation and probing of molecular vibrations with isotopic substructure." Physical Review A (General Physics) **13**(6): 2212-2225.

Linde, D. v. d., A. Laubereau and W. Kaiser (1971). "Molecular Vibrations in Liquids: Direct Measurement of the Molecular Dephasing Time; Determination of the Shape of Picosecond Light Pulses." Physical Review Letters **26**(16): 954-957.

Long, D. A. (2002). The Raman Effect. N.Y., John Wiley & Sons.

Maier, M. (1976). "Applications of stimulated Raman scattering." Applied Physics A: Materials Science & Processing **11**(3): 209-231.

Maiman, T. H. (1960). "Stimulated Optical Radiation in Ruby." Nature **187**(4736): 493-494.

McCall, B., M. Fushitani, Y. Miyamoto, T. Momose, T. Oka and R. S. e. al. (2003). Generation of Infrared Radiation by Stimulated Raman Scattering in Liquid and Solid Parahydrogen.

McLennan, J. C. and J. A. McLeod (1929). "Raman effect with liquid oxygen, nitrogen and hydrogen." Nature **123**: 160.

Merritt, J. M., S. Rudic and R. E. Miller (2006). "Infrared laser spectroscopy of CH[sub 3][centered ellipsis]HF in helium nanodroplets: The exit-channel complex of the F + CH[sub 4] reaction." The Journal of Chemical Physics **124**(8): 084301.

Miki, M. and T. Momose (2000). "Rovibrational transitions and nuclear spin conversion of methane in parahydrogen crystals." Low Temperature Physics **26**(9): 661-668.

Minck, R. W., R. W. Terhune and W. G. Rado (1963). "LASER-STIMULATED RAMAN EFFECT AND RESONANT FOUR-PHOTON INTERACTIONS IN GASES H_2, D_2, AND CH_4." Applied Physics Letters **3**(10): 181-184.

MISHRA, A. P. and T. K. BALASUBRAMANIAN (1997). "Rovibrational matrix elements of multipole moments of the H_2 molecule." Molecular Physics **90**(6): 895-902.

Momose, T., H. Hoshina, N. Sogoshi, H. Katsuki, T. Wakabayashi and T. Shida (1998). "Tunneling chemical reactions in solid parahydrogen: A case of $CD_3 + H_2 \rightarrow CD_3H + H$ at 5 K." The Journal of Chemical Physics **108**(17): 7334-7338.

Momose, T., H. Katsuki, H. Hoshina, N. Sogoshi, T. Wakabayashi and T. Shida (1997). "High-resolution laser spectroscopy of methane clusters trapped in solid parahydrogen." The Journal of Chemical Physics **107**(19): 7717-7720.

Momose, T., M. Masaaki, W. Tomonari, S. Tadamasa, C. Man-Chor, S. L. Steven and O. Takeshi (1997). "Infrared spectroscopic study of rovibrational states of methane trapped in parahydrogen crystal." The Journal of Chemical Physics **107**(19): 7707-7716.

Momose, T., M. Miki, M. Uchida, T. Shimizu, I. Yoshizawa and T. Shida (1995). "Infrared spectroscopic studies on photolysis of methyl iodide and its clusters in solid parahydrogen." The Journal of Chemical Physics **103**(4): 1400-1405.

Momose, T., D. P. Weliky and T. Oka (1992). "The stimulated Raman gain spectrum of the Q1(0) transition of solid parahydrogen." Journal of Molecular Spectroscopy **153**(1-2): 760-761.

Nauta, K. and R. E. Miller (2001). "Infrared spectroscopy and structures of Ar_n--HF in liquid helium nanodroplets." The Journal of Chemical Physics **115**(22): 10138-10145.

Pantell, R. H. and H. E. Puthoff (1969). Fundamentals of Quantum Electronics. N.Y., John Wiley & Sons.

Paul, J. B., R. A. Provencal, C. Chapo, A. Petterson and R. J. Saykally (1998). "Infrared cavity ringdown spectroscopy of water clusters: O--D stretching bands." The Journal of Chemical Physics **109**(23): 10201-10206.

Pauli, W. (1925). Z. Physik **31**: 765.

Pauli, W. (1940). "The Connection Between Spin and Statistics." Physical Review **58**(8): 716-722.

Pauli, W. (1946). Exclusion Principle and Quantum Mechanics in Nobel Lectures, Physics 1942-1962

Amsterdam, 1964, Elsevier Publishing Company

Placzek, G. (1934). Rayleigh-Streuung und Raman Effekt. Leipzig, Akademische Verlagsanstalt M. B. H.

Rabinowitz, P., A. Kador, R. Brickman and W. Schmidt (1976). "Waveguide H_2 Raman laser." Applied Optics **15**(9): 2005-2006.

Rabinowitz, P., B. Perry and N. Levinos (1986). " A continuously tunable sequential Stokes Raman laser." IEEE Jornal of Quantum Electronics **22**(6): 797- 802.

Raman, C. V. and K. S. Krishnan (1928). "A New Type of Secondary Radiation." Nature **121**: 501.

Rasetti, F. (1929). "Incoherent Scattered Radiation in Diatomic Molecules." Physical Review **34**(2): 367-371.

Rudic, S., J. M. Merritt and R. E. Miller (2006). "Infrared laser spectroscopy of the CH_3--HCN radical complex stabilized in helium nanodroplets." The Journal of Chemical Physics **124**(10): 104305.

Shen, Y.-R. (1975). Stimualted Raman Scattering. Light scattering in solids. M. Cardona. Berlin ; Heidelberg ; New York ; London ; Paris ; Tokyo Springer. **8:** 275-329.

Shen, Y. R. (1965). "Theory of Stimulated Raman Effect. II." Physical Review **138**(6A): A1741-A1746.

Shen, Y. R. and N. Bloembergen (1965). "Theory of Stimulated Brillouin and Raman Scattering." Physical Review **137**(6A): A1787-A1805.

Silvera, I. F. (1980). "The solid molecular hydrogens in the condensed phase: Fundamentals and static properties." Reviews of Modern Physics **52**(2): 393-452.

Silvera, I. F. and V. V. Goldman (1978). "The isotropic intermolecular potential for H_2 and D_2 in the solid and gas phases." The Journal of Chemical Physics **69**(9): 4209-4213.

Simon, T., E. F. Mario, K. Hiroyuki, H. Hiromichi, W. Tomonari and M. Takamasa (1999). "High resolution infrared absorption spectra of methane molecules isolated in solid parahydrogen matrices." The Journal of Chemical Physics **111**(9): 4191-4198.

Smekal, A. (1923). Naturwiss. **11**: 873.

Soots, V., E. J. Allin and H. L. Welsh (1965). Can. J. Phys. **43**: 1985.

Souers, P. C. (1986). Hydrgen Properties for Fusion Energy. Berkeley, University of California Press.

Stoicheff, B. (1965). "Acoustical Spectroscopy Using Optical Masers." The Journal of the Acoustical Society of America **37**(6): 1204.

Stoicheff, B. P. (1963). "Characteristics of stimulated raman radiation generated by coherent light." Physics Letters **7**(3): 186-188.

Stoicheff, B. P. (2002). "Heitler, Herzberg Observed that Nitrogen Nuclei Obey Bose." Physics Today **55**(11): 99.

Sussmann, R., T. Weber, E. Reidle and H.-J. Neusser (1992). Opt. Comm. **88**: 408.

Suzuki, M., M. Katsuragawa, R. S. D. Sihombing, J. Z. Li and K. Hakuta (1998). "Solid Hydrogen for Nonlinear Optics." Journal of Low Temperature Physics **111**(3 - 4): 463-468.

Tam, S. and M. E. Fajardo (2000). "Observation of the high-resolution infrared absorption spectrum of CO_2 molecules isolated in solid parahydrogen." Low Temperature Physics **26**(9): 653-660.

Tam, S., M. E. Fajardo, H. Katsuki, H. Hoshina, T. Wakabayashi and T. Momose (1999). "High resolution infrared absorption spectra of methane molecules isolated in solid parahydrogen matrices." The Journal of Chemical Physics **111**(9): 4191-4198.

Toennies, J. P. and A. F. Vilesov (2004). "Suprafluide Heliumtröpfchen: außergewöhnlich kalte Nanomatrices für Moleküle und molekulare Komplexe." Angewandte Chemie **116**(20): 2674-2702.

Trutna, W. R. and R. L. Byer (1980). "Multiple-pass Raman gain cell." Appl. Opt. **19**: 301.

van Kranendonk, J. (1983). Solid Hydrogen. N. Y. and London, Plenum Press.

Wang, C.-S. (1969). "Theory of Stimulated Raman Scattering." Physical Review **182**(2): 482-494.

Wang, C.-S. (1975). Quantum Electronics. New York, Academic.

Weliky, D. P., T. J. Byers, K. E. Kerr, T. Momose, R. M. Dickinson and T. Oka (1994). "High-resolution laser spectroscopy of the $Q_v(0)$ transitions in solid parahydrogen." Applied Physics B **59**: 265-281.

William R. Trutna, J., Y. K. Park and R. L. Byer (1979). "The dependence of Raman gain on pump laser bandwidth " IEEE Journal of Quantum Electronics **15**(7): 648-655.

Woodbury, E. J. and W. K. Ng (1962). Proc. IRE **50**: 2367.

Acknowledgement

The experimental work for the present diploma thesis was carried out at the Department of Molecular Physics of the Fritz-Haber-Institut der Max-Planck-Gesellschaft.
I would like to thank Prof. Gerard Meijer for giving me the opportunity to work on the project of building a hydrogen crystal Raman shifter, and for his kind scientific supervision of this project.

I would like to express particular thanks to my direct supervisor, André Fielicke, for his great support in all matters pertaining to the experiments. I very much enjoyed working in his group.

I would also like to thank Wolfgang Erlebach and Henrik Haak for their valuable advice and ideas in construction-related problems. I am sure that without their help, the project would not have achieved the success it did.

My thanks also go to Uwe Lehmann for his contribution in the early phases of the project in the working out of the initial plans for the Raman cell and the optical setup.

And last but not least, I would like to thank Thomas Lehmann and Thorsten Nemes as well as the entire team from the precision mechanics workshop, who did a wonderful job in constructing our hydrogen cells and all the other parts we needed for the operation of the Raman shifter.

Index